Università degli Studi di Padova
Dipartimento di Fisica e Astronomia "Galileo Galilei"

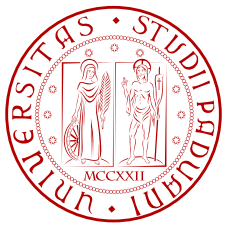

Corso di Dottorato di Ricerca in Fisica
XXIX CICLO

Phase separation, patterning and orientational ordering on closed surfaces: modelling the dynamics of molecules on biological membranes and vesicles

Coordinatore:
Prof. Gianguido Dall'Agata
Supervisore:
Prof. Enzo Orlandini

Dottorando: Giulio Vandin

Contents

Chapter 1

Introduction

In 1973, a seminal work by Helfrich [1] combined the classic theory of elastic shells and plates with the fluid mosaic model of plasma membranes [2] to describe the elastic properties of lipid bilayers. Since then, mechanistic models of the behaviour of cell membranes have been characterised by an extensive use of concepts borrowed from differential geometry to describe both the shape of the membrane and the dynamics of the molecules that constitute it, allowing the development of the field of statistical mechanics of random surfaces[3, 4, 5, 6]. Attempts to couple the two levels of description date back to 1991, when Andelman & al. [7] proposed a model for the equilibrium shape of bilayer vesicles and the biconcave morphology of human red blood cells which involved a phase-separating membrane, namely a scalar field modelling the coarsening of a binary mixture, and its interaction with the curvature of the membrane. Over the years, many works [8, 9, 10, 11, 12, 13, 14, 15] have focused on these dynamics, from a theoretical as well as a computational point of view, and recently the application of Finite Element Methods (FEM) [16, 17] has brought enhanced precision and stability to numerical models of phase-separating mixtures on curved surfaces. On the other hand, several in vitro studies have

The key concept to describe these dynamics is a field expressing a local order parameter that resides on the surface. While in the models describing the surface distribution of lipid

phases and membrane proteins a scalar order parameter is sufficient, in principle there can be also orientational order [18], given for instance by the direction of the membrane lipids, membrane proteins or cortical cytoskeleton [19, 20, 21]. This can be described by means of a vector field. Computational studies of membrane structures with orientational order have been performed, mainly through the use of Monte Carlo methods [22, 23], which can either sample equilibrium configurations or describes effective kinetic models but for relatively small systems.

In this thesis we address the problem of how inhomogeneities forming in scalar and vector order parameters during their evolution are affected by and affect the shape and curvature of the hosting surface. This investigation will be done by using a macroscopic description of the system based on Partial Differential Equations on differential manifolds, that will be integrated by means of numerical simulations on discretised surfaces.

Questions we want to address are the following:

1. How do phase separation and pattern formation evolve on curved surfaces?
2. What mechanisms involving surface curvature can arrest coarsening ?
3. What are the evolution and equilibrium configurations of elastic vesicles that are subject by local forces proportional to the phase separating fields ?
4. How can the dynamics of vector fields, describing local orientational order, be modelled and numerically integrated on curved surfaces?

Through the chapters of this thesis we construct theoretical and computational models to address these questions by proceeding in the following order.

In chapter 2 we introduce the general geometrical tools needed for the construction of the numerical models. More precisely we discuss the properties of smooth manifolds, the differential operators defined upon them, and their discrete approximation needed for numerical integration. In chapters 3 and 4 we consider the case in which the relaxation dynamics of the surface field is much faster than the corresponding evolution of the surface shape, that we assume to be static.

In chapter 3 we describe the phase separation dynamics of a scalar field evolving as a model B on a closed surface. More precisely, by starting from the work of Marenduzzo and Orlandini on the arrest of phase separation on curved membranes [24], we build a theoretical model to account for the arrest of coarsening induced by the curvature of the surface. We then proceed to test our model and its numerical implementation, confirm predictions from the theory, and investigate its consequences on the dynamical evolution of the order parameter in such systems.

In chapter 4 we address the problem of the formation of patterns on curved membranes and their localisation on specific regions of the surface through coupling with its curvature. After a brief revision of the Turing theory of pattern formation described in terms of reaction-diffusion equations, we study its modification on a curved substrate, and then couple it with a phase separation dynamics described by a scalar field. The results we obtain prove the possibility to limit the emergence of patterns to confined regions of the surface. We then describe alternative ways by which the curvature of a surface can influence the modes of surface patterns.

In chapter 5 we abandon the assumption of a static surface and we consider a situation where surface phase separation dynamic and the evolution of membrane shape evolve on a comparable time scale. We introduce a linear model in which the two phases of the surface field induce a normal stress on the membrane that deforms accordingly. This model is implemented by using finite element methods and taking into account the elastic properties of the membrane.

Finally, chapter 6 is devoted to present results on the relaxation dynamics of the director field of a nematic fluid on a curved surface. The main difficulty in the numerical simulation of this system is the construction of the discrete covariant differentiation of vectors that appears in the equation of motion of the field. After defining local reference frames for vector fields on triangular mesh surfaces, we present an effective laplacian operator and test it on a nematic field on a spherical surface.

Chapter 2

Differential geometry of curved surfaces

The objects we will study in this work are the closed surfaces topologically equivalent to a sphere. This choice is motivated by two main reasons: on the one hand, it is the shape of many biological objects like micelles, subcellular vesicles like vacuoles, lysosomes, transport and secretory vesicles, and cells themselves; on the other hand, this particular topology provides a simple starting point to study the general dynamics of fields on closed surfaces and their interaction with the underlying geometry, no particular complications of the theory being needed to adapt them to other closed surfaces like tori. Further work will be needed though if one wanted to extend the models to surfaces with boundaries.

We now introduce the notion of surface in the context of differential geometry, along with the main operators and representations we will use throughout our work.

2.1 Smooth manifolds

The starting point of our dissertation is the notion of surface. An extrinsic definition of such an object can be done in terms of a parametric surface: a smooth surface $\mathcal{M}$ is defined as

the image of a smooth differentiable function $\mathbf{x} : \mathbb{R}^2 \to \mathbb{R}^3$. Every point of surface $\mathcal{M}$ is then expressed in 3-dimensional space as $\mathbf{x}(u, v)$, where u and v are the independent variables in the euclidean plane. In this notation, a scalar, vector or matrix function f on the surface is simply the restriction $f|_{\mathcal{M}}$; the operation of differentiation of these functions along the surface clearly coincides with the differentiation of $f|_{\mathcal{M}}$ with respect to u, v. Furthermore, if the defining function is restricted to a curve $\Gamma \in \mathbb{R}^2$, the image will be a curve $\gamma = \mathbf{x}(\Gamma) \in \mathcal{M}$.

This definition allows to derive all the geometrical characteristics of the surface in an easy way, exploiting the linearity of the embedding space $\mathbb{R}^3$, but gives rise to higher computational complexity because 3-dimensional differential operators need to be applied to a discretised volume in which the surface is parametrised, instead of being applied to the surface itself. Thus, an intrinsic definition of a surface comes in handy, since it can be done without the use of (x, y, z) coordinates: this is the definition we will use when performing analytical studies, and it will also be useful for numerical operations in the discretised version of the surfaces. The smooth surface $\mathcal{M}$ is defined intrinsically as a topological manifold with a $\mathcal{C}^\infty$ maximal atlas, each one of whose charts ψ_p maps an open neighbourhood U_p of a point p of $\mathcal{M}$ to an open set in the euclidean plane $\mathbb{R}^2$ (see appendix A for details).

This correspondence allows to define scalar functions and curves in a natural way by the use of local charts. If $F : \mathbb{R}^2 \to \mathbb{R}$ is a $\mathcal{C}^k$-differentiable function, near point $p \in \mathcal{M}$ the composition $f = F \circ \psi_p : U_p \to \mathbb{R}$ is a scalar function on $\mathcal{M}$; this function can describe any scalar field on the surface, whether it be a geometrical quantity, a density of some substance on the surface or any other field with geometrical or physical meaning for which this representation of a surface is useful. Conversely, given a curve in euclidean space $\Gamma : \mathbb{R} \to \mathbb{R}^2$, a parametric curve on $\mathcal{M}$ can is given by the composition $\gamma = \Gamma \circ \psi_p : \mathbb{R} \to U_p$.

It is now a natural idea to extend to a manifold other mathematical objects such as vectors and matrices. If the linear properties of this objects have to be preserved, their definition must come from the local linearised maps of the curved surface, i.e. on the tangent planes. This is when the notion of a curve on $\mathcal{M}$ turns useful: it can be used to define tangent vectors as

the differentials of curves, hence the tangent plane to manifold $\mathcal{M}$ at point p is given by the quotient

$$T_p\mathcal{M} = \frac{\{\gamma : \mathbb{R} \to \mathcal{M} | \gamma(0) = p,\ \gamma \textit{ differentiable in } 0\}}{\left\{\gamma \sim \gamma' \textit{ if } \left.\frac{d\psi_p \circ \gamma}{dt}\right|_{t=0} = \left.\frac{d\psi_p \circ \gamma'}{dt}\right|_{t=0}\right\}}.$$

On the tangent plane a set of basis vectors can be chosen as a local reference frame for vector computations, such as the operation of directional derivative of a scalar function: given a vector $V \in T_p\mathcal{M}$ tangent to the curve $\gamma(t)$, $\gamma(0) = p$, and a scalar function $f : \mathcal{M} \to \mathbb{R}$, the directional derivative of f along V is

$$D_V f(p) = \left.\frac{d(f \circ \gamma)}{dt}\right|_{t=0}.$$

A coordinate version of the above expression can be given through the local charts at p: because the charts are always bijective, if a point p on the surface is mapped to $\mathbf{x} = (x^1, x^2) \in \mathbb{R}^3$, the directional derivative is given by

$$D_V f(p) = \left.\frac{d(f \circ \psi_p^{-1} \circ \psi_p \circ \gamma)}{dt}\right|_{t=0} = \left.\frac{dx^i}{dt}\ \frac{df}{dx^i}\right|_{t=0} = V^i \partial_i f(p).$$

Note that the components of vector V are given relative to the directional derivatives ∂_i: the latter in fact constitute a natural basis for the tangent space. Since such a basis exists at every point $p \in \mathcal{M}$, it is possible to construct a vector-valued function on $\mathcal{M}$ by associating to each point p a single vector $V(p)$ of the tangent space $T_p\mathcal{M}$. This class of objects are useful for many different purposes: they can be of course the gradients of scalar fields, but they can also represent velocity fields and orientations of polar objects, among the others.

It is now possible to identify the cotangent space at point p $T_p^*\mathcal{M}$ with the set of real-valued linear operators acting on $T_p\mathcal{M}$. In this formalism, a basis for the cotangent space $T_p^*\mathcal{M}$ is given by the differentials dx^i, which is consistent with the definition of the ∂_i basis of $T_p\mathcal{M}$ if the orthonormality condition $dx^i \partial_j = \delta_{ij}$. We now have all that is needed to define tensor quantities: the space $T_s^r(T_p\mathcal{M})$ of the tensors of rank (r, s) is defined as the space of linear operators $T : \overbrace{T_p\mathcal{M} \otimes \cdots \otimes T_p\mathcal{M}}^{r \text{ times}} \otimes \overbrace{T_p^*\mathcal{M} \otimes \cdots \otimes T_p^*\mathcal{M}}^{s \text{ times}} \to \mathbb{R}$. Tensors will be more easily

expressed as their components with respect to the elements of the basis $\partial_{i_1} \cdots \partial_{i_r} dx^{j_1} \cdots dx^{j_s}$ of $(T_p\mathcal{M})^r (T_p^*\mathcal{M})^s$: in this notation there will be two sets of indices, so that the typical expression will be $T^{i_1 \cdots i_r}_{j_1 \cdots j_s}$. From now on, we shall use the Einstein notation for sum over repeated indices, so that a sum is assumed when a high index and a low index are equal in a tensor expression:

$$A^\mu B_{\mu\nu} = \sum_\mu A^\mu B_{\mu\nu}.$$

2.2 Geometry of smooth surfaces

Now that the extrinsic and intrinsic definitions of a surface have been given, we can characterise the shape of the surface through a set of geometrical operators. In this section we introduce the notions of metric of a manifold, its shape tensor, the curvatures and the differential operators that will be used in the dynamical models of the next chapters. Throughout the chapter, the extrinsic and intrinsic notation will be used interchangeably, since the results obtained in one representation still hold in the other one.

2.2.1 Metric tensor

The metric tensor, also called first fundamental form, is a rank (0,2) tensor that extends the idea of scalar product to a curved surface $\mathcal{M}$. In $\mathbb{R}^2$ we can define a scalar product between two vectors $\mathbf{v}$, $\mathbf{w}$ as the action of the symmetric bilinear operator g, so that the result is the scalar quantity $\mathbf{v}^T g \mathbf{w}$. If g is the identity matrix $\mathbb{I}$, the scalar product is the usual euclidean one, and it induces the euclidean metric defined as $||\mathbf{u}|| = \sqrt{\mathbf{u}^T \mathbb{I} \mathbf{u}} = \sqrt{\mathbf{u}^T \mathbf{u}}$; non-euclidean metrics are defined the same way even if the symmetric operator g is different from the unity:

$$|\mathbf{u}|_g^2 = \mathbf{u}^T g \mathbf{u} = g_{11} u_1^2 + 2 g_{12} u_1 u_2 + g_{22} u_2^2. \tag{2.1}$$

An easy way to obtain the metric tensor is to compute the arclength of a curve on a parametric surface $\mathcal{M}$, and exploit the tie between the metric and the distance: in order to

find the length of the curve $\mathbf{x}(u(t), v(t))$, $t \in [a, b]$, we must solve the integral

$$s = \int_a^b \left|\left| \frac{d}{dt}\mathbf{x}(u(t), v(t)) \right|\right| dt.$$

The integrand contains the differential of the line element of the curve: this is the analogue of the euclidean length of an infinitesimal segment on the curve, and it reads

$$ds = \left|\left| \frac{d}{dt}\mathbf{x}(u(t), v(t)) \right|\right| dt = \sqrt{\left(\frac{d\mathbf{x}}{du}\frac{du}{dt}\right)^2 + 2\left(\frac{d\mathbf{x}}{du}\frac{du}{dt}\right)\cdot\left(\frac{d\mathbf{x}}{dv}\frac{dv}{dt}\right) + \left(\frac{d\mathbf{x}}{dv}\frac{dv}{dt}\right)^2}. \tag{2.2}$$

In order to recover an expression analogous to the (2.1) we can bring this to a form

$$ds^2 = g_{11}\left(\frac{du}{dt}\right)^2 + 2g_{12}\frac{du}{dt} + g_{22}\left(\frac{dv}{dt}\right)^2. \tag{2.3}$$

The comparison between (2.2) and (2.3) gives the expression for the first fundamental form in terms of the partial derivatives of the coordinates in $\mathbb{R}^3$ of the surface points:

$$g_{\mu\nu}(\mathbf{u}) = \frac{d\mathbf{x}}{du^\mu}(\mathbf{u}) \cdot \frac{d\mathbf{x}}{du^\nu}(\mathbf{u}), \tag{2.4}$$

where du^μ represents du if $\mu = 1$, dv if $\mu = 2$.

The values of the metric tensor computed this way still hold when considering an intrinsic representation of the surface, provided that the local coordinates on the tangent plane coincide with the parametric variables u, v. Generally speaking, a metric tensor is any rank-(0,2) tensor which is bilinear, symmetric and nondegenerate (i.e. its kernel on the tangent space $T_p\mathcal{M}$ is the null set), which varies smoothly with p. It is easy to see that, being the local charts smooth functions, the metric tensor obtained via equation (2.4) is itself smooth.

As said in the beginning of this section, the metric tensor can be used to compute the scalar product between two vectors in the tangent space: if v^μ and w^μ are vectors in $T_p\mathcal{M}$, then their scalar product is computed as $g_{\mu\nu}(p)v^\mu w^\nu$. This induces a relevant property of this tensor,

which can be used to lower the indices of vectors and tensors on the tangent space, according to $v_\mu = g_{\mu\nu}(p)v^\nu$. The inverse of the metric tensor $g^{\mu\nu}(p)$ acts in the same way when rising indices is required: $v^\mu = g^{\mu\nu}v_\nu$.

2.2.2 Curvature

For each point of the surface $\mathcal{M}$, the normal vector field of norm 1 can be computed as the normalised vector product of two nonparallel tangent vectors. More precisely, if $d\mathbf{x}/du$ and $d\mathbf{x}/dv$ are the local basis vectors of $T_p\mathcal{M}$, the unit normal is obtained by the product

$$\mathbf{n}(p) = \frac{\frac{d\mathbf{x}}{du} \wedge \frac{d\mathbf{x}}{dv}}{\left|\frac{d\mathbf{x}}{du} \wedge \frac{d\mathbf{x}}{dv}\right|}. \tag{2.5}$$

The second fundamental form, also called shape tensor, is a tensor that is necessary, together with the metric tensor, to compute the curvature of the surface. Specifically, this tensor catches the normal component of the second derivatives of the coordinate points, formalising this way the intuitive idea of curvature as a "bulging" of an extrinsic surface:

$$b_{\mu\nu}(p) = \frac{d^2\mathbf{x}}{du^\mu du^\nu} \cdot \mathbf{n}(p).$$

The eigenvalues of the second fundamental form are called the principal curvatures of the surface at point p, let them be κ_1 and κ_2.

In this notation, the mean curvature at point p is defined as the scalar function

$$H(p) = (\kappa_1 + \kappa_2)/2.$$

This quantity is positive when the surface is convex, negative when it is concave. Note that on a plane, it takes the constant value zero, but not only: on a saddle point where $\kappa_1 = -\kappa_2$ the curvature is zero, and this situation can be driven to its extreme consequences, as in the case of minimal surface, whose mean curvature is zero at every point.

Without needing to extract the eigenvalues of the shape tensor, we can compute the curvature exploiting the fact that the trace of a matrix equals the sum of its eigenvalues, whatever the basis in which it is expressed. Mean curvature is thus just one half of the trace of the second fundamental form, which is computed as

$$H(p) = \mathrm{Tr}(b(p)) = \frac{1}{2} g^{\mu\nu}(p) b_{\mu\nu}(p).$$

A different definition of curvature can be done in an intrinsic context, obtaining another scalar function called gaussian curvature $K(p)$. This quantity can be defined in terms of the Christoffel symbols without any need to embed the surface in 3D space (see App. A), but it is more easily computed as the product of the principal curvatures, so that

$$K(p) = \kappa_1 \kappa_2.$$

Again, we can skip direct computation of the eigenvalues, by considering the fact that the determinant of a matrix is equal to the product of its eigenvalues. Thus a compact formula for the gaussian curvature is

$$K(p) = \det(b^{\mu}{}_{\nu}(p)) = \det(g^{\mu\rho}(p) b_{\rho\nu}(p)) = \frac{\det(b_{\mu\nu}(p))}{\det(g_{\mu\nu}(p))}.$$

2.2.3 Covariant derivative

The operation of differentiation will be fundamental in every aspect of our work; we therefore need to extend the notion of derivative to curved surfaces. This is done very easily in the case of scalar fields: if $f : \mathcal{M} \to \mathbb{R}$ is a scalar field and (u_1, u_2) are local coordinates around point p, then the directional derivative of f in direction u_μ is simply the partial derivative $\partial_\mu f$.

Things get much more complicated when we compute the derivative of a vector field. When a vector is transported along a curve on a curved surface, its orientation can vary from point to point, since the vector is moving across the tangent planes of different points. If this transport

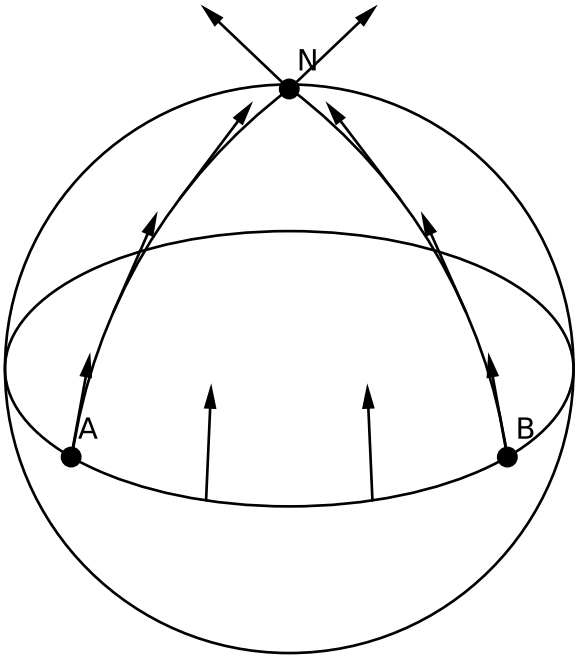

Figure 2.1: Parallel transport of a vector field from A to N keeping a constant angle with each geodesic segment: the shortest path from A to N gives an orientation, while the path going through point B gives an orientation orthogonal to the first one.

occurs along a closed curve, there can be points where the definition of the vector is not univocal, leading to inconsistencies (see Fig. 2.1). In order to fix these inconsistencies, a univocal choice of the orientation of the field for each point is needed. This means the directional derivative need to be corrected with an additional term which rotates the vector in order to align it with its correct orientation within the local reference frame. We here give the form of this correction term, referring to appendix A for the details: if $g_{\mu\nu}(p)$ is the metric tensor on the tangent space $T_p\mathcal{M}$, the affine connection is the quantity

$$\Gamma^{\rho}_{\mu\nu} = \frac{1}{2} g^{\rho\sigma} \left(\partial_\nu g_{\sigma\mu} + \partial_\mu g_{\nu\sigma} - \partial_\sigma g_{\mu\nu} \right) .$$

The covariant derivative $\mathbf{D}$ is the surface derivative consistent with a univocally chosen parallel transport, and it adds to the usual directional derivative ∇ as many copies of the affine connection as the rank of the tensor being differentiated. As an example, the covariant derivative acts on a vector (resp. covector) field in the following way:

$$D_\mu V^\nu = \partial_\mu V^\nu + \Gamma^\nu_{\mu\sigma} V^\sigma, \qquad\qquad D_\mu V_\nu = \partial_\mu V_\nu - \Gamma^\sigma_{\mu\nu} V_\sigma.$$

The same rule holds for tensors of any rank, provided that there is one copy of the affine connection for each index of the tensorm, with positive sign for high indices and a minus sign for low ones.

An application of this rule that is of fundamental importance in our work is the Laplace-Beltrami operator, the curved analogue of the laplacian. Its action on a scalar field $f : \mathcal{M} \to \mathbb{R}$ takes the form

$$\nabla^2_{LB} f = g^{\mu\nu} \left(\partial_\mu \partial_\nu f - \Gamma^\rho_{\mu\nu} \partial_\rho f \right). \tag{2.6}$$

2.3 Discrete setting

Now that all the operators of interest have been defined, we need to discretise the surface in order to be able to perform discrete computations on it. We choose to do so by the dyadic triangulation algorithm introduced by [25]: we start from a regular icosahedron inscripted in a unit sphere. Each edge is bisected and the midpoint projected outwards onto the surface of the sphere as a new grid point. New segments are drawn connecting the new nearest neighbours, and the a new discretisation is produced. Repeating this recursively m times starting from the initial icosahedron we get what is called the level-m geodesic grid. For our purposes we choose a level-4 grid with 2562 vertices and 5120 facets as an acceptable compromise between grid refinement and computational efficiency.

Now we have to introduce a differential structure on our surface. Since a spherical surface does not allow the existence of a global mapping of real coordinates without singularities, we

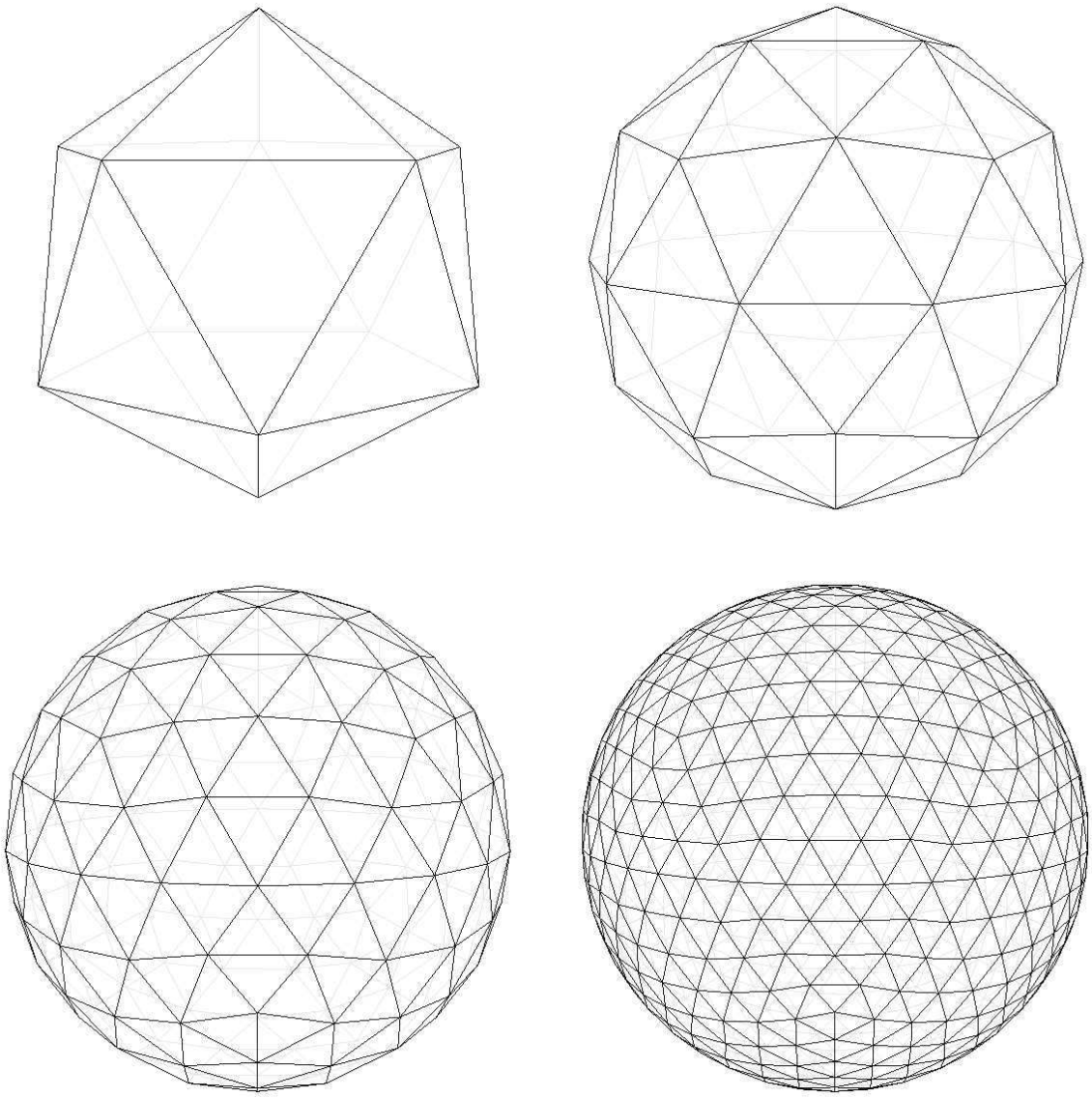

Figure 2.2: Dyadic triangulation: first figure on the left is the regular icosahedron, i.e. level-0 geodesic grid. On the right the level-1 grid with 80 facets is obtained by duplication of the edges of the icosahedron. On the bottom line the recursion is brought forward: from the left, grids of level 2 and 3 are shown, with 320 and 1280 facets respectively.

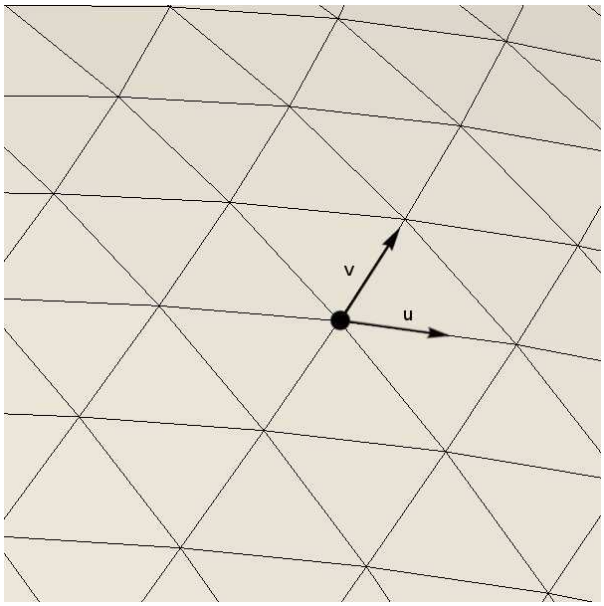

Figure 2.3: A local reference frame for differentiation at a fixed grid point. Note that in the points with 6 neighbours, 3 local frames can be defined (the other 3 being specular to them), while in the points with 5 neighbours there are 5 possible choices of the local basis.

will choose to adopt local reference frames, naturally defined by the couples of edges connecting a chosen vertex point to the closest first neighbours (see Fig. 2.3). Note that the 12 vertices of the initial icosahedron have 5 nearest neighbours, while the rest of the points of the grid have 6, however high the level of the grid. This fact forces us to treat differently these 12 "singular points", with a different number of local bases and in general different algorithms for the directional derivatives. The local basis vectors (u, v) are used as a basis of the tangent plane $T_{V_i}\mathcal{M}$ at vertex V_i, and all of the geometrical operators defined in this chapter are computed on this plane. We will not go now in the details of the numerical implementations of the operators, because they will be chosen differently according to the specific task to be accomplished: for this reason, they will be presented along with their application when they are needed.

2.3.1 Euler characteristic

Every curved surface can be covered with a triangulation such as the one described in the previous section. Every realisation of the triangulation is characterise by the number of vertices of the mesh N, the number E of edges connecting the vertices, and the number F of triangular faces among which the surface is subdivided. The Euler characteristic χ of a triangulated surface is defined by the formula

$$\chi = N - E + F.$$

Any convex polyhedron's surface has Euler characteristic 2, and this holds true whatever the number of vertices N in the triangulation. It can be shown that when the number of vertices tends to infinity this formula still holds, leading to conclude that the sphere has $\chi = 2$. Taking as an example the dyadic triangulation of section 2.3, we can easily compute [25] the numbers of vertices, edges and faces in level-m geodesic grid to be

$$N_m = 2 + 10 \cdot 4^m \qquad E_m = 30 \cdot 4^m \qquad F_m = 20 \cdot 4^m,$$

for every integer $m \geq 0$. Applying the formula for the Euler characteristic to the geodesic surface we get the result

$$\chi_m = N_m - E_m + F_m = 2 + 10 \cdot 4^m - 30 \cdot 4^m + 20 \cdot 4^m = 2$$

for any m. Thus taking the limit $m \to \infty$ leaves the result unchanged, concluding that the sphere obtained as level-∞ geodesic grid has $\chi = 2$.

Chapter 3

Phase Separation on Curved Membranes

The concept of phase in soft matter physics is strictly related to the foundational idea that, at low scales of energy, the structure of matter produces a behaviour which tends to be constant over a macroscopic region of space. Quite naturally from a conceptual point of view, since the properties of matter need to be constant within a region of one single phase, no mixing of two different phases occurs when they come in contact with each other, so that an interface is formed at the boundary between them. In precise regions of the thermodynamic phase space, this separation evolves in the direction of the minimal surface area between the phases, leading to the coarsening process called phase separation.

Many systems are known to undergo phase separation. Some of them allow different different phases of matter to change one into the other: this is the case when the phase is a state of matter characterised by one precise set of spatio-temporal relationships among the components of the phase and of fundamental interactions at work among them. An example of this situation is a system at supercritical conditions for the evaporation of water, at which liquid and gaseous parts of one same substance undergo at the same time separation, with the progressive reduction of the number of drops to minimise interfacial area between the phases, and phase

transition, with the volume of the liquid phase being progressively reduced. Another class is the opposite case of different substances, which can be in the same state of matter, but be immiscible for different reasons, such as entropy maximisation: this is for example the case of an unstable liquid emulsion of oil and water, which is driven by the single process of shrinking of the interfacial area. This latter class is of particular interest in biological soft matter, since phase separating mixtures are observed in a great variety of biologically interesting situations.

There are many examples of these dynamics: the functional internal compartmentalisation of living cells, in which liquid phases separate from the cytoplasm to provide a segregated region where biochemical reactions can occur without interfering with other subcellular processes [26, 27]; the coarsening of a bacterial suspension, with a separation taking place between areas of lower density of swimmers in the suspension medium [28]; and phase separation among the variety of lipid phases which compose the complex fluid mosaic of phospholipidic membranes [29, 30, 31]. This last process has been investigated experimentally through the use of *Giant Unilamellar Vesicles* (GUV), stable, artificially assembled bilayers of lipids, as well as cell-derived *Giant Plasma Membrane Vesicles* (GMPV), as model membranes. The recent developments in high resolution fluorescence microscopy have allowed to confirm the raft ipothesis, according to which phase segregation occurs between liquid ordered and liquid disordered lipid phases [29, 32]. Moreover, it has been possible to clarify the role of sterol structure in determining the ability to form domains and the association with local membrane curvature [33, 34] . Because of the inherently curved nature of biological membranes, if one wanted to model this phenomenon as a set of mathematical equations, he would need to include the influence of the geometry of the membrane in the model, changing the nature of the process in a potentially radical way, as in the case of curvature-modulated phase separation [35].

In this work we build a general model for phase separation on curved membranes, studying the influence of geometry on the evolution of the system and its long-time-limit outcomes, starting from the well known Cahn-Hilliard model of phase separation, adapting it to curved geometries and including the effect of curvature on the dynamics. Since the phenomena we

want to address are out of equilibrium, theoretical models of them tend to fail in finding exact analytical representations of the evolution of these systems. Though steady-state solutions can be deduced from the choice of a particular set of equations describing the model, the role of numerical simulations is often crucial in determining the details of the reproduced dynamics. We therefore put together a set of computational tools to couple the phase separation dynamics with the curved objects as described in chapter 2.

This chapter is structured as follows: in the first section we will make a general presentation of the Cahn-Hilliard theory of phase separation, from the derivation of the model to a study of the steady state solutions; in the second section we will focus on the numerical methods used to study the dynamical evolution of the model on a flat geometry through use of computer simulations and the study of the results; in the third section we explain the numerical algorithms used in the simulation of the curved case and comment the results. In the last section we will present a modified version of the model to take into account the effect of curvature on the dynamics, along with a theoretical study of the steady state solutions and the results of numerical study.

3.1 The Cahn-Hilliard model

To make our dissertation more clear, we now start with one of the simplest system undergoing spontaneous phase separation: one can imagine a two-component fluid made up of two immiscible phases, which we label A and B (e.g. oil and water) undergoing spontaneous phase separation as the temperature is not higher than a threshold value T_c. For the sake of simplicity, we will assume that the temperature of the system is always under this critical value; though done for simplification, this assumption will hold when considering biological systems, as the temperature variations occurring in physiological conditions are usually limited.

A well-studied model of this system is based on the Cahn-Hilliard free energy, originally build to model the phase separation of binary alloys [36]. This is a classical example of conserved dynamics, model B in the Hohenberg-Halperin classification [37]. This dynamical evolution of

this class of systems is described by a differential equation involving the chemical potential descending from the free energy of the system along with a noise term taking into account the effects of thermal fluctuation. After identifying an order parameter φ and a chemical potential associated with φ, the equation takes the following general form:

$$\frac{\partial \varphi(\mathbf{x},t)}{\partial t} = M\nabla^2 \mu(\mathbf{x},t) + \xi(\mathbf{x},t). \tag{3.1}$$

In the Cahn-Hilliard model, a local order parameter is defined as the difference between the volume concentrations of the two substances, $\varphi = c_A - c_B$. A double-well free energy potential is chosen as a functional of the order parameter, representing the two stable separated phases A and B; a gradient term takes into account the driving force of surface minimization. We are implicitly assuming that the temperature of the system is below the critical value for phase demixing. We thus have the free energy

$$\mathcal{F}[\varphi] = \int d^2x \left[f(\varphi(\mathbf{x})) + \frac{\kappa}{2} \left|\nabla \varphi(\mathbf{x})\right|^2 \right]. \tag{3.2}$$

In our particular case, we choose as the double-well function f the simple Landau potential for second order phase transitions. This is defined by a polynomial of the fourth order, wich allows to simply derive the expression for the chemical potential, and consequently the time evolution of the binary mix:

$$f(\varphi) = \frac{\varphi^4}{4} - \frac{\varphi^2}{2}. \tag{3.3}$$

It is immediate to derive the chemical potential of the system through functional derivation of this free energy with respect to φ:

$$\mu(\mathbf{x},t) = \frac{\delta F[\varphi]}{\delta \varphi(\mathbf{x},t)} = \varphi^3(\mathbf{x},t) - \varphi(\mathbf{x},t) - \kappa\nabla^2\varphi(\mathbf{x},t), \tag{3.4}$$

provided we chose periodic or zero-flux boundary conditions, to avoid linear terms in the gradient at the boundaries of the domain. In the Cahn-Hilliard model there is no reaction

between the two components: this implies a global conservation of the order parameter φ, which implies the existence of a conserved current. This current is given by the gradient of the chemical potential 3.4. Furthermore, we model the thermal fluctuations as being negligible with respect to the laplacian of the chemical potential, thus the time evolution of the order parameter is given by the continuity equation:

$$\dot{\varphi} = \nabla^2 \left[\varphi^3 - \varphi - \kappa \nabla^2 \varphi\right], \tag{3.5}$$

where we set the parameter $M = 1$ in eq. 3.1 to simplify calculations.

From the nonlinear equation (3.5) one can easily obtain the main features of the system, assuming a random initial configuration, with values in the interval [-1,1] and the integral of φ equal to zero - i.e. the two fluids A and B are found in the same amount.

The potential (3.3) is the starting point to find the bulk stable states: the minima $\varphi = \pm 1$ of this function will be attractors for φ in the homogeneous zones of the system. There is another steady state for $\varphi = 0$, but this happens to be unstable to small perturbations, and does not therefore represent another phase of the system. Once we introduce the interface term $\kappa \left|\nabla \varphi\right| / 2$, we can obtain the profile of the interface for $\dot{\varphi} = 0$, that is, the curve that solves the stationary equation in the normal direction x to the interface:

$$\kappa \frac{\partial^2 \varphi(x)}{\partial x^2} = \varphi(x)^3 - \varphi(x).$$

The solution is a nonlinear combination of exponentials, which can be written in a compact form as

$$\varphi(x) = \tanh\left(\frac{x}{\sqrt{2\kappa}}\right),$$

which smoothly connects regions with constant value $\varphi = -1$ with others with $\varphi = 1$. Since the surface energy term has a positive coefficient within the free energy functional, it needs to be minimised at the steady state: when starting from a random configuration with φ varying

randomly yet smoothly from point to point, the interfacial length between the two bulk phases has to be the minimal one, thus, in a flat space, a straight line.

Up to now, we just described the steady-state solution of the Cahn-Hilliard equation. In the next section we shall briefly go through the dynamical properties of this model.

3.2 Cahn-Hilliard model on a flat plane

3.2.1 Numerical Methods

As we already saw, the equation that determines the time evolution of this specific model is a nonlinear one. This implies a general difficulty in finding analytic solutions for its evolution from a given initial configuration to the steady state we just described. Though it is proven that a unique solution to the boundary problem exists, along with some of its properties, the deterministic outcome of the evolution from a given set of data is better studied with numerical tools, provided they are stable. We now present the numerical evaluation of the evolution produced by this model in the simpler case of a flat surface; we shall later move on to more complex domains. We choose to study the equation on a triangulated regular flat plane, since our the following developments of our models shall move onto triangulated curved surfaces. The grid is constructed as a planar set of points at the vertices of adjacent equilateral triangles. This results in a regular structure with hexagonal symmetry around each point.

In order to study the evolution of our equation, we need to be able to evaluate numerically the one differential operator that appears in the expression. The most straightforward way to do consists in discretising second order directional derivatives into second order finite differentiations and apply an averaging along the three different directions of the edges intersecting at each point.

The central finite difference algorithm of order n for regular grids of step Δx gives an estimate of the derivative along a certain direction of a function f at a point x, provided that the values of f at points x, $x + \Delta x$ and $x - \Delta x$ are known. It relies on the second order Taylor

expansion of the function around point x, and it can be expressed with the following formula:

$$\frac{\delta^2 f(x)}{\delta x^2} = \frac{f(x+\Delta x) - 2f(x) + f(x-\Delta x)}{\Delta x^2}.$$

These numerical derivatives have to be evaluated along the three couples of parallel segments that intersect at point x. This wouldn't be necessary on a rectangular grid, since orthogonal directions can be summed directly when constructing the laplacian; we choose this method to prove it useful when we shall switch to curved membranes, in which triangulation is in general preferred, especially with spherical topologies.

As for the time evolution: we are now left with a differential equation of the type

$$\dot{\varphi}_i(t) = F_i(t) = F(\varphi_i(t)),$$

where F is the discretised version of the Cahn-Hilliard operator $F[\varphi] = \nabla^2\left[\varphi^3 - \varphi - \kappa\nabla^2\varphi\right] = 6|\nabla\varphi|^2 + (3\varphi^2 - 1)\nabla^2\varphi - \kappa\nabla^4\varphi$. For our simulations we used a fourth order Adam-Bashforth-Moulton predictor-corrector method. This method can be written in a compact form as

$$\varphi_i(t+\Delta t) = \varphi_i(t) + \Delta t P_i(\varphi, F; t),$$

where the predictor-corrector operator P_i gives an estimate of the time integration of F_i over the discrete time integral Δt. To write its explicit form, we need at each grid point the value of the Cahn-Hilliard operator at time t as well as those at the three previous time steps. These values are used to estimate the value at time $t + \Delta t$ through the fourth-order predictor:

$$\tilde{\varphi}(t+\Delta t) = \varphi(t) + \Delta t\left(\frac{55}{24}F_i(t) - \frac{59}{24}F_i(t-\Delta t) - \frac{37}{24}F_i(t-2\Delta t) - \frac{3}{8}F_i(t-3\Delta t)\right).$$

Given $\tilde{\varphi}(t+\Delta t)$, one can plug it into the expression for F, obtaining the $\tilde{F} = F(\tilde{\varphi})$ needed for

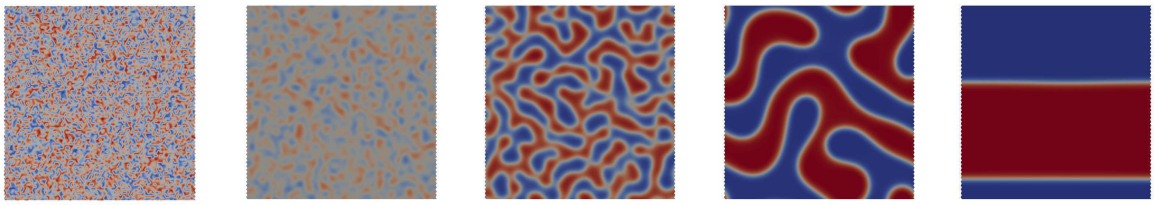

Figure 3.1: Five snapshots of the time evolution in $\log(t)$ of φ from an initial random configuration (first from the left) to complete separation (last on the right). Phase A ($\varphi = +1$) is indicated by colour red, while phase B ($\varphi = -1$) is blue.

the computation of the corrector; this gives the second (implicit) step

$$\varphi(t + \Delta t) = \varphi(t) + \Delta t \left(\frac{3}{8}\tilde{F}_i(t + \Delta t) + \frac{19}{24}F_i(t) - \frac{5}{24}F_i(t - \Delta t) + \frac{1}{24}F_i(t - 2\Delta t) \right),$$

which gives the final estimate for the updated value of φ, with a higher order of convergence than one would obtain with explicit methods of lower orders like the Euler algorithm [38].

3.2.2 Phase separation dynamics on flat spaces

With our numerical scheme, we studied eq. (3.5), starting from an initial configuration with random values at each point distributed uniformly in the interval $[-1, 1]$. The grid step is $\Delta x = 1$, and consequently, the time increment has been chosen as $\Delta t = 0.01$ to ensure numerical stability. The problem is completed by the choice of periodic boundary conditions, that is, on a toroidal topology. As shown in Fig. 3.1, the spinodal decomposition of the binary mixture starts soon in the simulation, resulting in two main routes of domain growth and interface minimisation: one is the merging of domains of a same phase (Fig. 3.2), and the second is the mechanism of Ostwald ripening (Fig. 3.3), the latter being a process of absorption of smaller bubbles into bigger ones by diffusion through the interface [39]. These two mechanisms are observed in real experiments as characteristic features of phase separation dynamics, thus at least qualitatively confirming the correctness of our simulations.

One general test we can perform on our results is computing the characteristic length of

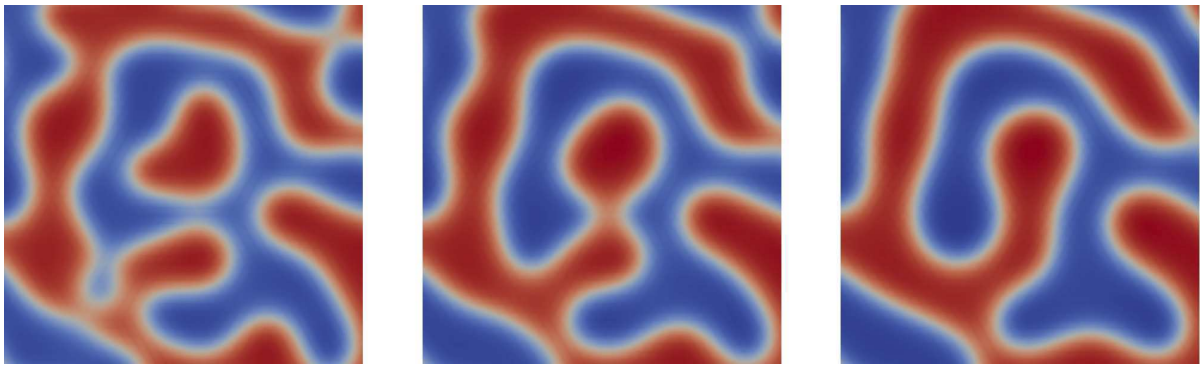

Figure 3.2: The merging of a bubble at the center of the image with a larger structure, from left to right.

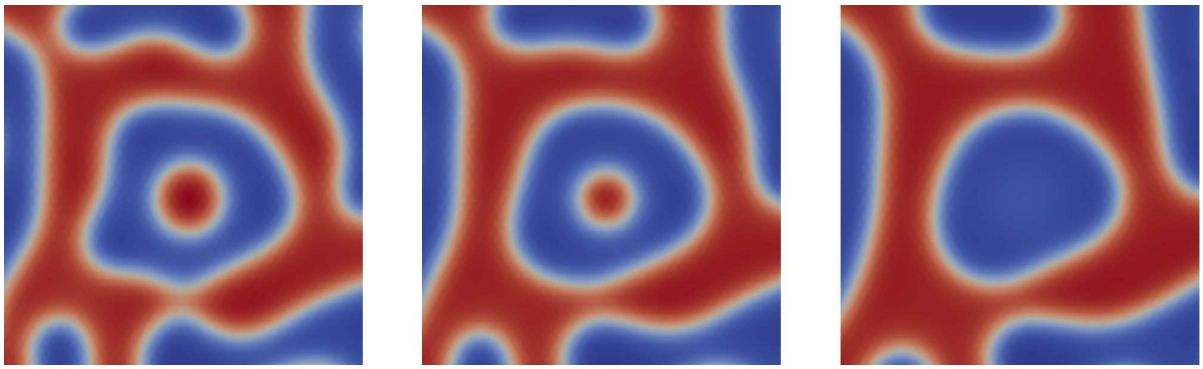

Figure 3.3: The vanishing of a bubble by diffusion through the interface (Ostwald ripening).

the domains as they evolve in time: in order to do this, we must compute the first moment of the structure factor of of φ. First thing we need are the Fourier components of the spatial distribution of the field φ:

$$\tilde{\varphi}_{m,n}(t) = \sum_{x=-l_x}^{l_x} \sum_{y=-l_y}^{l_y} \varphi(\mathbf{x}, t) e^{2\pi i \mathbf{x}\cdot\mathbf{k}},$$

where m, n are wavenumbers (obviously in finite number, hence a high-frequency cutoff is implicitly assumed) and $\mathbf{k} = (k_x, k_y)$ the wavevector, with $k_x = 2\pi m/l_x$, $k_y = 2\pi n/l_y$, l_x, l_y being the linear dimensions of the domain over which the spatial sum is performed. The square modulus of this sum is the structure factor $S_{m,n}(t) = |\tilde{\varphi}_{m,n}(t)|^2$, which serves as the generator function for the distribution of the wavevectors $\mathbf{k}$. This way we can compute the characteristic wavelength $L(t)$ at time t as the inverse modulus of the average wavevector:

$$L(t) = \frac{2\pi}{k(t)} = 2\pi \frac{\sum_{m,n} S_{m,n}(t)}{\sum_{m,n} |\mathbf{k}| \, S_{m,n}(t)}.$$

We expect from the Lifshitz-Slyozov theory [40] that this function of time be a power-law $L(t) \propto t^{1/3}$, and fitting the $L(t)$ data in Fig. 3.4 with the curve $L^\star(t) = L_0 + At^{\Gamma^\star}$ (note that the graph is in logarithmic time), we get an exponent $\Gamma^\star = 0.339 \pm 0.006$, clearly compatible the theoretical value 1/3.

3.2.3 Finite difference algorithms on curved surfaces

Now that we have verified the effectiveness of finite difference algorithms in reproducing the features of the Cahn-Hilliard model on flat surfaces, we shall proceed to extend it to a curved geometry. We restrict our study to spherical topologies, more suited to represent biological vesicles such as cells, and use a minimal coupling to adapt the Cahn-Hilliard equation to the new landscape, i.e. without assuming any explicit dependence on curvature for now. As a first step, we need to implement the covariant form of the differential operators: essentially, we need to introduce a correction term to vector quantities like gradients, in order preserve the

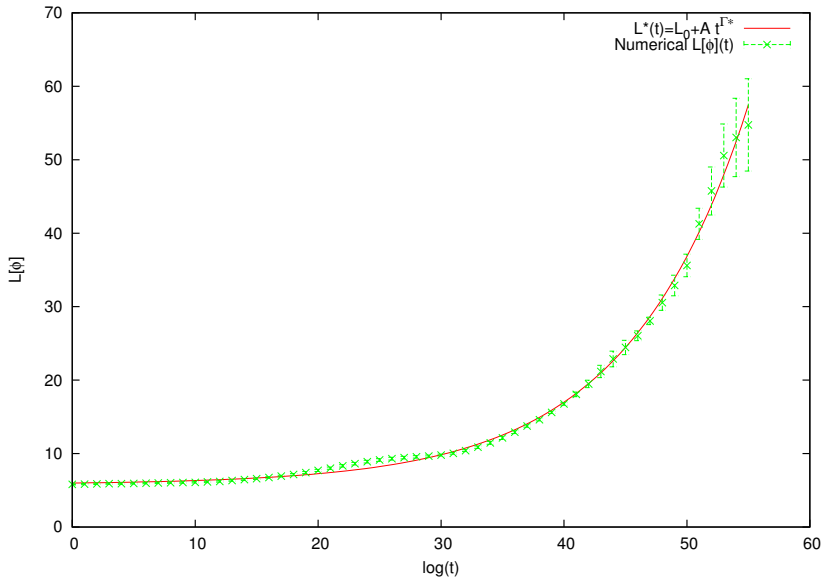

Figure 3.4: Time evolution of the structure factor of φ: the fitted power law coincides with the theoretical result.

direction of the vectors along a closed curve on the surface.

Given a set of local reference frames for each grid point as defined in chapter 2, we can use them to compute discrete derivatives. Since the grid we are now using is not homogeneous as in the flat case, we must use the version of finite difference algorithms for nonuniform grids, derived as the ones presented in section 3.2.1 under the assumption that the forward and backward increments around point V_i are not of equal length and in general not parallel (Fig. 3.5). If the two different increments in the oriented direction u are of different lengths $\Delta u_1, \Delta u_2$ in the order given by the orientation, the second order central finite difference will read

$$\frac{\delta f}{\delta u}(V_i) = \frac{\Delta u_1 f\left(u + \Delta u_2\right) - \left(\Delta u_1 + \Delta u_2\right) f(u) + \Delta u_2 f(u - \Delta u_1)}{\Delta u_1 \Delta u_2 \left(\Delta u_1 + \Delta u_2\right)}.$$

Since in the covariant version of the Laplace-Beltrami operator (2.6) an explicit gradient term

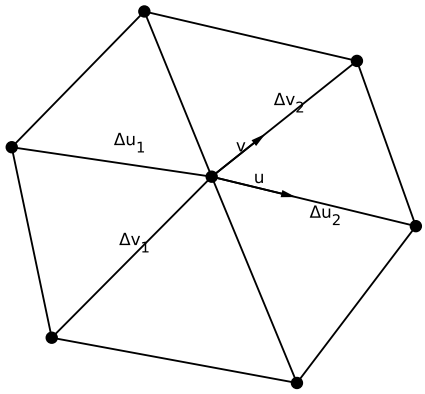

Figure 3.5: The local grid geometry around a grid point: the backward and forward increments are in general not equal nor parallel on a nonuniform grid.

$\partial_\rho \varphi$ appears, we need also the formula for first order finite difference:

$$\frac{\delta f}{\delta u}(V_i) = \frac{{\Delta u_1}^2 f\left(u + \Delta u_2\right) + \left({\Delta u_2}^2 - {\Delta u_1}^2\right) f(u) + {\Delta u_2}^2 f(u - \Delta u_1)}{\Delta u_1 \Delta u_2 \left(\Delta u_1 + \Delta u_2\right)}.$$

Note that the more the contiguous segments of lengths Δu_1 and Δu_2 are parallel, the more the algorithm is reliable. This depends both on the ratio between the local radius of curvature of the surface and the length of a single edge, and on the local distortion of the triangular meshes. In fact, even if we choose a very small scale for the edges, we will have errors which depend on the local connectivity of the grid. Specifically, since our construction starts from a regular icosahedron, which is the dual polyhedron of a dodecahedron, we have 12 vertices which have 5 first neighbours instead of 6. Since a pentagon does not bear central symmetry, there cannot be pairs of edges meeting at i lying on the same geodesic of the surface. This gives rise to two main issues: it forces us to discard altogether the central finite difference algorithm presented so far when working on the vertices with 5 first neighbours, and produces distortions in the shape of the hexagonal cells which lie in proximity of the pentagonal ones, .

A workaround to the first problem relies on the choice of a forward difference algorithm

instead of the central finite difference one. Since each edge of the pentagonal cell is shared by a hexagonal cell as well, we can perform the differentiation along the two subsequent edges along the outward direction from the vertex (Fig. 3.6). This allows to compute the value of the derivative at the point, again by averaging the values of the operators along all of the defined local frames. We must be aware though that this algorithm is one order less precise than the central finite difference scheme. The expression follows again from Taylor expansion of the function around a vertex V_i along direction u, and it reads

$$\frac{\delta f}{\delta u}(V_i) = -\frac{\Delta u_2(2\Delta u_1 + \Delta u_2)f(V_i) + (\Delta u_1 + \Delta u_2)^2 f(V_i + \Delta u_1) - {\Delta u_1}^2 f(V_i + \Delta u_1 + \Delta u_2)}{\Delta u_1 \Delta u_2(\Delta u_1 + \Delta u_2)},$$

for the first derivative, and

$$\frac{\delta^2 f}{\delta u^2}(V_i) = 2 \cdot \frac{\Delta u_2 f(V_i) - (\Delta u_1 + \Delta u_2)f(V_i + \Delta u_1) + \Delta u_1 f(V_i + \Delta u_1 + \Delta u_2)}{\Delta u_1 \Delta u_2(\Delta u_1 + \Delta u_2)}$$

for the second derivative.

The second issue, i.e. the local distortion, can be mitigated by adopting a method of grid refinement. The basic idea is to isolate the local feature of the grid that influences the error on the finite differences, and to change the positions of grid points to achieve a reduction of the main contributor to the error, that is the misalignment of contiguous edges, i.e. the deviations of the faces from equilateral triangles. As can be seen from Fig. 3.7A, angular distortion increases as we get closer to the five-fold points - but exactly on these points there is perfect symmetry.

The method we choose to mild this effect is a simple spring relaxation of the grid: we replace the edges of the grid with springs of unitary elastic constant, and set the masses of the grid points to 1. The force acting on vertex i is then the sum of all of the contributions of the springs connected to it:

$$\mathbf{F}_i^{el}(t) = \sum_{j \in \langle i \rangle} |\mathbf{x}_i(t) - \mathbf{x}_j(t)|,$$

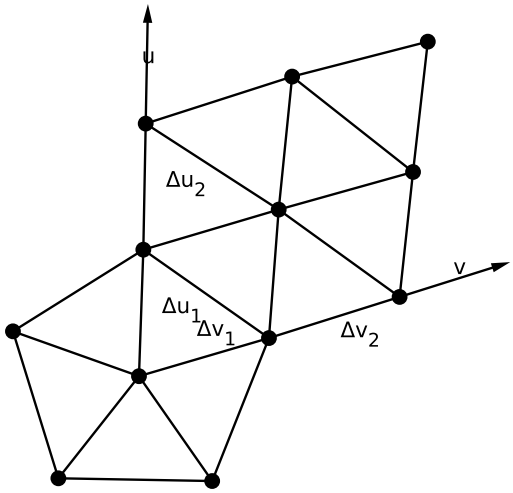

Figure 3.6: The geometry of a point with 5 neighbours: the directions of differentiantion are prolonged onto the neighbouring 6-cell.

where $\langle i \rangle$ represents the set of first neighbours of point i. The update of the position of grid points should be given by the acceleration produced by this force, but in order to make the relaxation converge we need a damping force proportional to the velocity at time t via a constant γ. Then, the velocity of the particle at time $t + \Delta t$ is given by

$$\mathbf{v}_i(t + \Delta t) = \mathbf{v}_i(t) + \Delta t \left(\mathbf{F}_i^{el}(t) - \gamma \mathbf{v}_i(t) \right).$$

Notice that the velocity at time t appears twice, and it vanishes if $\Delta t \cdot \gamma = 1$: therefore, if we choose the damping constant to take the (large) value $\gamma = 1/\Delta t$, we obtain an overdamped version of the dynamics, in which the velocity is only proportional to the elastic force. This in turn affects the the update of the positions of grid points, so that we obtain the simple rule:

$$\mathbf{x}_i(t + \Delta t) = \mathbf{x}_i(t) + \Delta t \mathbf{F}_{el}(\mathbf{x}_i(t)),$$

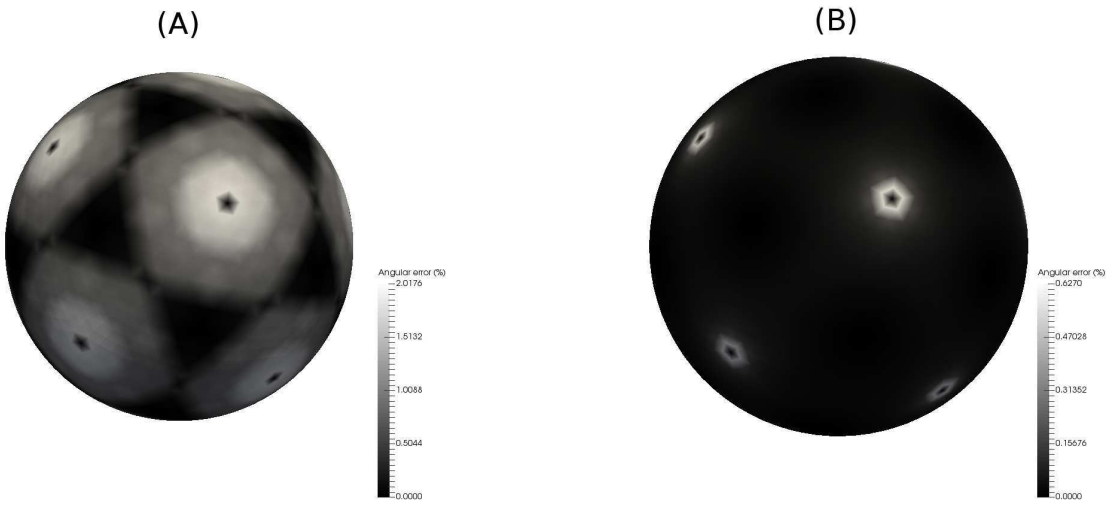

Figure 3.7: The map of the percentage of asymmetry of the triangles surrounding each point with respect to perfect rotational symmetry: in (A) we show the angular distortion of the starting geodesic grid, in (B) the reduced errors after grid refinement.

up to an appropriate rescaling of timestep Δt. As shown in [41], the optimal resting length of the springs is $\ell_0 = \beta\lambda$, where β is a control parameter, and λ the characteristic length of the edges, given on a unit radius sphere by

$$\lambda = \frac{2\pi}{10 \cdot 2^{m-1}},$$

where m is the level of refinement of the grid following the discretisation explained above. For best reduction of the grid distortions, a value of the control parameter $\beta = 1.2$ is assumed, leading to a significant reduction in local distortions (see Fig. 3.7B).

In these simulations we need to evaluate the action of the Laplace-Beltrami operator on a scalar field φ. If we choose a reference frame formed by the vectors $\mathbf{e}_1^{ij} = \mathbf{x}_j - \mathbf{x}_i$, $\mathbf{e}_2^{ij} = \mathbf{x}_{j+1} - \mathbf{x}$, we can compute a local estimate of the metric tensor through equation (2.4):

$$g_{\mu\nu}(ij) = \partial_\mu \mathbf{e}_\mu^{ij} \cdot \partial_\nu \mathbf{e}_\nu^{ij},$$

where ∂_μ stands for the appropriate finite difference in the direction of $\mathbf{e}_\mu^{ij}$. Using expression (A.2) from appendix A, we can obtain a formula for computation of the discrete version of the affine connection in the local frame:

$$\Gamma^\rho_{\mu\nu}(ij) = g^{\rho\sigma}(ij)\partial_\mu\partial_\sigma\mathbf{e}^{ij}_\mu \cdot \partial_\nu\mathbf{e}^{ij}_\nu.$$

In chapter 2 we derived expression (2.6) for the Laplace-Beltrami operator, that together with the expression for the metric and the affine connection we just showed, produce an output value of $\nabla^2_{LB}\varphi$ on vertex i given by

$$\left\langle \nabla^2_{LB}\varphi \right\rangle_i = \sum_{j\in\langle i\rangle} g^{\mu\nu}(ij)\left[\partial_\mu\partial_\nu\varphi - \Gamma^\rho_{\mu\nu}(ij)\partial_\rho\varphi\right].$$

3.2.4 Simulations on closed surfaces

Once we have performed all the steps we need to transport our equations to a curved space, we can proceed to the simulations. We recall that the minimal coupling we performed in our adapted equation does not include any explicit curvature terms in the equation of motion, and accordingly, no association of a particular phase with areas of higher curvature is observed in the simulations: the phase domains will just adapt to the surface to occupy the same areas and have the same interface length they would have on a flat plane. The covariant derivation is needed exactly for this reason: if it were not corrected with the additional affine connection, the consequently inconsistent differential operators we would get, would produce different shapes and sizes depending on the local curvature of the surface.

3.2.5 Results

We performed our simulations on a spherical surface, and two different ellipsoidal surfaces. In all cases the time interval was $\Delta t = 0.01$, and the radii or minor axes of the surfaces were set to $R = 18.9$, so that the smallest edge was of unitary length, to ensure numerical stability.

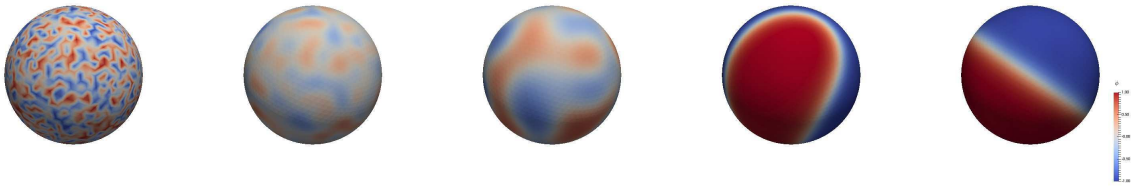

Figure 3.8: Phase separation on a sphere: snapshots in $\log(t)$ from an initial random configuration (left) to a complete separation (right). The interface at the steady state coincide with a geodesic circle, whose orientation is determined only by initial conditions - therefore, the symmetry group of the steady state is the 2-dimensional group $\mathbb{S}^2$ of rotations on a sphere.

In Figure 3.8 we show the evolution of φ on a spherical surface of radius R. As can be seen following the timelapse, the coarsening dynamics and the formation of phase domains is similar to the one observed on a flat space, ending up in a bipartition of the surface, with the interface line following a geodesic of the surface. Note here that if the profile of φ is measured along the normal direction u to the interface line, one obtains a curve compatible with the analytical solution in d=1 flat space - see Fig. 3.9.

When the dynamic occurs on an ellipsoid, the asymmetry of the surface imposes the direction of the interface to coincide with an umbilical geodesic: on an oblate ellipsoid, the geodesics of minimal length are the cycles orthogonal to the minor axis, so that the steady state configurations can be plotted to a plane (Fig. 3.10); on a prolate ellipsoid, the minimum interfacial length is reached when the interface coincides with the umbilical curve orthogonal to the major axis (Fig. 3.11).

3.3 Effect of curvature on phase separation: arrested coarsening

Until now we have studied the classic Cahn-Hilliard system on curved surfaces, without any explicit coupling to the underlying surface. We now want to investigate the effects that the local geometry of the surface can induce on phase separation. This is done by assuming a

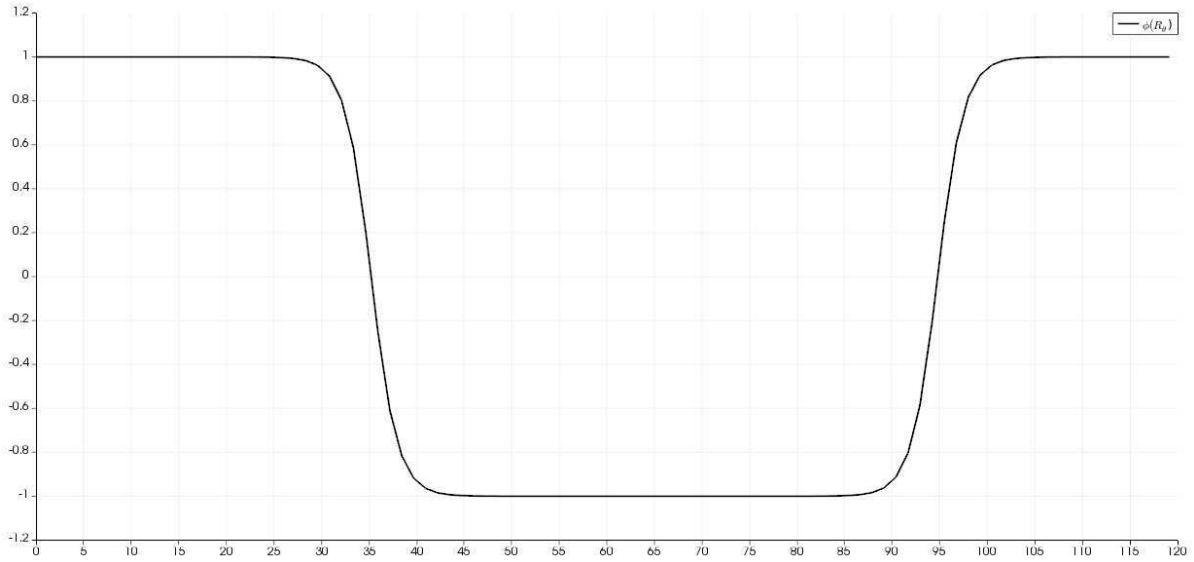

Figure 3.9: Plot of φ along a geodesic circle normal to the interface between A and B. The profile is compatible with the shape of the interface on a flat space.

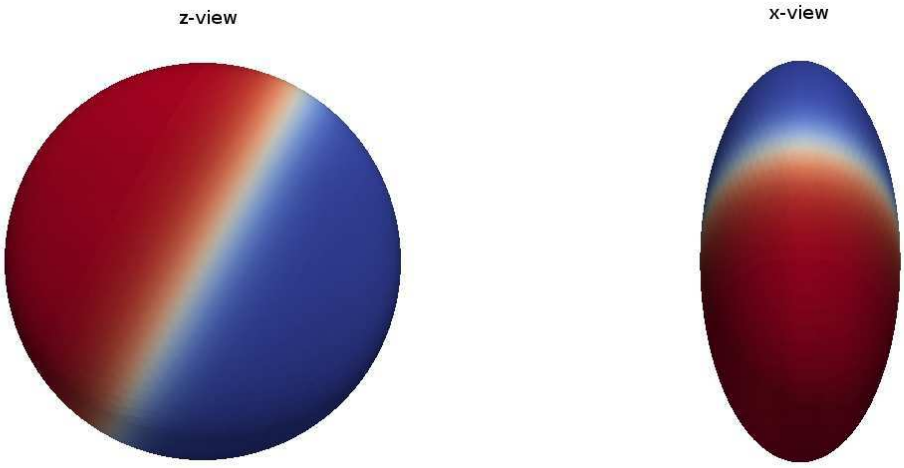

Figure 3.10: Steady state of a binary mixture on an oblate ellipsoid: the interfacial curve can be any geodesic cicle normal to the z axis, thus being symmetrical with respect to the 1-dimensional group $\mathbb{S}^1$ of the rotations in the (x, y) plane.

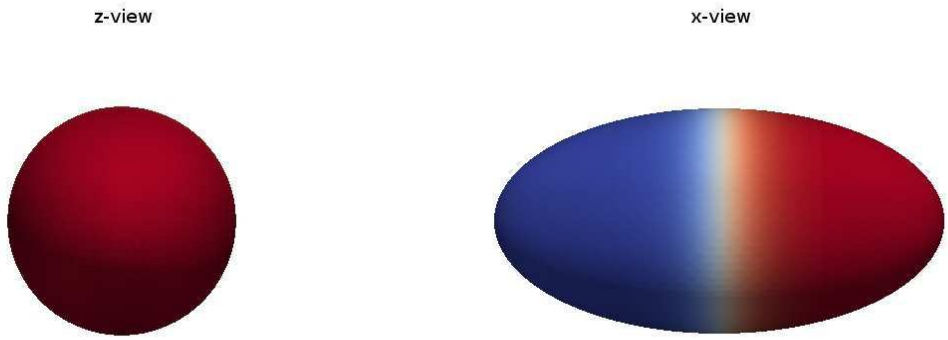

Figure 3.11: Steady state of a binary mixture on a prolate ellipsoid: the interfacial curve can only coincide with umbilical geodesic normal to the major axis, and the only symmetry of the steady state is the reflection across the (x, y) plane - or equivalently, the reflection $\varphi \to -\varphi$.

binary mixture that has an additional term in the free energy that couples the order parameter with the curvature of the surface. This simple coupling implies that the two phases have opposite affinities with the local curvature of the membrane: while they don't feel any effect on a minimal surface, there will be an attraction of one phase to the areas with higher curvature, and to the ones with lower curvature for the other phase. This can be justified if we think of protein complex whose shape fits better a more curved surface, and thus migrate from regions of lower curvature to regions of higher curvature [42, 43].

We will show that on a surface of nonconstant mean curvature, the effects induced by the newly introduced energy term can lead to effective arrest of the phase separation, thus leading to a steady state with more than one domain for each phase. This kind of dynamics is of interest in biophysics, because it provides a simple framework to explain the formation of inhomogeneous distributions in a variety of situations. On one hand, it constitutes a mechanism for pattern formation which does not rely on reactor-diffusion dynamics like in Turing patterns. On the

other hand, there are systems in which a process which clearly behaves like a Cahn-Hilliard mixture does not complete the coarsening, limiting the phase segregation to a certain finite time [29, 30].

3.3.1 Arrested Phase Separation on lipid membranes

The occurrence of phase segregation between liquid ordered and liquid disordered phases on phospholipidic has been proved experimentally on model membranes when sterols are added to binary mixtures of immiscible lipids [29, 30, 31, 32]. However, the behaviour of living membranes is thought to differ from complete phase separation, and requires instead the arrest of the growth of the phase domains at a certain length scale, smaller than the radius of the vesicle. Several main mechanisms have been proposed by which this arrest of the phase separation might originate.

One hypothesis is that lipid rafts (i.e. the domains of cholesterol-rich domains of saturated lipids) appear on membranes close to the critical point of the fluid-fluid coexistence region: thus, the correlation length is large, but complete phase separation does not take place. Experimental measurements of the critical exponents on GMPVs in the vicinity of the critical temperature for miscibility of the lipid mixture have been shown to be compatible with this hypothesis, reconducing the behaviour of the membranes to the universality class of the 2D Ising model [44, 45, 46].

Although the near-criticality hypothesis is compatible with experimental measurements on model membranes, real biological vesicles are often not appropriately described as simple lipid leaflets enclosing homogeneous liquids; instead, the internal volume is crowded with viscoelastic structures affecting the mechanical behaviour of the membrane itself. Hence, a second line of thought considers the arrest of phase separation as the result of the coupling of the membrane with the cytoskeleton: in this scenario the formation of macroscopic domains is always suppressed, and the universality class is the 2D random-field Ising model, which does not support critical behaviour [47, 48, 49]. Experiments on model membranes coupled to an actin network

have confirmed the suppression of macroscopic phase separation [50].

The main limitation of these mechanisms is that they view the membrane as a flat, two-dimensional surface. Since biological membranes are inherently curved surfaces, the results obtained by the previous models may not apply to curved geometries. Thus another explanation is necessary, that takes into consideration the local shape of the membrane as a major contributor to the stabilisation of raft domains [51, 52]. The idea that regions of certain curvature attract specific lipid species has been proved experimentally on microfabricated lipid bilayers with curvature heterogeneities [53]. This mechanism is the one we chose in the construction of our model, because of the highly curved setting we use in the representation of the membrane.

3.3.2 Coupling to surface curvature

The free energy functional we consider is given by

$$\mathcal{F}[\varphi, H] = \int d^2x \left[\frac{1}{4}\varphi^4(\mathbf{x}) - \frac{1}{2}\varphi^2(\mathbf{x}) - \kappa\nabla^2\varphi(\mathbf{x}) + cH(\mathbf{x})\varphi(\mathbf{x}) \right],$$

where $H(\mathbf{x})$ is the local mean curvature. The sign of the coupling coefficient c determines whether the interaction between the positive phase and the higher curvature is attractive or repulsive (and the behaviour of the opposite phase is determined consequently). The dynamics is nontrivial though, and it produces different equilibria of the free energy and different regimes.

Let be c a positive constant, for simplicity, and let's us restrict our study to a region of the surface where the curvature is $H(\mathbf{x}) > 0$. If we look at the bulk free energy, as φ increases, the overall free energy increases: thus, with a positive coupling constant, phases and curvatures of opposite signs will be energetically pushed to come together. More specifically, we can look at the stationary points of the functional

$$f_c(\varphi) = \frac{1}{4}\varphi^4 - \frac{1}{2}\varphi^2 + cH\varphi, \tag{3.6}$$

which vary in number and values as we tune c from zero to a positive value. Clearly, if we set $c = 0$ (or equivalently, if the curvature is constantly zero), we recover the same equilibrium points found in the flat case, i.e. one unstable equilibrium for $\varphi = 0$ and two stable equilibria for $\varphi_\pm = \pm 1$.

Let's now tune c to a positive yet small value, say $c \ll H$. This will produce a small shift in the free energy, displacing the equilibria in the negative direction, as we now briefly prove. If we assume that the perturbation will act linearly on the equilibria, let $\overline{\varphi}$ be a stable equilibrium value in the flat environment, then with small positive c it becomes $\varphi^\star = \overline{\varphi} + \alpha c$. To determine the value of α we must plug it into the derivative of equation (3.6). If the result is zero up to a linear term in c, then $\varphi^\star$ is the new equilibrium. After a trivial calculation, we have $\alpha = 1/2$, so the new equilibrium is $\varphi^\star = \overline{\varphi} - c/2$, which confirms that the minimal points are displaced to the left, i.e. lower values of φ are preferred when the curvature is positive (see Fig. 3.12. Furthermore, substituting the $\varphi^\star$ value into eq. (3.6), we see that the minima of f_c will be displaced vertically, lowering the left one and raising the right one, thus making the latter metastable. In this regime, there might be a localisation of the phases in the regions of the preferred curvatures, but the driving force of the coarsening - the interfacial energy - still prevails over the curvature term, and the coarsening is not arrested if the surface has regions with different curvatures.

If we now increase c further, we reach a critical value $\overline{c}$ where the local minimum for positive φ disappears. To find it, we can exploit the fact that the inflexion points of the curve in φ are constant, regardless of the value of c. Since the second derivative of f_c is

$$f_c''(\varphi) = 3\varphi^2 - 1,$$

the flexes will be $\tilde{\varphi}_\pm = \pm\sqrt{3}/3$ for all values of c. This tells us that that in order to make the positive minimal value φ_m vanish, it must be made to coincide with the inflexion point. Thus, we can impose $\varphi_m = \sqrt{3}/3$, and since this is a minimal point, it must bring the first derivative

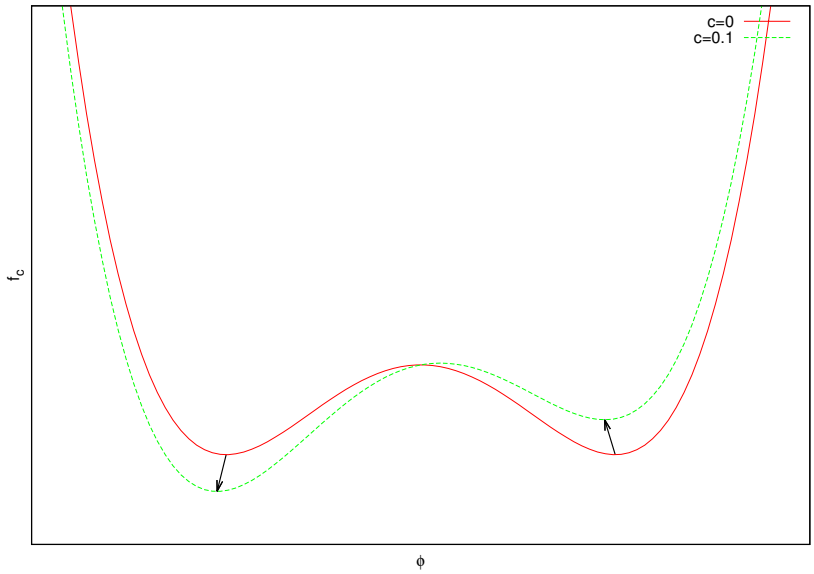

Figure 3.12: As shown in our computations, the minima of f_c are displaced when c is tuned from zero to a positive, yet small value.

of f_c to zero:

$$f'_{\overline{c}}(\varphi_m) = \varphi_m^3 - \varphi_m + \overline{c}H = 0.$$

Substituting the numerical value of φ_m leads to a linear equation in $\overline{c}$, which gives the critical value

$$\overline{c} = \frac{2\sqrt{3}}{9H},$$

in a region with locally constant curvature H. With $c \geq \overline{c}$, only one of the two phases is allowed in a region with nonzero curvature, thus effectively implementing an arrest of the coarsening: if two domains of phase A are separated by a region of high enough curvature, their merging will be prevented by the fact that phase A is prohibited in the space between them. Obviously, the region where the curvature is high enough for c to be critical needs to have a radius bigger than the interfacial width $\sqrt{\kappa}$. A study of the curvature of the surface will then be needed to understand the global $\overline{c}$ which allows to select the allowed phase in the different regions of the surface.

Note that the new equilibrium values of φ are not ± 1 anymore: this can be fixed by artificially limiting the domain of φ to $[-1, 1]$, by using it to represent something other than the difference between two concentrations, or modifying the bulk part of the free energy as

$$f_{a,b,c}(\varphi) = \frac{a}{4}\varphi^4 - \frac{b}{2}\varphi^2 + cH\varphi, \tag{3.7}$$

with a choice of a and b that allows the extremal values $-1; 1$ to be reached only in the regions with extremal curvature.

3.3.3 Results

The framework we used for the study of simple phase separation can be adapted to this modified version without particular issues. We only need to compute the mean curvature, which can be done by taking the trace of the matrix product of the second fundamental form and the inverse metric tensor:

$$H(\mathbf{x}) = \frac{1}{2} b_{\mu\nu}(\mathbf{x}) g^{\mu\nu}(\mathbf{x}).$$

In Fig. 3.13 we display the evolution of φ with supercritical c on a surface with a gaussian bump. After an initial regime in which the random initial fluctuations are smoothed out, phase segregation takes place, according to the shape of the surface.

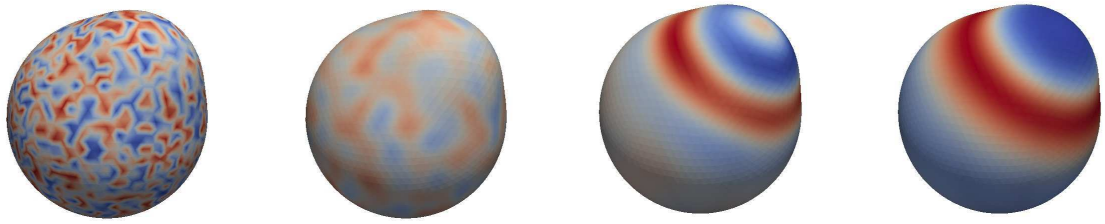

Figure 3.13: From left to right, we show the evolution of the phase separation with curvature coupling on a spherical surface with one gaussian bump. A ring-like structure is formed in the late stages of the dynamic, in the collar region of least curvature around the bump.

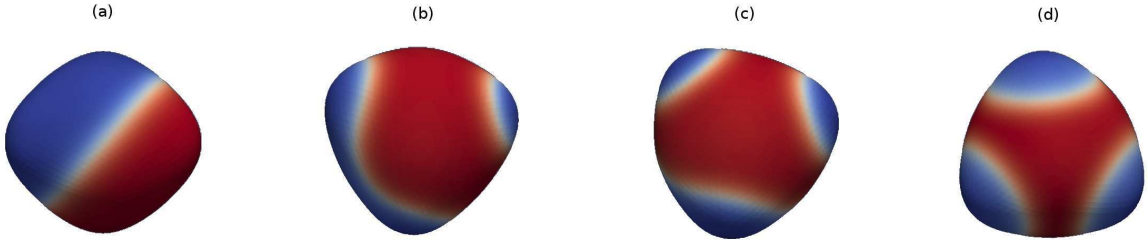

Figure 3.14: Final stage of phase separation for different values of c. In (a) the uncoupled version is used: since the shape of the surface is akin to that of the tetrahedron, there are three geodesics of minimal length, corresponding with the square intersections of the tetrahedron with a plane, and the interface at steady state coincides with one of these geodesics. In (b) a small value of c arrests the phase separation at a late stage, leaving only one bubble of phase B separated from the bulk; note that the interface is not of minimal length anymore, but follows curves on the surface along which the curvature is constant. In (c) the coupling is critical for regions of lowest curvature, but this still allows he presence of a narrow bridge of phase B connecting two of the domains corresponding to the gaussian bumps. In (d) a c is chosen which is supercritical for all of the regions of the surface, leading to complete arrest of the coarsening process.

In Fig. 3.14 we see the steady state of φ on a surface with four gaussian bumps disposed symmetrically, with increasing values of c. In frame (a), we have the conventional phase separation with $c = 0$; in (b) c is supercritical for the regions of highest curvature, but not for the ones with lower curvature, thus we have the formation of two domains of the B-rich (blue) phase, and one of the A-rich (red) phase; in (c) we have c at the critical value for the region of lower curvature, thus the B-rich phase is attracted to the regions of lower curvature, but not strongly enough to completely overcome the interfacial energy, thus creating three different domains of the B-rich, while in (d) a c is chosen, which is supercritical for all of the surface curvatures, thus allowing to see the full arrest of the coarsening, with one domain of A-rich phase and four bubbles of B-rich phase located in correspondence with the four bumpy protrusions.

Since we have seen that a coefficient $c \geq \overline{c}$ does not allow the existence of the positive phase, we want to check whether this mechanism could effectively stop also the process of Ostwald ripening of two bubbles. Let us put ourselves in 1D to simplify the calculations, without loss of generality: consider a landscape of uniform $\varphi \equiv -1$, with two regions of $\varphi = +1$ delimited

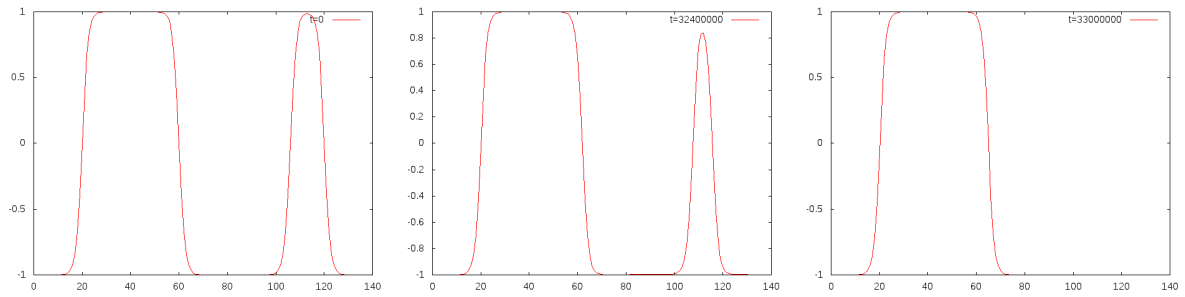

Figure 3.15: The bubble on the right is below a critical radius, thus it dissolves by diffusion through the interface, letting the bigger one on the left grow.

by the correct tanh interface. If one of the two $\varphi = +1$ regions is bigger than the other one, and the smaller one is below a critical radius, we can assume that the smaller one will vanish, producing a growth in the bigger one. We perform a simple simulation on a 1D grid with $\Delta x = 1$, covering the interval $[0, 140]$, with one bigger region of $\varphi = +1$ spanning the interval $I_1 = [20, 60]$, and a smaller one in the interval $I_2 = [106, 120]$. The timestep is set to $\Delta t = 0.01$ for numerical stability, and we complete the system with zero-flux boundary conditions, $\nabla\mu(0) = \nabla\mu(140) = 0$. The system evolves again using the 1D version of the finite difference algorithm presented in Chapter 3.1 to evaluate the laplacians, and the Adams-Bashforth-Moulton predictor-corrector. As seen in Fig. 3.15, the smaller bubble vanishes, while the bigger one extends its radius of an amount equal to the initial radius of the other one. This process lasts $t^\star = 3.3 \cdot 10^5 s$ in simulated time, i.e. $N_{t^\star} = 3.3 \cdot 10^7$ timesteps, after which the smaller bubble is no longer visible.

Let us now add an energy barrier that impedes the existence of the positive phase, say with a coefficient $c = 1/2$ and a hill in the 1D grid built in a way that the curvature has a gaussian bump of width $\sigma = 3$ centered in the mean point $\xi = 83$ between the two bubbles:

$$\mu(x) = \varphi(x)^3 - \varphi(x) - \kappa \frac{d\varphi}{dx}(x) + c\, e^{-\frac{(x-\xi)^2}{2\sigma^2}}.$$

When performing the simulation, we see that there is a depression in φ corresponding to

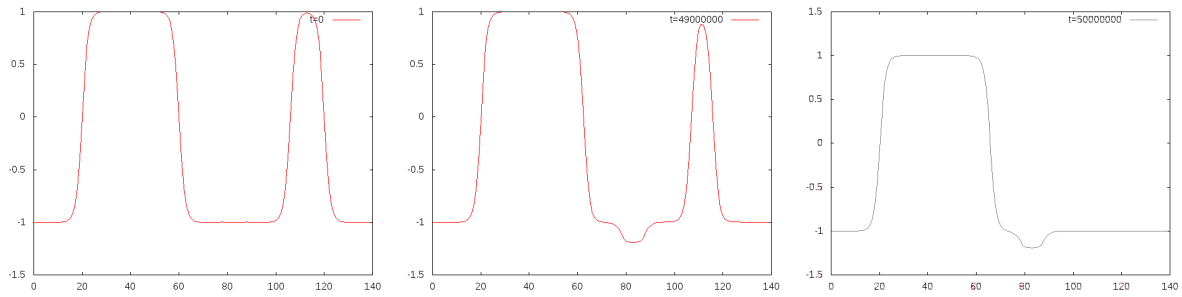

Figure 3.16: A supercritical energy barrier does not stop the coarsening by Ostwald ripening, but it considerably delays it, prolonging the total time needed for the smaller bubble to dissolve.

gaussian protrusion Fig. 3.16; the dynamics though is similar to the one seen in the $c = 0$ case, but with a longer absorption time - now it is $t^\star = 5.0 \cdot 10^5 s$ in simulated time. This means that though the phase $\varphi = +1$ is prohibited at equilibrium in the curved region, a flow of that phase is allowed through the obstacle, but it is slowed down by the presence of the barrier.

Chapter 4

Localised Patterning on Curved Membranes

Let there be a membrane with two lipid phases, which undergo spontaneous segregation, arrested by a coupling of a more fluid phase with regions of higher mean curvature. If there is a reaction-diffusion process taking place on the membrane, the different phases of the underlying lipid could influence the diffusivity of one or both the reactants. Thus, if we have a coupled activator-inhibitor system, it could be allowed to produce Turing patterns in the regions with higher H, and not in the regions with lower curvature. This scenario provides a simple model for the localisation of patterns on membranes in regions with specific curvatures. In this section, we will present in detail this model, studying the different patterning modes and their response to the shape of the membrane.

4.1 Turing Patterns

The reaction-diffusion model of pattern formation is a very popular system in biological science [54]. It is applied to the formation of chromatic patterns on the surface of living beings, as well as to the distribution of species in an environment or the sorting of proteins on a cell

membrane. The main idea is that the spatial inhomogeneity results from the competition of two fields with different diffusivities, let's call them an *activator* and an *inhibitor*, the former promoting the increase of both fields, the latter a decrease. If we call the activator u and the inhibitor v, we will have a system of two coupled equations, with a reaction and a diffusion part for each field:

$$\begin{cases} \dot{u} &= \gamma f(u,v) + \nabla^2 u \\ \dot{v} &= \gamma g(u,v) + D\nabla^2 v \end{cases},$$

where f and g denote two nonlinear functions of u and v which describe the reaction part, γ is a scale factor and D is the diffusion coefficient of the inhibitor, while the diffusivity of the activator is assumed to be unitary.

The mechanism by which the inhomogenous patterns are produced goes under the name of "diffusion-driven instability". It requires the stability of the steady states of the nondiffusive equation - i.e. the reaction part - which becomes unstable once the diffusion part is introduced. The unstable growth of the local disturbances is then controlled by the nonlinear part, letting the system converge to a configuration of regular spatial patterns. In our dissertation, we choose as a particular system the Gierer-Meinhardt model for pattern formation [55], whose equations are

$$\begin{cases} \dot{u} &= \gamma(u^2/v - \alpha u) + \nabla^2 u \\ \dot{v} &= \gamma(u^2 - v) + D\nabla^2 v \end{cases}.$$

The first thing that needs to be done is finding the equilibria of the nondiffusive equations, thus neglect the laplacians and the time derivatives. In our case, this produces the values

$$\overline{u} = \frac{1}{\alpha}, \quad \overline{v} = \frac{1}{\alpha^2}.$$

To determine the range of values of a that stabilise these equilibria, we need to impose the negativity of the eigenvalues of the stability matrix $\mathcal{M}$ formed with the partial derivatives of

f and g with respect to u and v

$$\mathcal{M} = \begin{pmatrix} 2\overline{u}/\overline{v} - \alpha & -\overline{u}^2/\overline{v}^2 \\ 2\overline{u}^2 & -1 \end{pmatrix} = \begin{pmatrix} \alpha & -\alpha^2 \\ 2/\alpha & -1 \end{pmatrix}.$$

To obtain negative eigenvalues, we require the trace of $\mathcal{M}$ to be negative, since it is equal to the sum of the eigenvalues, and the determinant to be positive, because it gives the product of the eigenvalues. These two requests produce the condition $0 < \alpha < 1$.

We then proceed to find the values of α and D that induce the instability: we need the stability matrix used before, but we now take its Fourier transform, to be able to deal with the laplacian terms. Spatial differentiation produces a term $-i\mathbf{k}$, where $\mathbf{k}$ is a wave vector, then the diffusive stability matrix is

$$\mathcal{M}_D = \begin{pmatrix} \gamma\alpha - k^2 & -\gamma\alpha^2 \\ 2\gamma/\alpha & -\gamma - Dk^2 \end{pmatrix}.$$

This time we require that at least one eigenvalue is positive, to induce instability. Since k, D and γ are positive and $0 < \alpha < 1$,, the trace of the matrix is always negative, thus there is at least one negative eigenvalue. This means that the only possibility to have a positive eigenvalue is for the determinant to be negative, implying that the two eigenvalues have opposite signs. The determinant of $\mathcal{M}_D$ is a quadratic function $h(k^2)$:

$$h(k^2) = Dk^4 - k^2\gamma(D\alpha - 1) + \gamma^2 a.$$

In order for an instability to exist, there must be a range of k^2 where $h(k^2)$ is negative, and this is possible if $D\alpha > 1$. This condition, however, is not sufficient: an instability region exists if the minimum of the curve $h(k^2)$ is negative, so we find the critical wavelength k_c^2 setting the

derivative to zero

$$0 \equiv h'(k_c^2) = 2k_c(2Dk_c^2 - \gamma(D\alpha - 1)) \qquad \Longrightarrow \qquad k_c^2 = \frac{\gamma(D\alpha - 1)}{2D},$$

so that the minimum undergoes the condition

$$h(k_c^2) = \gamma^2 \left[\alpha - \frac{(D\alpha - 1)^2}{4D}\right] < 0 \qquad \Longrightarrow \qquad (D\alpha - 1)^2 > 4Da.$$

So, in the end the conditions for pattern formation sum up to the following system of inequalities:

$$\begin{cases} 0 < \alpha < 1 \\ D\alpha > 1 \\ (D\alpha - 1)^2 > 4D\alpha \end{cases} . \tag{4.1}$$

4.1.1 Varying diffusion coefficient

The conditions (4.1) ensure that stable spatial patterns are formed, and the characteristic length of the patterns is determined by the range of k^2 for which $h(k^2)$ is negative. We now want to study what happens if the diffusion coefficient D satisfies the conditions above only in certain regions of the domain. Specifically, we picture a situation similar to the one described at the beginning of this section, with the diffusivity of the activator being dependent on the concentration of a fluid phase.

Let then φ be the concentration of the substrate that influences the diffusivity of the activator u in a system exhibiting Turing patterns as the one described in the previous section. If φ undergoes a coarsening as the one described in section 3.1, then there are again two stable phases $\varphi = \pm 1$. According to the third inequality of conditions (4.1), there is a critical diffusivity $D_c = 3 + 2\sqrt{2}$ which separates the homogeneous steady state from the patterning regime. In our new scenario we want the diffusivity to vary around this critical value, with an amplitude of variation ΔD, so that the value $D_c + \Delta D/2$ is reached when $\varphi = +1$ and

$D_c - \Delta D/2$ when $\varphi = -1$. A smooth function which satisfies these requirements is the sigmoid function

$$D(\varphi) = D_c - \Delta D + \frac{1}{1 - e^{-\nu(\varphi - \varphi_0)}} \tag{4.2}$$

where φ_0 is the unstable equilibrium between the two phases of φ (zero in our case) and ν determines the sharpness of the transition - which becomes a step function centered in φ_0 in the limit $\nu \to \infty$.

4.1.2 Phase segregation determines the position of patterns

Now that we have introduced the dependence on φ, we can study what happens when φ follows the phase separation dynamics we have described. The system is described completely by three partial differential equations, one for the phase separation and two for the pattern formation:

$$\begin{cases} \dot{\varphi} &= M\nabla^2\left(a\varphi^3 - b\varphi - \kappa\nabla^2\varphi\right) \\ \dot{u} &= \gamma(u^2/v - \alpha u) + \nabla^2 u \\ \dot{v} &= \gamma(u^2 - v) + D\nabla\cdot(D(\varphi)\nabla v) \end{cases} . \tag{4.3}$$

Note that in the PDE for the inhibitor the Laplacian has been substituted by the divergence of the flux $\mathbf{j} = D(\varphi)\nabla v$. We start by studying the evolution of the system on a flat surface with periodic boundary conditions, as in section 3.1.

4.2 Dynamics on a flat surface

To begin with, we consider the dynamics of the system on a flat surface. Numerical integration of equation (4.3) has been performed on a triangular grid of $N = 8686$ points with periodic boundary conditions and by using the Adams–Bashforth–Moulton predictor–corrector method for the time evolution with time step $\Delta t = 0.01$. Fig. 4.1 shows the time evolution of the φ field and of the activator field u : it is apparent that patterning occurs either in the A-rich phase regions ($\varphi = +1$) or very close to it: these are the regions where the value of $D(\varphi)$ is large

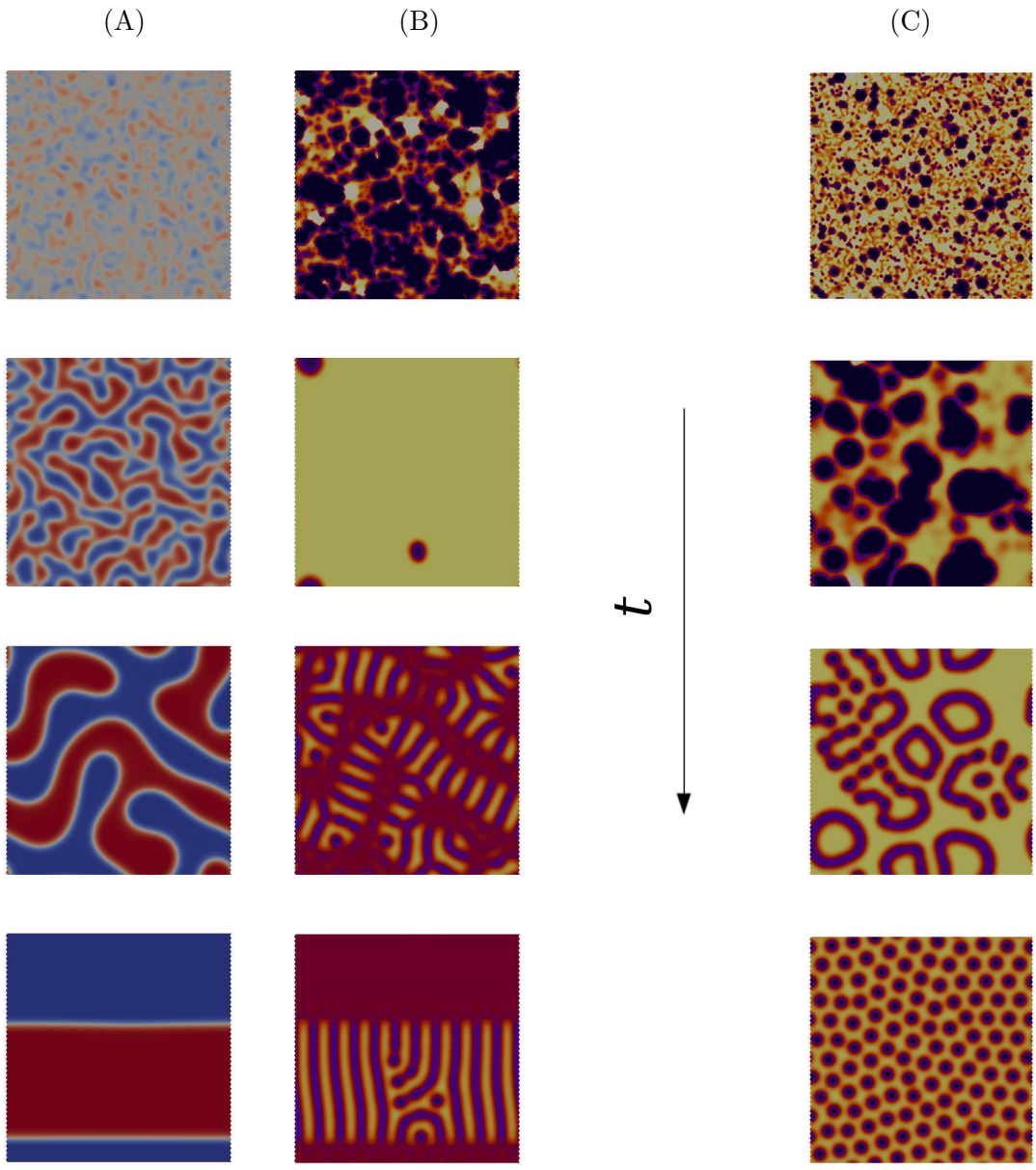

Figure 4.1: Computed dynamics with periodic boundary conditions on a plane. (A) Snapshots of the Cahn-Hilliard phase separation dynamics for φ, starting from an initial random configuration. (B) Plots of the activator field u in the Gierer-Meinhardt equations, with a diffusion coefficient coupled with φ. The uncoupled (constant diffusivity) dynamics of the activator is shown in sequence (C) for comparison. The parameter of the Cahn-Hilliard dynamics is $\kappa = 4$; the diffusivity function is characterised with a variation $\Delta D = 10$, and a sharpness $\nu = 10$. In all the figures the color scale of the patterning dynamics ranges from 0.1 (purple) to 4.5 (white) whereas the one referring to the coarsening dynamics ranges from $\varphi_- = -1$ (blue) to $\varphi_+ = +1$ (red).

enough to trigger a diffusion-driven instability in the Turing equations. More interestingly, by comparing the kinetics of the simple Turing system with the one coupled to the phase separation dynamics, one observes that the φ-dependent diffusivity leads to a different selection of pattern type (stripes versus spots) and of wave-lengths. This can be quantified by computing the time evolution of the typical cluster size of the activator $L[u](t)$ as the first moment of the structure factor Fig. 4.2. In particular, for the Turing system, one observes an initial fast (exponential) growth, followed by a decay, due to the nonlinear component of the equation that stabilises the Turing pattern, to the typical length of the resulting spatially modulated steady-state. Notice that in the coupled case the small time dynamic is characterised by very small fluctuations of $L[u]$. This is because the spatial configuration of the reactants becomes progressively homogeneous until the droplets of the pattern-allowing phase become large enough for the patterning to initiate. On the contrary, after this initial regime, the fluctuations become more important than in the uncoupled case. This is due to the heterogeneity of the domains size, to the shrinking of some patterns by Ostwald ripening and the change in shape of the growing domains. The interplay between coarsening and patterning dynamics can be further explored by looking also at the extreme case in which the binary mixture coarsening is much faster then pattering (see bottom panel of Fig. 4.2). In particular we choose the extreme situation in which patterning occurs on a completely phase separated binary mixture. In this case the fluctuations of $L[u]$ are less pronounced since the patterning dynamics occurs on an equilibrated (i.e. phase separated) substrate. In both coupled cases the stationary state value of $L[u]$ is higher than in the simple (i.e. uncoupled) Turing system indicating the selection of a striped pattern rather than a more closely packed, spotted one. The fluctuations in the scale length of φ at steady state are caused by the fact that there are a few possible steady state configurations: either a circular domain of one phase within the other, or two parallel rectangular domains of the two different phases.

The difference between the coupled and uncoupled dynamics gives also rise to a distinct resolution of defects: while defects disappear altogether in the uncoupled model (Fig. 4.1C),

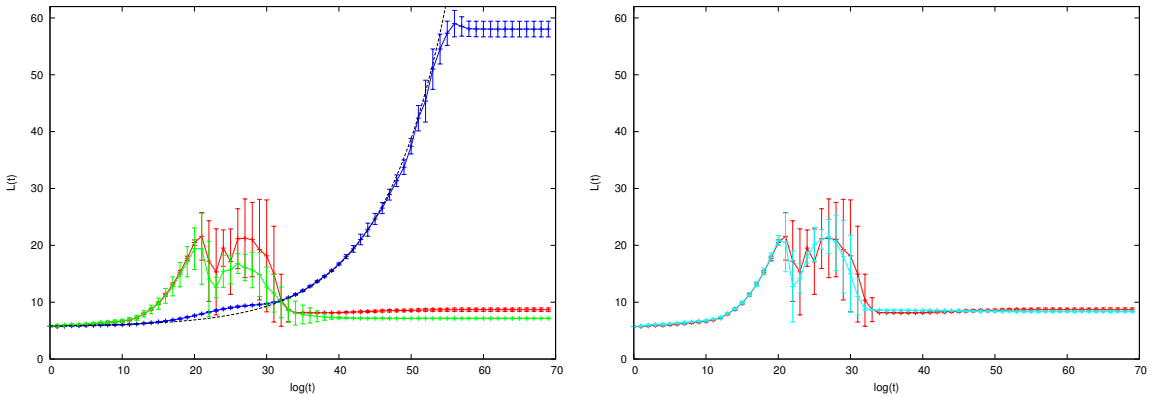

Figure 4.2: Time evolution of the length scales of the interacting fields of Fig. 4.1. (Left panel) The growing blue curve refers to the length scale of the binary mixture phases, L[φ], undergoing the coarsening dynamics of Fig. 4.1A. Its behaviour is in agreement with the standard Cahn-Hilliard (model B) dynamics in finite domains. Indeed L[φ] grows with time as $t^{1/3}$ (see dashed curve) until it reaches the system size. The red and green curves refer instead to the typical length scale of the Turing patterns, $L[u]$, evolving respectively with the coupled (Fig. 4.1B) and uncoupled (Fig. 4.1C) dynamics: the deviation of the two curves in the long time limit reflects the change between the striped (Fig. 4.1B) and the spotted (Fig. 4.1C) patterns. In the right panel we compare the time evolution of the Turing patterns length scale $L[u]$ in the coupled case when the Cahn-Hilliard coarsening is either comparable (red curve) or much faster (cyan curve) than the reaction-diffusion dynamics. In all cases the size of the bars (proportional to the fluctuations of $L[u]$) have been computed as the statistical error over 16 simulations.

defect annealing can be imperfect in the coupled version (Fig. 4.1B). This is because in the latter case defects may arise en route to steady state due to coarsening, for example when two domains with different internal stripe orientation merge. In the case of a larger domain, the boundaries of the pattern-allowing region are too far apart, so that the patterns are not constrained in a striped configuration in the whole domain, and the defects which are far enough from the boundaries are free not to cancel out. However, in a sufficiently small domain, the closeness of the boundaries forces the final configuration into the most symmetric one commensurate with the periodicity at the boundaries. In this case, if we choose a smaller domain for the simulation, evenly spaced stripes are formed at equilibrium (see Fig. 4.3).

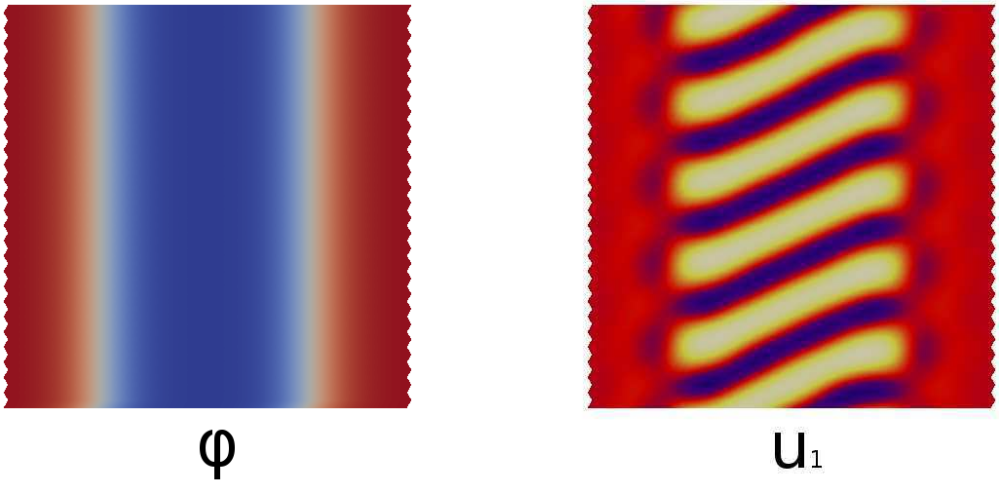

Figure 4.3: In a smaller domain, the patterns which result at equilibrium are stripes without internal defects. This happens because the influence of the boundaries extends throughout the whole patterning region, i.e. the transversal size of the domain is not much larger than the characteristic length of the patterns.

4.3 Dynamics on curved surfaces

We now turn to the curved case. The equations are equal to the (4.3), with the difference that the laplacians are replaced by the Laplace-Beltrami operators, and the gradients in the third equation are replaced with covariant derivatives. If we want to guide the patterns to regions with a specific curvature, we must insert the dependence in the free energy, as in section 3.3.2. The modified system of equations will then be

$$\begin{cases} \dot{\varphi} &= M\nabla^2\left(a\varphi^3 - b\varphi - \kappa\nabla^2\varphi + cH\right) \\ \dot{u} &= \gamma(u^2/v - \alpha u) + \nabla^2 u \\ \dot{v} &= \gamma(u^2 - v) + D\nabla\cdot(D(\varphi)\nabla v) \end{cases} . \tag{4.4}$$

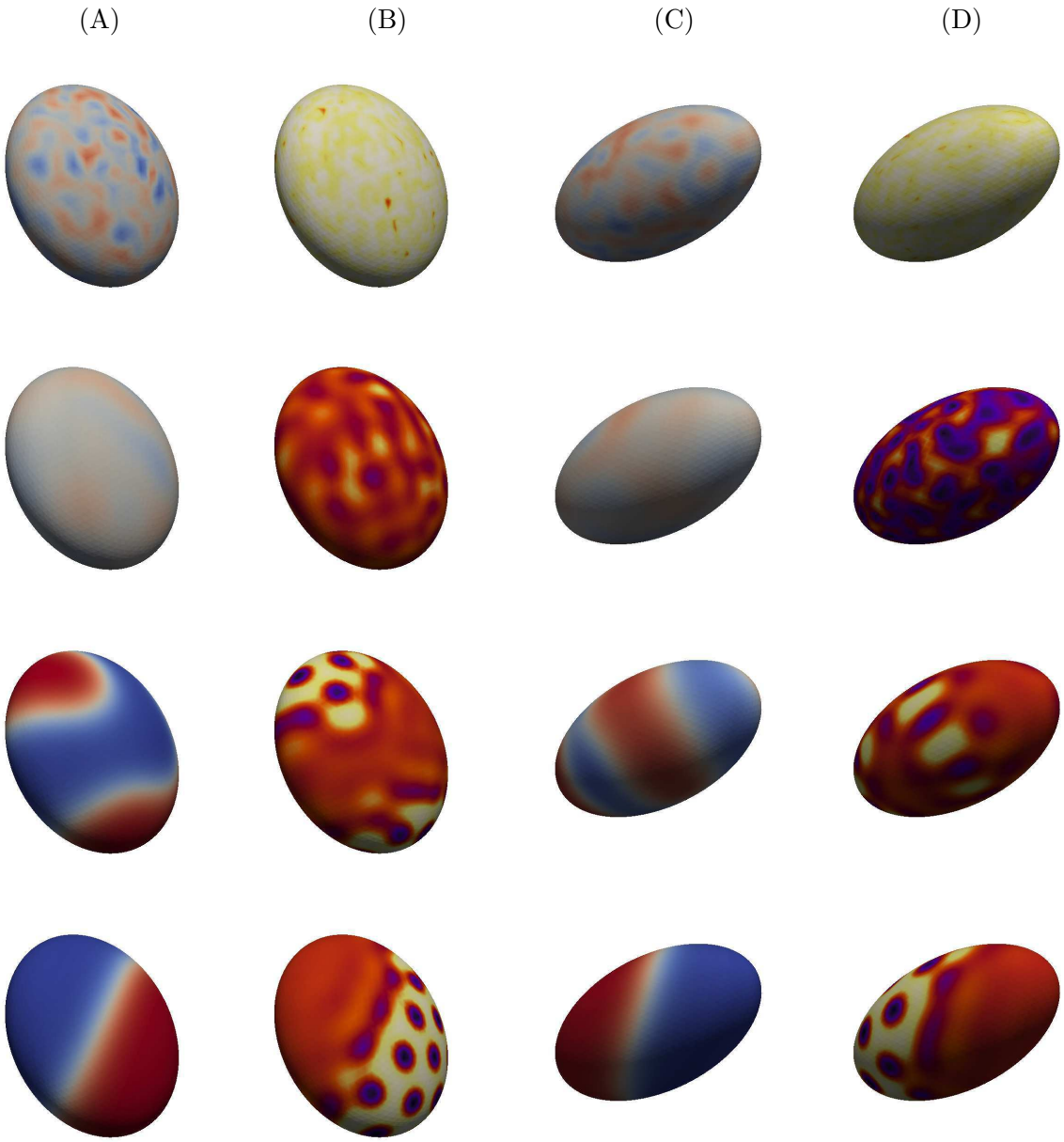

Figure 4.4: Dynamics on an ellipsoidal geometry. (A) displays the evolution of φ on an oblate ellipsoid, (B) is the corresponding u; (C) and (D) are analogous sequences for φ and u respectively, on a prolate ellipsoid.

Let's then apply these equations to curved surfaces, beginning with an ellipsoidal geometry (either rod-like, prolate, or disc-like, or oblate). These simulations are more demanding in view of the anisotropic nature of the surface: we therefore used a less refined grid with $N = 2562$

points but with a much smaller integration time step $\Delta t = 0.001$.

We note here that the length scale of the structures is completely determined by the parameters of equations (4.4) and by the curvature profile of the surface. The thickness of the interface of the phase domains in the modified Cahn-Hilliard equation is determined by the coefficient κ as in the flat case, and the size of the domains is set by the relationship between the intensity of the curvature term c and the level curves of the curvature H. On the other hand, the characteristic length of the patterns formed is selected by the choice of the scale constant γ in the reaction-diffusion equations. In order to make the results of the simulations independent of the resolution of the discretised membrane, we chose the set of parameters $\kappa = 4$, $\gamma = 4$, on surfaces with the sizes already used in chapter 3.1. This allows to tune the sizes of the domains which are formed on the surface so that they always are much bigger than the maximum size of the edges of the surface.

4.3.1 Intrinsic curvature

First, we focus on the case of intrinsic curvature, where the coefficient c of the coupling is set to zero. As in the flat case, patterns appear quickly in regions of high φ (Fig. 4.4). We first neglect any explicit coupling of φ with the curvature of the surface. In this case the coarsening dynamics proceeds until phase separation is completed, irrespectively of the specific geometry of the surface, as already pointed out in previous works. It is important to note that the only difference between the flat environment and the uncoupled system on the ellipsoid is the geometry of the surface. Remarkably, this is enough to select different patterns in steady state (spots in the curved geometry, stripes in the planar one). The kinetics we observe on the curved surface may also show multiple switches between patterns; for instance on a prolate ellipsoidal geometry the Turing reactants first form clusters; these then evolve transiently into stripes, and eventually into spots (see Fig. 4.4).

4.3.2 Explicit coupling with curvature

A second case of interest is that in which the curvature directly enters the free energy, so as to model differential targeting of lipids to areas of high curvature. This geometric coupling can arrest coarsening in the Cahn-Hilliard dynamics, so that the number of "lipid" domains is larger than one in steady state (see Figs. 4.5, 4.6 and Suppl. Fig. 3). The number of domains in steady state depends on geometry: for instance we end up with two domains at the tip of a sufficiently prolate ellipsoid (see Fig. 4.5), whereas when modelling a sphere with Gaussian bumps, in steady state there may be as many domains as there are bumps (see Fig. 4.6A).

Note that, while the Turing fields do not affect the dynamics of the binary system, the formation of Turing patterns depends strongly on the lipid concentration. In particular the coupling between the Turing dynamics and phase separation drives the patterns to domains with large values of φ, where the diffusivity of the inhibitor is large; as a result, in Figs. 4.5

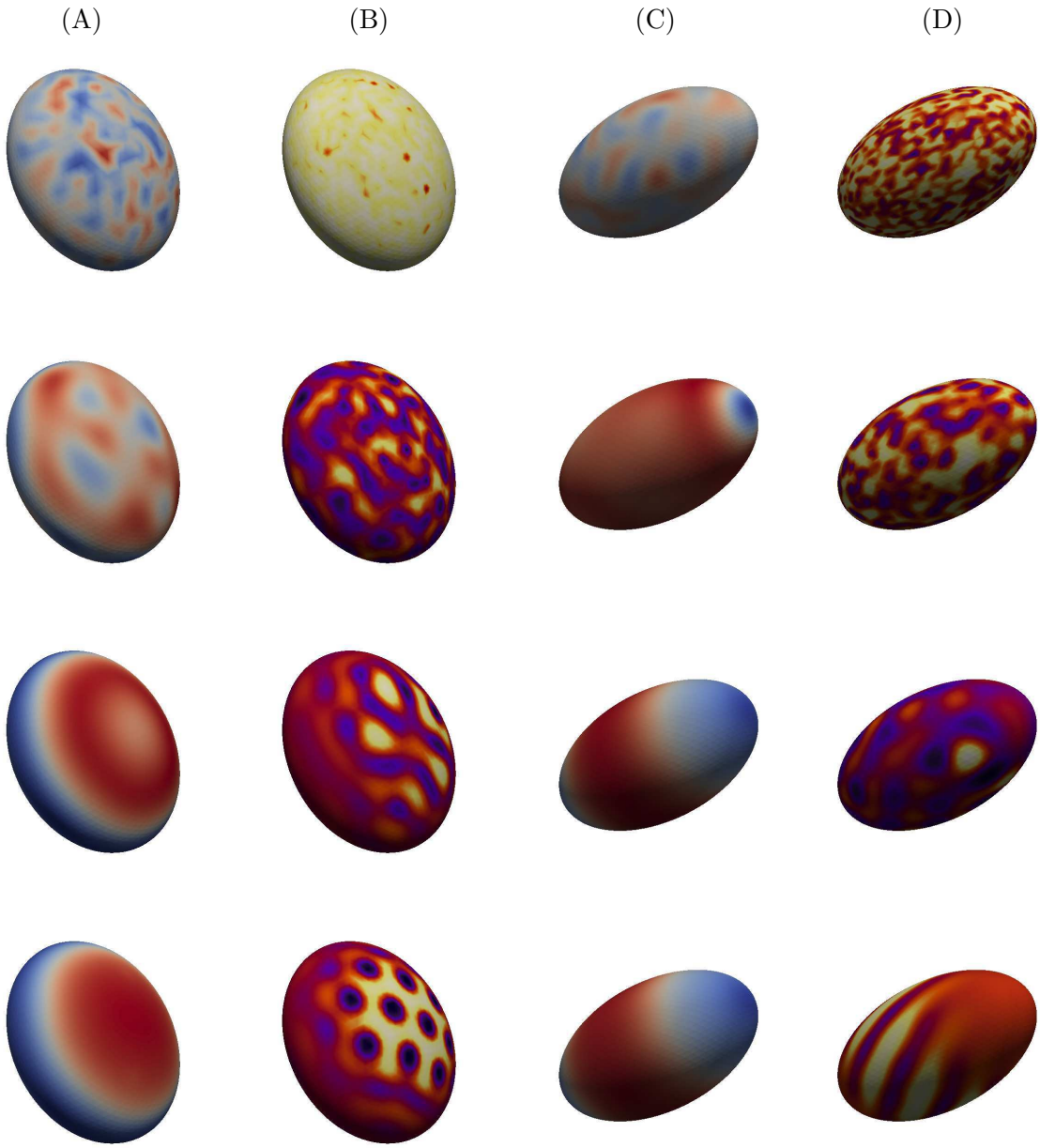

Figure 4.5: Simulations with a direct coupling between curvature and φ in the free energy. In column (A) the evolution of the driving field φ on an oblate ellipsoid is shown, along with the corresponding patterns in the Turing species - localised in the zones with least curvature - on column (B). Columns (C) and (D) display the same for the case of a prolate ellipsoid. The size of the pattern-allowing domains is limited by the free-energy coupling, which, cannot be too high in order to keep the time variation of φ small enough for numerical stability.

To understand why the direct coupling between φ and curvature arrests the coarsening, we recall that as explained in Section 3.3.2 the curvature $H(\mathbf{x})$ may be viewed as an external field locally promoting high values of $|\varphi|$ (the sign depending on the ones of c and of the curvature). If there are several places where $H(\mathbf{x})$ is high (e.g. a sphere with many bumps), then the coupling to the curvature favours the formation of a domain of φ in each of these locations. Because the overall composition of the binary mixture is conserved, and because the highly curved regions are fixed, it is not possible to join up these domains to form a single one without creating large interfaces which are thermodynamically unfavourable. The resolution of these competing factors is to arrest coarsening and end up with a multidomain steady state. This argument also suggests that, according to the value of the surface tension and the coupling strength c to the curvature, the final number of domains can be controlled (Fig. 3.14). and 4.6, patterns form in the low-curvature domains. Inverting the sign of the curvature coupling term c leads to the opposite behaviour with patterns now targeted to the high curvature regions, provided that the region with higher curvature is larger than the emerging lengthscale of the Turing patterns.

The pattern morphology (both over time and in steady state) is also determined geometrically, but in a subtler way. For instance, on an oblate ellipsoid local clusters of the activator create initially, to yield regular spot patterns at the flat sides (only the top one is shown in Fig. 4.5(A,B)). Instead, on a prolate geometry the initial dynamics is similar, but the pattern is later on relocated to a narrow central band on the ellipsoid, where it mutates to a set of tilted stripes. In this case, the selection of different patterns in steady state is simply related to the final symmetry of the domains which host them (an axially narrow symmetric band favours stripes in the perpendicular directions, two larger discs are isotropic and can accomodate spots).

In reality, the curvature of biological surfaces can vary more sharply than on the shown ellipsoids; examples are budding cells such as yeast where a functional bump develops on the cell membrane. Situations like this can lead to a more complex dynamics in our coupled Cahn-Hilliard-Turing model. An example is shown in Fig. 4.6, where a sphere with four bumps is

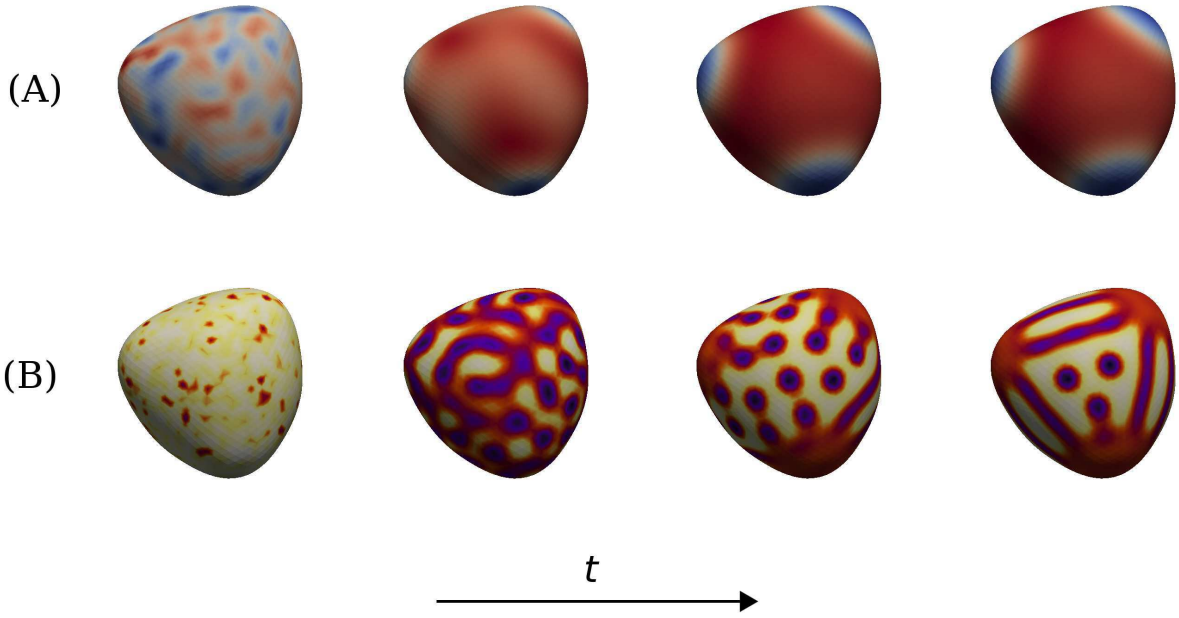

Figure 4.6: Localised pattern formation on a sphere with four bumps. Similarly to other surfaces, the coupling promotes pattern formation on regions with smaller curvature. In row (A) the time evolution of φ is shown: the positive phase spreads throughout the central region of the surface, while the negative phase is allowed to be only on the bumps (higher-curvature regions). In row (B) the corresponding patterning of the activator field u occurs in the lower-curvature regions which are rich in the $\varphi = 1$ phase. Note the coexistence of different patterns modes: striped around the bumps and spotted in the flat region.

considered. The positive curvature at the bumps recruits negative domains of φ which stop coarsening and drive away the Turing patterns. As a result, stripes form which connect the negative φ bumps; this effectively creates four disconnected domains, each of which houses a regular array of activator spots (Fig. 4.6).

4.3.3 Direct coupling with curvature

As a second possible way to localise patterning to region with a chosen curvature is a simpler version of the model where the diffusion coefficient of the Turing inhibitor depends directly on the surface curvature, and phase separation is not modelled. This can be done in practice by replacing φ with $K(\mathbf{x})$ in Eq. (4.2). The results are shown in Fig. 4.7: while the patterns

are now targeted to high or low curvature by hand, the dynamics by which they form is quite different. This is because the patterning domains are now static in space, whereas they are dynamic and linked to the Cahn-Hilliard kinetics in the coupled model. Consequently, we usually observe no switches in morphology over time, and as a result the steady states are different (compare Fig. 4.7 with Fig. 4.5 and Fig. 2B with Fig. 2C in the supplementary material). In other words, the dynamic nature of the coupling between the Turing species and φ increases the pattern forming potential of the system. . The parameters that determine the shape of D are the same used in the previous section, except for ν and φ_0, which are tuned according to the values assumed by the curvature on the considered surface. As can be seen in Fig. 4.7, the patterns are formed only in the regions where the curvature is under a threshold

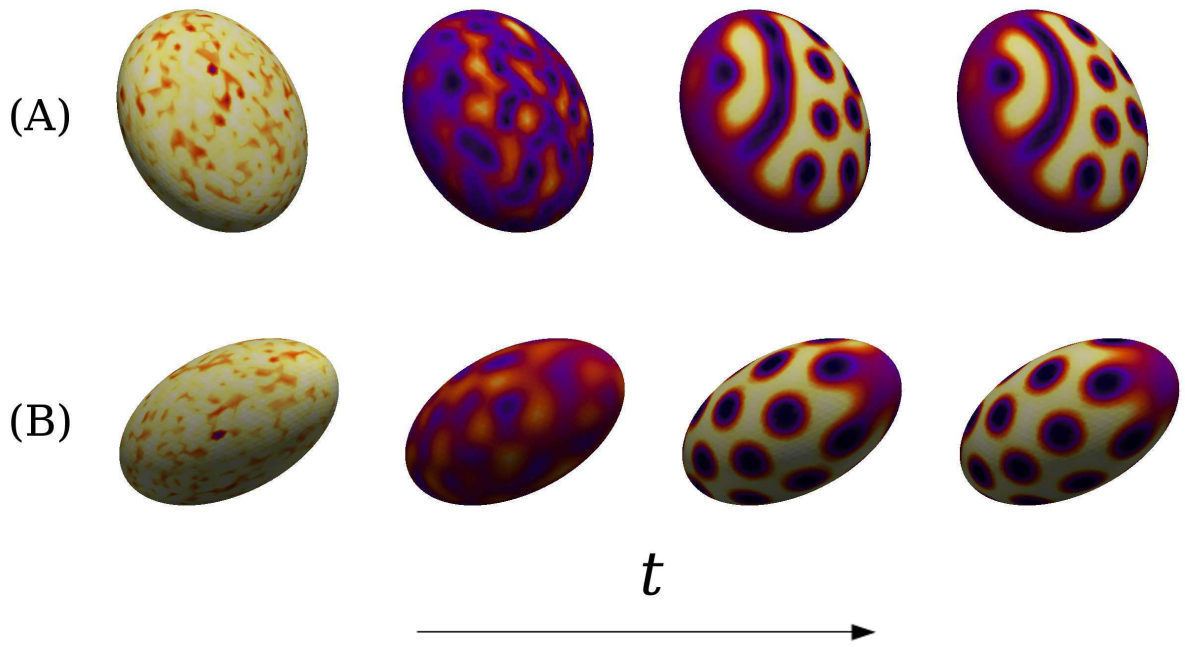

Figure 4.7: Direct coupling with curvature. Rows (A) and (B) show the time evolution on an oblate and a prolate ellipsoid respectively, of the activator field directly coupled with the gaussian curvature of the surface: the arbitrariness of the threshold curvature for patterning allows to better control the size of the pattern-allowing domains without hindering numerical stability.

value - which depends on the specific surface. The most significant differences from the case where the coupling is mediated by φ are that the modulating field is now static, since the vesicle does not change shape during the simulation, and the more precise correspondence between pattern-allowing regions and areas with lower curvature.

4.4 Lamellar patterns

In the previous section we proposed a model where the reaction diffusion system does not need to be coupled to an underlying conserved order parameter φ in order to form localised patterns. Now we describe a system in which the patterns are not the outcome of a reaction-diffusion transition but are produced from the sole configuration of the phase-separating field φ. This can be modeled by modifying the Landau free energy of the Cahn-Hilliard model with an additional term, quadratic in the laplacian of φ [56]:

$$\mathcal{F}[\varphi] = \int_{\mathcal{M}} d^2x \left[\frac{1}{4}\varphi^4(\mathbf{x}) - \frac{1}{2}\varphi^2(\mathbf{x}) + \frac{\kappa}{2} \left|\nabla\varphi(\mathbf{x})\right|^2 + \lambda \left(\nabla^2\varphi(\mathbf{x})\right)^2 \right]. \tag{4.5}$$

The term proportional to the coefficient $\lambda > 0$ stabilises the dynamics of the system also when the coefficient κ of the gradient term is negative: this possibility allows to describe systems that promote the formation of interface, as in the case of the presence of a surfactant. To model a situation in which the surfactant is attracted to regions of higher curvature, we can assume the coefficient κ to be a linear function of the local curvature $\kappa(\mathbf{x}) = -\kappa_0(H(\mathbf{x}) - H_0)$, where $\kappa_0 > 0$ is a constant coefficient, and H_0 is a threshold curvature. Among the level curves of $H(\mathbf{x})$, the ones with constant curvature H_0 house a dynamic of phase separation with no interface terms, and partitions the surface into one region where $\kappa(\mathbf{x}) > 0$ and another one with $\kappa(\mathbf{x}) < 0$.

We simulated equation (4.5) on an oblate ellipsoid, setting $\kappa_0 = 40$, since the curvature of the ellipsoid with maximum diameter $R_m = 37.8$ is of order $H \sim 10^{-2}$ (see Fig. 4.8). For $\kappa(H) > 0$, φ undergoes coarsening, with a faster evolution towards minimisation of the

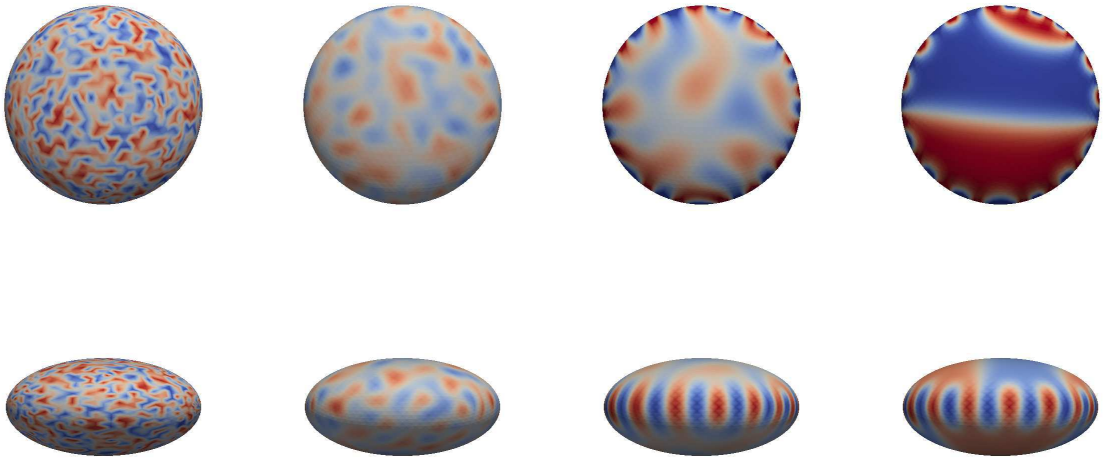

Figure 4.8: From left to right, the time evolution of a system undergoing phase separation, with the outcome of the coarsening being determined by the local curvature of the surface: on top row, Cahn-Hilliard phase separation with minimisation of interfacial length is observed when the curvature is small; on the bottom row, the areas with higher curvature promote the formation of interface, thus spatially modulated patterns are created, without the need of introducing non-equilibrium processes like the Turing reaction-diffusion system.

interfacial length where the curvature is lowest, i.e. near the center of the least-curved regions. Hence, the gradient term becomes gradually irrelevant until it falls to zero whe H_0, and thus the coarsening dynamic proceeds progressively slower as we approach H_0. On the other hand, on the most curved region of the membrane where $\kappa(H) < 0$ we observe the formation of periodic structures with highly curved interface. Consistently with that, the interface is close to minimal length geodesics where H is minimum, and more curved along the outer rim, where the negative $\kappa(H) < 0$ energetically promotes the creation of interface.

Chapter 5

Dynamic evolution of membranes

In the systems considered so far, we assumed that the fields living on the surface evolved in time on a timescale much shorter than the ones over which the shape of the surface itself changes in an appreciable way. On the other hand one can think at situations in which the characteristic times of the two dynamics are comparable. In addition, we assume that the fields are influenced by the local curvature of the surface, and in turn they may induce local deformation on the surface. A possible way to implement this effect is to assume that the local force on the surface acts along the surface normal and linearly proportional to the local value of the field φ. In addition, in order to avoid an unbounded local strain on the surface we assume that the force is proportional to the cell area σ_i surrounding the point i- the latter being necessary to avoid a higher strain on the surface in regions with higher densities of grid points. The expression we consider is

$$\mathbf{F}_\mathbf{i}^\varphi = F_0 \, \varphi_i \, \sigma_i \, \mathbf{n}_i,$$

where $\mathbf{n}_i$ is the unit normal to the surface at point i pointing in the outward direction, and the value of F_0 determines the orientation and the intensity of the force. Note that, without any other forces acting on the surface, this simple model is numerically unstable because the deformations rapidly sum up and breaks the surface apart. It is also conceptually inconsistent, because in real biological membranes there always are elastic forces restoring the initial shape

of the membrane and countering the effect of external forces. In order to design a more stable version, we need to take into account intrinsic mechanical properties and conservation laws of the membrane.

In this chapter we build a model for the evolution of closed vesicles undergoing phase separation. The model is similar to other works in literature [57, 58, 59, 60], with some fundamental differences. On one hand, it does not focus on the budding dynamics of multi-component vesicles as others do [58, 59, 60], but on another somewhat opposite behaviour; on the other hand, it leaves more configurational freedom to the membrane, so that the compressibility of its volume and area can be tuned in a wide range of values, leading to a variety of different equilibrium shapes that show similarities with models reproducing the shrinking the vesicle [61], and also to already known numerical results for phase-separating vesicles in the stiff limit of total conservation of area and volume [57]. Besides, the model presented here does not assume one free energy describing both the dynamics of the phase field and the membrane, treating membrane deformations as a non-equilibrium process.

5.1 Mechanical properties of biological membranes

Biological membranes are selectively permeable barriers that typically separate two predominantly aqueous compartments. Among their functions there are the compartmentalization of the structures in the cell, the formation of a stable fluid medium for catalytic reactions, and assistance in transmitting inter- and intracellular signals and in keeping the cells attached to their substrate [62]. A typical example of biological membrane is the phospholipidic bilayer of cell membrane: the membrane that surrounds the cytoplasm of living cells is composed by amphiphilic phospholipids that have a hydrophilic phosphate head and a hydrophobic tail consisting of two fatty acid nonpolar chains (Fig. 5.1A). The superposition of two sheets of parallel phospholipids, with the nonpolar tails oriented towards the contact plane between the two sheets, constitutes the bilayer, as displayed in Figure 5.1B. The bilayer is characterised by the presence of different lipid phases depending on the temperature of the system and the chemical

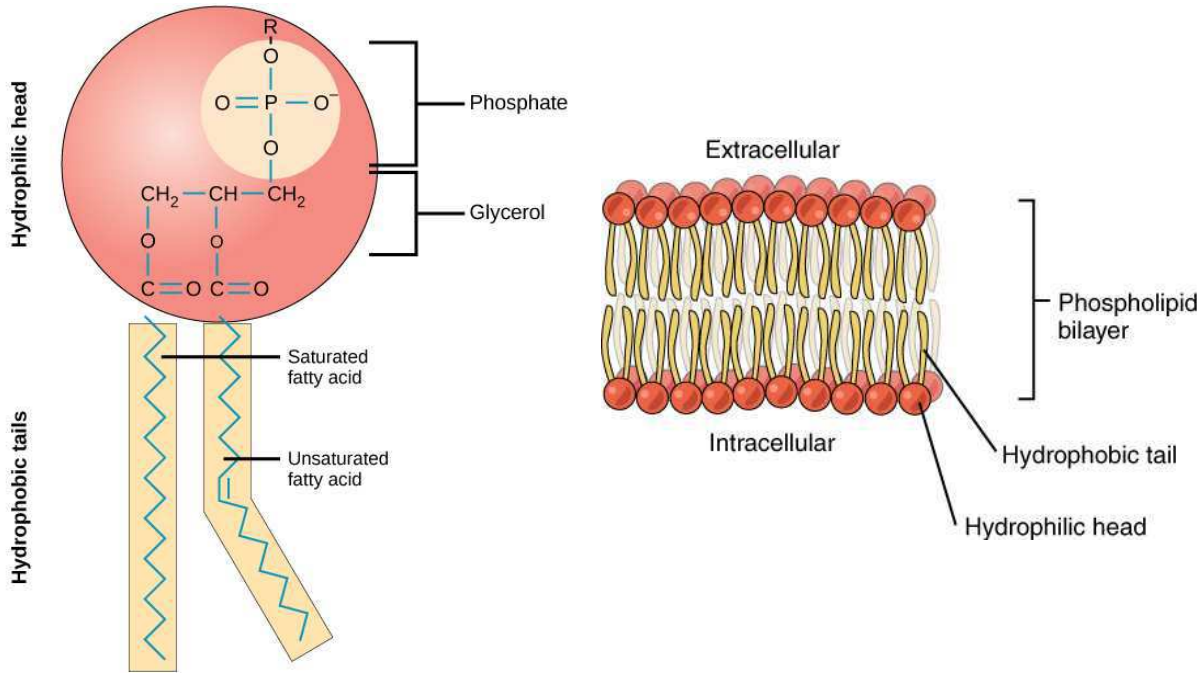

(A) (B)

Figure 5.1: Figure A shows the structure of a phospholipid: molecules of this class are made up by two fatty acid hydrophobic chains and a polar head constituted by a modified phosphate group attached to a glycerol backbone. In figure be we show a phospholipid bilayer consisting of two adjacent sheets of phospholipids arranged tail to tail. The hydrophobic tails associate with one another, forming the interior of the membrane. The polar heads contact the fluid inside and outside the cell (image taken from [63]).

properties of the tails of the phospholipidic molecules; the different phases are characterised by different packing of the lipids within the bilayer, affecting its mechanical properties [64, 65].

Following the well-established fluid mosaic model that describes the cell membrane as a two-dimensional fluid [2], the bilayer can be treated as a continuous two-dimensional medium, and consistently characterised by its response to the displacement of some mass from its equilibrium position. Since we are considering negligible the thickness of the membrane, we here limit our description to displacements that produce stretching (i.e. a change in surface area) and bending (the change in curvature) of the membrane.

The stretching consists in a deformation that varies the area of the membrane, producing

a change in the surface tension. The increase in tension reflects the increase in the free energy, which can be evaluated through the Hooke's law for continuous media. If we assume an isotropic deformation, the free energy variation is quadratic in the area variation, so it can be described by the expression

$$\Delta E_A = \frac{\kappa_A}{2} (\Delta A)^2 .$$

The stretch modulus is defined as $K_A = \kappa_A \cdot A_0$, where A_0 is the equilibrium area, and its typical values are around $K_A \approx 60 k_B T / nm^2$ [66, 67].

Bending is the main deformation responsible for change in membrane shape: the sole contribution of bending energy can reproduce a range of membrane shapes corresponding to the ones observed in living matter [68, 69, 1]. The relevant quantity when defining the bending energy of a membrane is not an area as in the case of stretching, but the curvature of the membrane. By recalling from chapter 2 that the mean curvature gives an estimate of the displacement along the normal direction of a curve on the membrane, we assume this is the relevant quantity in evaluating the bending energy, since bending implies the displacement of points of the membrane perpendicularly to the membrane itself. The higher the displacement, the higher the curvature, so following the idea initially proposed by Helfrich [1] we can write the total curvature-elastic energy as the hamiltonian

$$E^B(t) = \sum_{i=1}^{N} \frac{\kappa_B}{2} \left(H_i(t) - H_i^0 \right)^2 + \sum_{i=1}^{N} \kappa_C K_i(t), \tag{5.1}$$

where H_i denotes the mean curvature at point i and H_0 is the spontaneous local curvature of the membrane, K_i the gaussian curvature, and κ_B, κ_G are the bending moduli, whose typical values range from about $10 k_B T$ to $100 k_B T$ [70]. As in the case of stretching, the energy is quadratical in the deformation, which is represented as the deviation from a spontaneous curvature which reflect the asymmetry between the inner and outer monolayer of the membrane.

5.1.1 Mesh elasticity

A simple way to impose an elasticity to the icosahedral grid representing the surface is done by representing the edges as elastic springs. The unstressed length of each edge $\mathbf{e}_{ij}$ is assumed to be the length L^0_{ij} in the initial spherical configuration, so that the elastic force acting on vertex i of the grid at time t will be

$$\mathbf{F}^E_i(t) = \sum_{j\in\langle i\rangle} H_E \mathbf{e}_{ij}(t) \frac{L^0_{ij} - L_{ij}(t)}{L_{ij}(t)}, \tag{5.2}$$

where $L_{ij}(t)$ is the length of edge $\mathbf{e}_{ij}(t)$ and H_E is the elastic constant of the spring. While this is sufficient for a surface with an even distribution of vertices, we recall from chapter 3.1 that on an icosahedral grid triangulation, as the one we chose, there are 12 points with 5 nearest neighbours instead of 6 as any other point of the grid. If we apply the force (5.2) to all points of the grid, we find that the 12 singular points are less tightly attracted towards their neighbours, therefore they are more subject to normal forces evenly applied to every point of the surface. To fix this inhomogeneity in the response of the surface to an external force, we assign to the springs connected to a singular point $i^\star$ a different elastic constant $H^\star_E = \frac{6}{5}H_E$, so that the total force pulling on point $i^\star$ equals the total force pulling on points with 6 neighbours.

5.1.2 Bending rigidity

The elastic force we just implemented is sufficient to limit excessive deformation which could cause a real membrane to break, and more generally, to lead to instability when simulating its evolution. However, this is not enough: indeed, there are still deformations that can distort the angles between the faces (see Fig. 5.2), despite preserving the lengths of the edges , bringing up pointy protrusions through which the discrete nature of the surface, which is necessary for computational purposes, would induce artificial dynamics which do not reflect any real situation.

To overcome this pathological, non physical effect, we impose a spontaneous curvature on

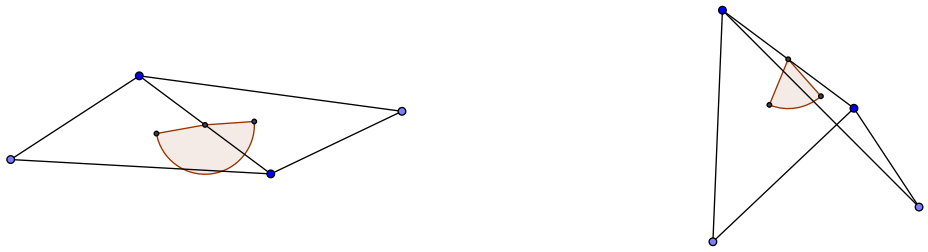

(A) (B)

Figure 5.2: Bending of a pair of triangle elements around the shared edge. The edge lengths do not vary from Fig. A to Fig. B, but in the latter, the angle between the facets (shaded) is reduced, bringing up a pronounced deformation that might interfere with the numerical accuracy of the simulation.

the membrane, so that the formation of regions with too high a curvature are energetically unfavoured. We use for this purpose the Helfrich potential (5.1) as a starting point. The Gauss-Bonnet theorem states that on a surface homeomorphic to a sphere, the integral of the gaussian curvature is always equal to 4π (see 2 in appendix A); since in our model the topological genus of the surface does not change from the one of the sphere, we can neglect the last sum in expression (5.1), which would only add a constant term to the free energy integral. Keeping only the contribution of the mean curvature leads to the following potential for the bending energy:

$$E_i^B(t) = \frac{\kappa_B}{2}\left(H_i(t) - H_i^0\right)^2 . \tag{5.3}$$

The bending rigidity coefficient κ_B is proportional to the angular restoring force, $H_i(t)$ is the mean curvature at point i computed at time t, and H_i^0 is the spontaneous curvature of the membrane that descends from the asymmetry between the inner and outer layer of the membrane.

In order to derive a force acting on the points, we need to compute the spatial gradient of this potential energy. Since we are interested on the effect of the *deformations* of the surface on the curvature energy, we need to compute the usual three-dimensional gradient at each point of the grid, with a central finite difference algorithm for each of the components x_α, $\alpha = 1, 2, 3$. If $\mathbf{X^t}$ is the $3N$-dimensional vector containing all the coordinates of the grid vertices in 3D space

at time t, let us call $\mathbf{X^t}^+_{i,\alpha}$ the same array of coordinates, but with a small increment Δh summed to the α-th component of the i-th vector, and $\mathbf{X^t}^-_{i,\alpha}$ the same but with the increment being subtracted. If we associate to every configuration $\mathbf{X^t}$ the corresponding N-dimensional vector $\mathbf{H}(\mathbf{X^t})$ whose components are the mean curvatures $H_i(\mathbf{X^t})$ at each grid point, the derivative of the curvature at vertex i can be evaluated as

$$\frac{\Delta H_i(t)}{\Delta x_{i,\alpha}} = \frac{H_i(\mathbf{X^t}^+_{i,\alpha}) - H_i(\mathbf{X^t}^-_{i,\alpha})}{2\Delta h}. \tag{5.4}$$

With this definition of the spatial gradient, we can now express the bending force related to (5.3) as

$$\mathbf{F}^B_i(t) = \kappa_B(H^0_i - H_i(t))\frac{\Delta H_i(t)}{\Delta \mathbf{x}_i}.$$

5.1.3 Conservation Laws

In order for our model to be more realistic, we need our closed vesicle to limit the variations of volume and area during it evolution. We include these constraints by inserting two more harmonic terms in the total energy. If V_0 is the initial volume enclosed by the vesicle and S_0 is its initial surface area, we define the two additional energy terms

$$E^V + E^S = \frac{\kappa_V}{2}(V(t) - V_0)^2 + \frac{\kappa_S}{2}(S(t) - S_0)^2,$$

with $V(t)$ and $S(t)$ being, respectively, the volume and the area of the vesicle at time t. We made this choice instead of using Lagrange multipliers because it is simpler to implement numerically, and allows to tune compressibility of the surface and volume. In this framework, it is quite clear that, by choosing sufficiently high values of κ_V and κ_S, one can constrain the system to stay closer to the initial values V_0 and S_0: in fact, in the limit $\kappa_V \to \infty$, $\kappa_S \to \infty$ the effect of this energy term is equivalent to applying a Lagrange multiplier. In the notation of section 5.1.2, we can then obtain the restoring force related to these new energy terms, by

first computing the discrete gradients

$$\frac{\Delta V(t)}{\Delta x_{i,\alpha}} = \frac{V(\mathbf{X^t}^+_{i,\alpha}) - V(\mathbf{X^t}^-_{i,\alpha})}{2\Delta h}, \qquad \frac{\Delta S(t)}{\Delta x_{i,\alpha}} = \frac{S(\mathbf{X^t}^+_{i,\alpha}) - S(\mathbf{X^t}^-_{i,\alpha})}{2\Delta h}, \tag{5.5}$$

and then using them to differentiate the energy. This gives the final expression for the restoring force

$$\mathbf{F}^C_i(t) = \kappa_V(V_0 - V(t))\frac{\Delta V(t)}{\Delta \mathbf{x}_i} + \kappa_S(S_0 - S(t))\frac{\Delta S(t)}{\Delta \mathbf{x}_i}.$$

This total force effectively takes into account the local surface tension of the surface as well as the pressure of the fluid it contains.

5.2 Numerical Methods

In chapter 3.1 we deliberately used finite difference algorithms to test their stability and reliability for further extension that takes into account the dynamics of vector fields. On the other hand, in the past three years there have been developments of new methods to approach the differential geometry of vector fields on surfaces [71, 72, 73, 74]. This led us to abandon the finite difference approach used for the problem studied in Chapter 3 and moved to algorithms that allow the computation of differential operators on curved surfaces without needing to explicitly evaluate every single tensor and connection. This greatly reduce numerical errors through a smart use of local transformations of coordinates. In the following we illustrate these new methods that we have adapted to our purposes.

5.2.1 Local surface and Volume

Since our surface is discretised by a finite number of triangles, we can compute the total surface area by just summing up the areas of all the triangles. This gives the exact area of the triangulated surface, which obviously differs the less from the continuous version the higher is the number of grid points used to discretise the surface. This is enough for the total area,

but we might be interested in computing the area locally: we present two different definitions which are useful for our applications.

The first one is the Voronoi area of vertex i defined in 5.2.3: with reference to Fig. 5.5C, we can see that $\alpha + \beta + \gamma = \pi/2$, thus $\alpha = \pi/2 - \hat{k}$ and $\gamma = \pi/2 - \hat{j}$. This means that the shaded area in figure 5.5 - which is the intersection between the Voronoi region of i and $T(i,j,k)$ - is given by $\frac{1}{8}(|ij|^2 \cot \hat{k} + |ik|^2 \cot \hat{j})$. Upon summation over all the triangles in the first ring around i, we obtain the formula for the Voronoi area:

$$A_i^V = \frac{1}{8} \sum_{j \in \langle i \rangle} (\cot \alpha_{ij} + \cot \beta_{ij}) \left| \mathbf{x}_i - \mathbf{x}_j \right|^2 .$$

This is the definition of the cell area that we shall use in the computation of the laplacian operator and the mean curvature.

Another useful definition of the area of the cell surrounding a point i can be obtained by dividing by a factor of 3 the sum of the areas of the triangles converging at i:

$$A_i^E = \frac{1}{3} \sum_{T(i,j,k) \in \langle i \rangle} A_T.$$

This definition derives quite easily from the request that the surface of each triangle be equally subdivided between its three vertices, even though no specific boundaries of this subdivision are assumed. Nonetheless, this simple definition displays the relevant property that the sum of tha areas of the cells of all the points of the grid coincides with the exact area of the discrete surface, whereas the Voronoi areas might superimpose if during the dynamics some of the triangular facets become obtuse.

For what concerns the volume, we again consider the surface triangles: if A_T is the area of triangle $T(i,j,k)$, the related volume is given by the triple product of the oriented triple of

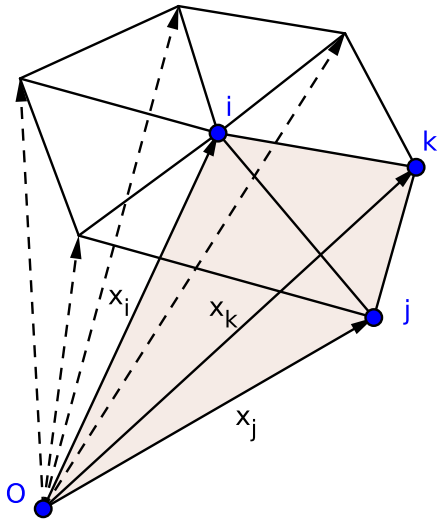

Figure 5.3: Computation of the volume element associated to vertex i: for each triangle $T(i,j,k)$ having i as its vertex, the volume of the simplex generated by vectors $\mathbf{x}_i$, $\mathbf{x}_j$, $\mathbf{x}_k$ (shaded in the figure) is divided by three in order to equally subdivide it among the three vertices of triangle $T(i,j,k)$.

position vectors of its vertices (see Fig. 5.3), up to a scale factor:

$$V_i = \frac{1}{18} \sum_{T(i,j,k) \in \langle i \rangle} \mathbf{x}_i \cdot (\mathbf{x}_j \wedge \mathbf{x}_k).$$

The prefactor is obtained by multiplying the factor 1/6 needed to obtain the volume of a simplex from a triple product, and the factor 1/3 to equally subdivide the volume of the "slice" among the vertices of the triangle, following a rule analogous to the one used in the definition of the A_i^E cell area given above. We purposely used the signed version of the volume because, depending on orientation of the triangle, we can end up in computing the volume of a convex region of well a concavity of the surface - in this latter case, we assume the volume of the simplices has a negative sign, consistently with the orientation of the surface: upon summation

over all of the triangles, we obtain the volume enclosed by the surface.

5.2.2 Local derivatives

As we have seen in section 5.1, there are different forces working together to keep the membrane at equilibrium, each one of them depending on the effects on potential energy of the membrane of small displacements of surface points. The spatial differentiation we use involves recalculating the quantities of interest for highly numerous sets of points, which is quite expensive from a computational point of view; however, if we look at the discrete derivatives in sections 5.1.2 and 5.1.3, we can substitute computation of derivatives of global quantities, such as total volume and area, with local ones.

By considering the expression 5.10 for the discrete approximation of the mean curvature, we can see that its application to a single point i involves only local quantities of the triangular mesh, and only a summation on the small number of first neighbours of vertex i. Thus, we can neglect all the terms in vectors $\mathbf{X}^{\mathbf{t}\pm}_{i,\alpha}$ with the exception of the incremented vector $\mathbf{x}_i$ and its nearest neighbours - the coordinates of the latter remaining unvaried from $\mathbf{X}^{\mathbf{t}}$.

Similar considerations can be made for the surface and area variations in expressions 5.5: the displacement of a single point can influence only the partial volume and surface assigned to vertex i and its nearest neighbours.

5.2.3 Finite element laplacian operator

To compute the Laplace-Beltrami operator of a scalar function on a triangulated surface, we need first to find a discrete version of its gradient, and then compute the divergence of the gradient with a simple application of the Stokes theorem [75].

Let f be a scalar function on a triangulated surface, with values on the vertices $i \in \{1, ..., N\}$. For each triangle $T(i, j, k)$, where i, j and k are the indices of its vertices in counterclock order as in Fig. 5.4, we can identify a point $\mathbf{u} \in T(i, j, k)$ with the local barycentric coordinates

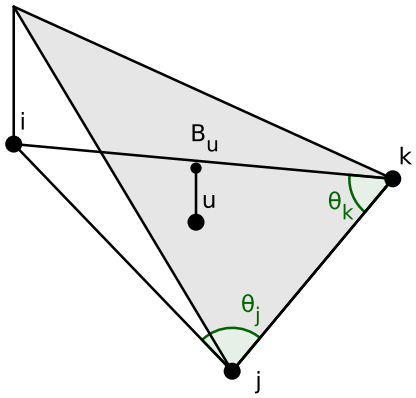

Figure 5.4: A triangle $T(i,j,k)$ is shown, with the shaded surface representing the graph of the barycentric coordinate $B_i(\mathbf{u})$ for each $\mathbf{u}$ within the triangle. The function B_i reaches its maximum value 1 at vertex i, and goes linearly to zero as it meets the opposite edge $\mathbf{e}_{jk}$. The variation of B_i is steepest in the direction orthogonal to edge $\mathbf{e}_{ij}$, therefore this is the direction of the constant gradient vector ∇B_i on triangle $T(i,j,k)$.

$B_i(\mathbf{u}), B_j(\mathbf{u}), B_k(\mathbf{u})$, defined as the coefficients in the linear combination

$$\mathbf{u} = B_i(\mathbf{u})\mathbf{x}_i + B_j(\mathbf{u})\mathbf{x}_j + B_k(\mathbf{u})\mathbf{x}_k,$$

with the properties that $0 \leq B_i, B_j, B_k \leq 1$, and $B_i + B_j + B_k = 1$. These coordinates provide a local basis for linear interpolation of function f on triangle $T(i,j,k)$, so we can write

$$f(\mathbf{u}) = B_i(\mathbf{u})f_i + B_j(\mathbf{u})f_j + B_k(\mathbf{u})f_k.$$

The gradient of the function is now easily evaluated as the linear combination of the gradients of the barycenters coordinate functions: since these are linear, the gradients will be constant. The direction of the gradient vectors is determined considering that B_i is 1 on point i, and linearly goes to 0 as we move orthogonally towards the edge opposite to i (see Fig. 5.4): this is the direction of steepest variation of the coordinate function, so the gradient can be written as the constant vector

$$\nabla B_i(\mathbf{u}) \equiv \frac{(\mathbf{x}_k - \mathbf{x}_j)^\perp}{2A_T},$$

with A_T being the area of the triangle and $(\mathbf{x}_k - \mathbf{x}_j)^\perp$ the vector orthogonal to $\mathbf{x}_k - \mathbf{x}_j$ with its same length and pointing in the direction of i. Since the coordinates must sum identically to 1, the sum of the gradients has to be zero, and we can express $\nabla B_i = -\nabla B_j - \nabla B_k$. This leads us to the explicit formula for the gradient of f:

$$\nabla f(\mathbf{u}) = (f_j - f_i)\,\frac{(\mathbf{x}_i - \mathbf{x}_k)^\perp}{2A_T} + (f_k - f_i)\,\frac{(\mathbf{x}_j - \mathbf{x}_i)^\perp}{2A_T}. \tag{5.6}$$

This expression allows us to compute the action of the Laplace-Beltrami operator on f as the divergence of the gradient. The key step is to average the operator on the Voronoi cell of area A_i^V around vertex i, so that the laplacian takes the form

$$\left\langle \nabla^2 f \right\rangle_i = \int_{A_i} \nabla^2 f(\mathbf{u}) dA = \int_{\partial A_i} \nabla f(\mathbf{u}) \cdot \mathbf{n}(\mathbf{u}) ds. \tag{5.7}$$

The Voronoi cell is found by drawing across each edge connected to point i a segment intersecting the edge orthogonally at the midpoint; the closed path defined by the union of these segments is the perimeter of the cell (Fig. 5.5A). On each individual triangle the gradient ∇f is constant, and, as we can see from Fig. 5.5B, the integral along the piecewise linear curve from the midpoints of segments $\overline{ij}$ and $\overline{ik}$ is equal to the integral computed along the straight line connecting the two midpoints (circuitation of a constant field is zero). This means that we can write the normal vector as $(\mathbf{A} - \mathbf{B})^\perp = (\mathbf{x}_j - \mathbf{x}_k)^\perp/2$. If we put this together with formula (5.6), we obtain the integral per triangle

$$\begin{aligned} \int_{\partial A_i \cap T(i,j,k)} \nabla f(\mathbf{u}) \cdot \mathbf{n}(\mathbf{u}) ds &= (f_j - f_i)\frac{(\mathbf{x}_i - \mathbf{x}_k)^\perp \cdot (\mathbf{x}_j - \mathbf{x}_k)^\perp}{4A_T} \\ &+ (f_k - f_i)\frac{(\mathbf{x}_j - \mathbf{x}_i)^\perp \cdot (\mathbf{x}_j - \mathbf{x}_k)^\perp}{4A_T} \end{aligned} \tag{5.8}$$

Denoting by θ_j, θ_k the internal angles of the triangle at vertices j and k respectively (see Fig.

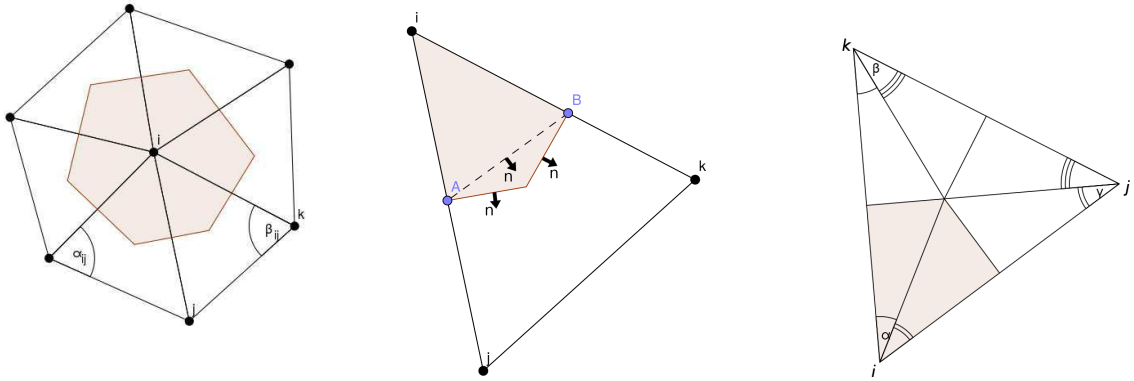

(A) (B) (C)

Figure 5.5: Geometric construction of the Voronoi region: in (A) it is the shaded region surrounding point i, with the sides connecting the circumcenters of the triangles normal to the edges of the triangles; in (B) we show the three directions the normal vector can take along two curves connecting midpoint vectors $\mathbf{A}$ and $\mathbf{B}$; in (C) we display the three angles defined connecting the circumcenter of the triangle with its vertices.

5.4), we can follow the method of section 5.2.1, computing the area of the triangle as

$$A_T = \frac{1}{2}\sin(\theta_j)\,|\mathbf{x}_j - \mathbf{x}_i|\,|\mathbf{x}_j - \mathbf{x}_k| = \frac{1}{2}\sin(\theta_k)\,|\mathbf{x}_i - \mathbf{x}_k|\,|\mathbf{x}_j - \mathbf{x}_k|\,.$$

Since the scalar products in the right hand side of eq. (5.8) are equal to $\cos(\theta_j)\,|\mathbf{x}_j - \mathbf{x}_i|\,|\mathbf{x}_j - \mathbf{x}_k|$ and $\cos(\theta_k)\,|\mathbf{x}_i - \mathbf{x}_k|\,|\mathbf{x}_j - \mathbf{x}_k|$ respectively, we obtain the integral per triangle

$$\int_{\partial A_i \cap T(i,j,k)} \nabla f(\mathbf{u}) \cdot \mathbf{n}(\mathbf{u}) ds = \frac{1}{2}((f_j - f_i)\cot(\theta_k) + (f_k - f_i)\cot(\theta_j)).$$

By summing over all the triangles surrounding f and dividing by the Voronoi area one obtains the finite element laplacian

$$\left\langle \nabla^2_{LB} f \right\rangle_i = \frac{1}{2A_i^V} \sum_{j \in \langle i \rangle} (\cot\alpha_{ij} + \cot\beta_{ij})(f_j - f_i) \tag{5.9}$$

5.2.4 Mean curvature

In chapter 3.1 we derived the mean curvature as a trace of a tensor. This definition required explicit construction of the first and second fundamental form starting from the derivatives of the coordinate functions. Now that we have an easier expression for the discrete laplacian on a triangulated curved surface, we can use it to compute the mean curvature of the surface through the following formula [76]:

$$2H_i\mathbf{n}_i = -\nabla^2_{LB}\mathbf{x}_i,$$

where $\mathbf{n}_i$ is the outward unit normal at point i. As in previous section, we average the value of the operator through integration on a cell that includes i, obtaining the simple result reported by

$$\mathbf{H}_i = \frac{1}{2A_i^V}\sum_{j\in\langle i\rangle}(\cot\alpha_{ij} + \cot\beta_{ij})(\mathbf{x}_i - \mathbf{x}_j), \qquad H_i = |\mathbf{H}_i|\,, \tag{5.10}$$

where the norm $|\cdot|$ is intended as the standard euclidean norm in three dimensions.

5.2.5 Normal to the surface

The outward unit normal vector at a point i can be derived from (5.10) by normalising the vector $\mathbf{H_i}$. However, this is a definition which does not hold for areas with zero mean curvature, or more dramatically on minimal surfaces where the mean curvature vanishes everywhere. In order to avoid such artificial singularities, we choose a simpler but more stable algorithm to find normal vectors.

We start by computing the outward unit normal for a triangle $T(i,j,k)$ as the normalised external product of the edges departing from i - this is but the discrete version of equation (2.5):

$$\mathbf{n}_{ijk} = \frac{(\mathbf{x}_j - \mathbf{x}_i)\wedge(\mathbf{x}_k - \mathbf{x}_i)}{|(\mathbf{x}_j - \mathbf{x}_i)\wedge(\mathbf{x}_k - \mathbf{x}_i)|}.$$

Once we have the $\mathbf{n}_{ijk}$ for each triangle $T(i,j,k)$ sharing vertex i, we can compute the normal

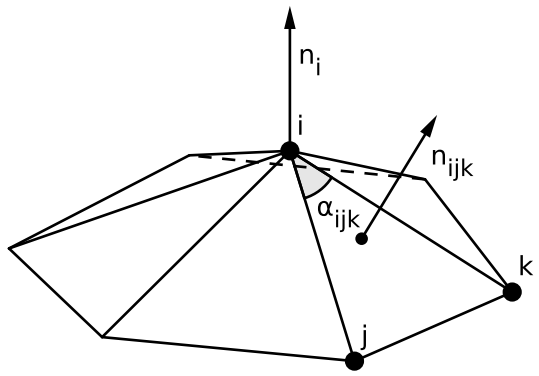

Figure 5.6: Diagram of a hexagonal cell centered at vertex i for computation of the normal vector $\mathbf{n}_i$. The construction shows as an example the normal to triangle $T(i,j,k)$ and the angle at i, α_{ijk}. The normal vector $\mathbf{n}_i$ is obtained upon weighed summation over the normals of all the triangles using the angles α_{ijk} as weights.

vector at i by taking a weighed average of the $\mathbf{n}_{ijk}$, with the angles of the triangle having i at their vertex α_{ijk} as weights (see Fig. 5.6):

$$\mathbf{n}_i = \frac{\sum_{T(i,j,k)\in\langle i\rangle} \alpha_{ijk}\mathbf{n}_{ijk}}{\left|\sum_{T(i,j,k)\in\langle i\rangle} \alpha_{ijk}\mathbf{n}_{ijk}\right|}.$$

This algorithm gives a stable, reliable estimate of the vertex normal, even in the presence of marked irregularities in the distribution of angles among the triangles of the grid.

5.2.6 Phase-dependent normal force

Until now we focused on the forces exerted by the membrane's own elasticity and bending energy and by the conservation constraints. Of course, for a meaningful evolution to take place, there has to be also an external force, as in the state of balance among the internal forces, the membrane rests unperturbed in its original spherical configuration, whatever is the value of the field φ.

As already stated at the beginning of this chapter, if we assume that the relaxation times of the membrane and the field living on it are of the same order of magnitude, the action of a force depending on the value of the field φ in a certain region of the surface becomes relevant. The

biophysical basis of this idea is that some classes of proteins, orientations of the cortical actin, or lipid phases of the membrane, induce a protrusion or an engulfing, depending on the value of the order parameter [77, 78, 79, 80], and are attracted themselves to regions of higher or lower curvature [81, 82, 83]. The direct dynamics, i.e. the action of the field on the membrane, is explicated through the imposition of a normal force, this being the easiest way to induce a locally positive curvature if the force points outward, or negative if it points inward. This choice is motivated by the assumption that the coarsening dynamic induced by the modified Cahn-Hilliard free energy is the prevailing surface phenomenon: since the force exerted by the cytoskeleton or curvature-inducing proteins has both a normal component and a tangential flow [57, 84], by neglecting the surface flow of proteins or cytoskeleton-induced flow in favour of the phase separation, we assume that only the normal component of the force is relevant in the evolution of the membrane.

We first assume that the force is proportional to the local normal vector, $\mathbf{F}_\mathbf{i}^\varphi \propto \mathbf{n}_i$. Moreover, the proportionality coefficient is a linear function of φ, namely $F_0\varphi_i$, where F_0 is a global constant that can be chosen as a positive or negative real number. The last term in the definition of the force $\mathbf{F}_i^\varphi$ follows naturally from the consideration that the grid is not perfectly uniform: this means that on a membrane with a constant φ at all its points, there will be a higher pressure in regions with higher density of points per unit area, representing an unrealistic evolution caused only by the particular discretisation chosen. In order to avoid artificial dynamics like this, we complete the definition of the force by multiplying it by the area of the surface cell surrounding point i (A_i^E in section 5.2.1), which is good for our purpose since it weighs the force per grid point by local area. The final expression for the normal force is then

$$\mathbf{F}_i^\varphi = F_0\varphi_i\mathbf{n}_i A_i^E.$$

The equation of motion for grid point i is completely specified by the total force acting on the vertex. As done in section 3.2.3, we add a damping force $-\gamma\dot{\mathbf{x}}_i$ with $\gamma = 1/\Delta t$: the

damping constant gives therefore the timescale of evolution of the shape of the vesicle, hence this evolution is assumed to proceed at a slower pace than the phase separation of field φ. Since the damping term cancels out with the velocity term at time t, we are left with just one equation for the position of each point at time $t + \Delta t$:

$$\mathbf{x}_i(t + \Delta t) = \mathbf{x}_i(t) + \Delta t \left(\mathbf{F}_i^{\varphi}(t) + \mathbf{F}_i^{E}(t) + \mathbf{F}_i^{B}(t) + \mathbf{F}_i^{C}(t) \right)$$

5.3 Results

We are now provided with two differential equations, one for the evolution of the position of grid points $\mathbf{X^t}$, and one for the evolution of the field $\varphi_i(t)$ on the surface, i.e. the Cahn-Hilliard equation with curvature coupling of 3.3.2. The full system of PDE to be solved is then

$$\begin{cases} \dot{\mathbf{x}}_i(t) &= \mathbf{F}_i^{\varphi}(t) + \mathbf{F}_i^{E}(t) + \mathbf{F}_i^{B}(t) + \mathbf{F}_i^{C}(t) \\ \dot{\varphi} &= M \nabla_{LB}^2 \left[\varphi^3 - \varphi - \kappa \nabla_{LB}^2 \varphi - cH \right]. \end{cases} \tag{5.11}$$

The constant M in the equation for φ sets a timescale for the coarsening of the field. In the previous chapters, we assumed that the timescale $\tau_D = 1/\gamma$ for vesicle deformation was negligible when compared to the scale $\tau_C = 1/M$ of the phase separation, so that in the limit $\tau_D \gg \tau_C$ the vesicle could be considered static. In this case, we assume instead $\tau_C > \tau_D$, with τ_D small, so that the evolution of the vesicle shape can be observed over a time comparable to the one needed for φ to reach steady state. The surface is expected to deform thanks to the positive feedback of the normal force and the attraction of high-curvature and domains of the A-rich phase, while the ones of the B-rich phase migrate towards regions of progressively small curvature: the deformation will follow the same coarsening dynamics that φ undergoes. This coarsening will proceed until the curvature reaches threshold for coarsening arrest through the coupling with curvature (see section 3.3.2): at that point, phase separation arrests, stabilising the surface in the most symmetrical configuration allowed by the number and size of formed

domains.

We therefore expect that the number of distinct domains of the phases grows as the curvature coupling coefficient c increases, because a higher curvature term will overcome the driving force of the interface-reducing term and block the coarsening at an earlier stage. This is indeed what we observe, for all the choices of the parameters that we tested. Moreover, we expect that in the steady state there are bubbles of one of the two phases within a connected domain of the other one, or eventually the limit case of a tesselation of the surface among domains of phase A and phase B. Since the surface has spherical topology with positive spontaneous curvature, any region connecting two A-rich, positively curved domains, should have a positive curvature. This causes the curvature to increase above the critical value allowing the presence of the A-rich phase, which can then flow in that region and reduce interfacial length. Thus, for every choice of the parameters there must be one connected domain of the A-rich phase, and only the number of connected domains of the B-rich phase will increase with c. As we will see below, our findings confirm this picture. We hereby note that while our simulations were performed for a mixture with ratio 1:1 between the phases, different choices would be possible. As the fraction of A increases, we would expect a smaller dimension of the B-rich domains at steady state, because a larger A-rich domain will produce a positive feedback with the outward normal force, thus locking the size of the B-rich domains to a smaller size; vice versa, increasing the fraction of B will produce the opposite effect, thus making the influence on the steady state configuration of the average order parameter φ_0 roughly equivalent to that of the curvature coupling c in controlling the number and size of the B-rich domains.

Simulations were performed on the refined icosahedral geodesic grid of level 4 used in the previous chapters, of radius $R = 18.9$, and with a number of vertices $N = 2562$. The time integration interval is $\Delta t = 0.01$ as well as the spatial interval for differentiation of the vector $\mathbf{X^t}$, $\Delta h = 0.01$. We set the intensity of the normal force to $F_0 = 2$, the intensity of the volume restoring force to $\kappa_V = 10$ and the bending rigidity coefficient $\kappa_B = 10$. By starting from a spherical shape and initial random distribution of φ in the interval $[-1, 1]$, we investigated the

time evolution and final configuration of the surface.

5.3.1 Stretchable surface

The intensity of the surface restoring force is chosen to be $\kappa_S = 10$ and the elastic constant of the surface to $H_E = 10$: a choice which effectively implements a stretching response of the surface, while leaving the surface area rather free to vary, as shown in Fig. 5.7. The dynamics have been investigated for various choices of the curvature coupling constant c introduced in section 3.3.2.

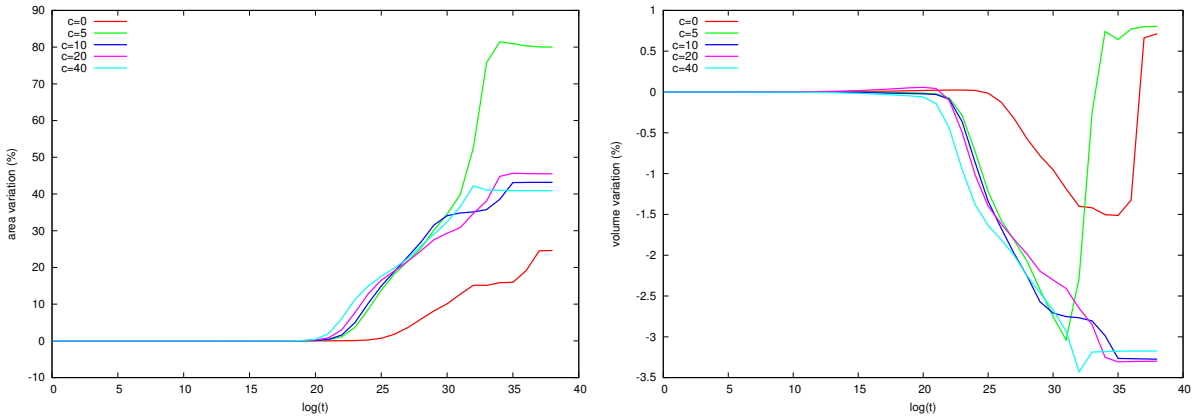

Figure 5.7: Time evolution of area (fig. A) and volume (fig. B) of an elastic vesicle with $\kappa_S = 10$, $H_E = 10$. The area is allowed to increase of up to the 80% of the initial surface, while the volume variation is confined between a +0.8% in the case of $c = 5$, and a maximum decrease -3.4% with $c = 40$.

Let us start with the case $c = 0$, so that φ follows the simple Cahn-Hilliard equation for curved surfaces of section 3.2.5. Initially, no macroscopic displacement of the points of the surface is observed, and the evolution proceeds similarly to the case of simple phase separation on a spherical surface (see 3.2.5). However, if we look at the plot of the force vectors on the surface (Fig. 5.8b), we see that in fact the force is initially displacing the points normally of a small distance. Soon after the initiation of the motion though, the restoring forces $\mathbf{F}_i^R(t) = \mathbf{F}_i^E(t) + \mathbf{F}_i^B(t) + \mathbf{F}_i^C(t)$ counter the effects of $\mathbf{F}_i^\varphi$, stabilising the vesicle shape and slowing down the deformation dynamics (figure 5.8c). The intensity of the total force then increases again,

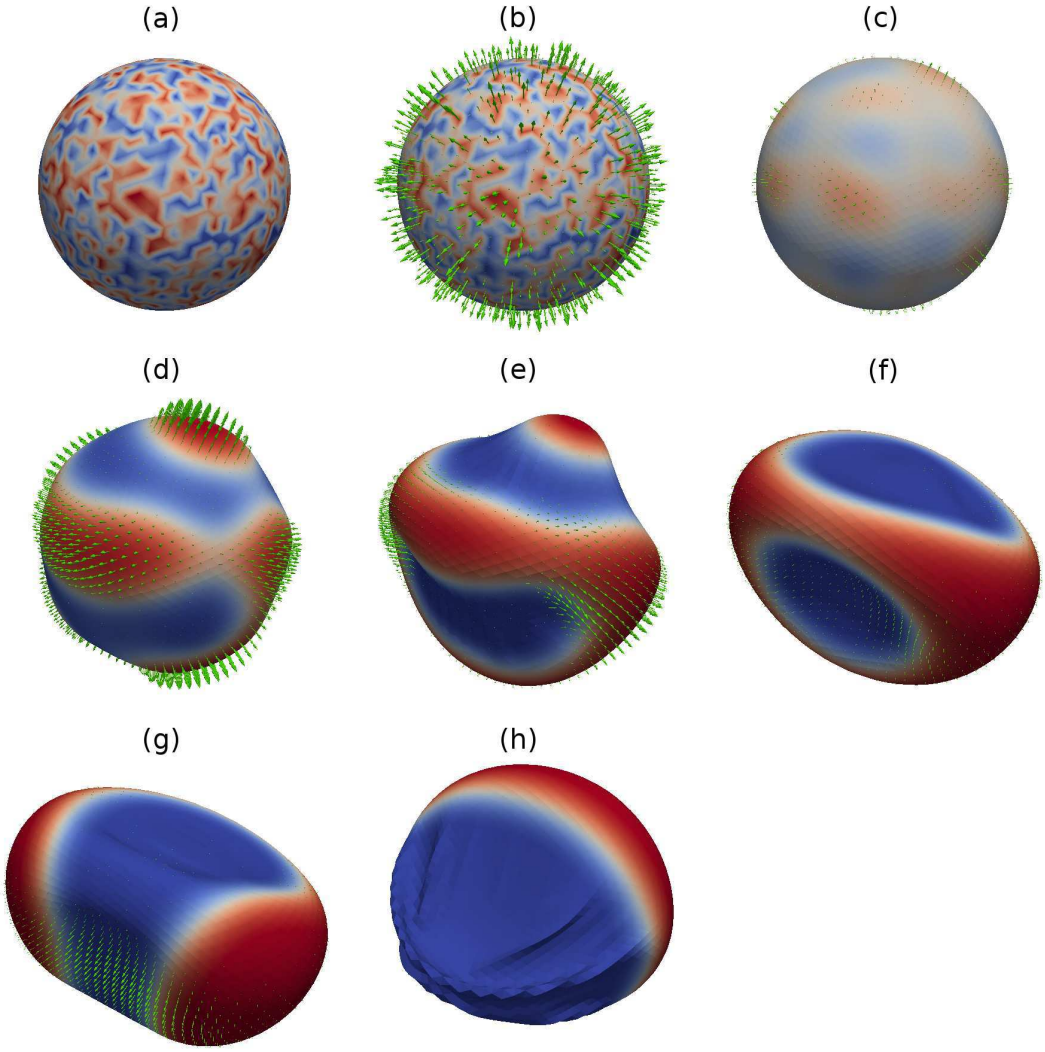

Figure 5.8: Time evolution of a vesicle undergoing phase separation on its surface while being deformed by a normal force $\mathbf{F}^{\varphi}$ proportional to the local phase of field φ. The simulation starts with a random configuration of the field φ and a spherical shape of the surface. The onset of the dynamic is characterised by initial small deformations by $\mathbf{F}^{\varphi}$; the vector force is shown in green in figure (b). The force is then countered by the spontaneous forces of the membrane, and reaches a minimum average intensity at stage (c), where no macroscopic deformation is yet visible and φ is not yet reaching the extremal values ± 1. As phase separation proceeds, the intensity of the force increases again, bringing up noticeable deformations. From (e) to (f) a large red drop in the upper part of the surface is absorbed via Ostwald ripening, bringing the system to a configuration with three domains of the B-rich phase. The connected domain with three holes of the A-rich phase is then cut in two points and becomes a single ring-like domain (g). The shape then relaxes until the interfacial length is minimised, and reaches steady state in figure (h).

as the bulk of the phase domains reach their equilibrium values, as shown in Fig. 5.8d; then $\mathbf{F}^{\varphi}$ follows the local variations of φ before being balanced by the mechanical properties of the membrane (Fig. 5.8e-g), until the phase separation is completed (Fig. 5.8h). Note that the restoring forces $\mathbf{F}_i^R$ acting on the membrane do not favour the formation of a single large domain with negative curvature. Hence, wrinkles are formed in order to contain the positively curved area confined to narrow tubular domains and surrounded by depressions or saddle-like regions characterised by a higher magnitude of the modulus of the negative principal curvature. These narrow domains have positive curvature, and we expect that, when the coupling constant c is increased to a positive value, they will attract the A-rich phase, hindering complete phase separation.

We now consider a positive coupling coefficient $c = 5$. The initial stages of the dynamic are very similar to the $c = 0$ case (cfr. Fig. 5.9a-c and Fig. 5.9a-d), but then the positive feedback between curvature and normal force sets in. The force thus becomes more intense when the coarsening proceeds, and more pronounced deformations occur (Fig. 5.9d). As already noted, with reference to Fig. 5.8g-h, we see that, when the phase separation has led to a configuration with only few domains, the area of B-rich phase must contain a region with positive curvature, namely along the ridge of the wrinkles that are formed in that region. In the case of nonzero c this configuration is prohibited, and the A-rich phase must be at the region of higher curvature. This brings a final shape where two B-rich domains are separated by a ring of A-rich phase, which can be arranged only in a maximally symmetric way to reduce interfacial length, thereupon producing a biconcave shape reminiscent of the membrane of red blood cells (see Fig. 5.9f).

Increasing the coupling coefficient to $c = 10$ produces a different shape. The dynamics is similar to the one observed with $c = 5$, but since the competition between the curvature term and the surface one in equation (5.11) is now more imbalanced in favour of the curvature, the arrest of the coarsening process takes place earlier, producing a surface with tetrahedral symmetry and a total of 4 domains of the engulfed B-rich phase separated by a protruding

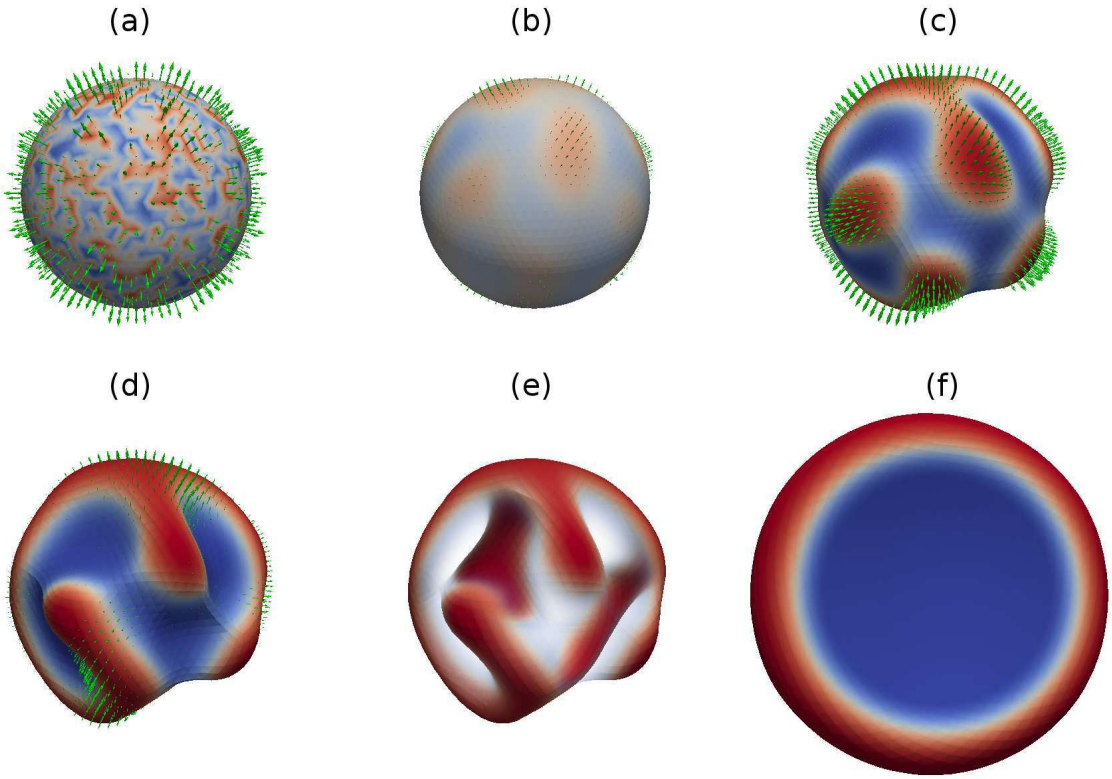

Figure 5.9: Arrested coarsening with coupling coefficient $c = 5$. The initial phases (a) to (c) are similar to those observed in the case of null coupling. Then the coupling with the curvature imposes the regions with higher curvature to be associated with the A-rich phase, as shown in figure (d). Note that in this configuration there already is a single connected domain of the A-rich phase with toroidal topology, as can be seen in figure (e): here the B-rich phase is made transparent in order to show the 3-dimensional development of the domain. The shape then relaxes in order to minimise interface, and finally reaches the biconcave shape of a red blood cell in figure (f).

connected domain of the A-rich phase, as shown in Fig. 5.10.

By increasing further to $c = 40$, the imbalance between curvature coupling and surface reduction is even more pronounced, and the number of domains of the B-rich phase in the steady state is 6, thus leading to a surface with cubic symmetry (Fig. 5.11a): the arrest of the phase separation occurs even earlier, stabilising the cubic configuration that was transient with $c = 10$ (compare with Fig. 5.10a). The number of B domains in the steady state then reaches a plateau: it reaches a configuration with 7 depressed domains for $c = 80$, which is formed

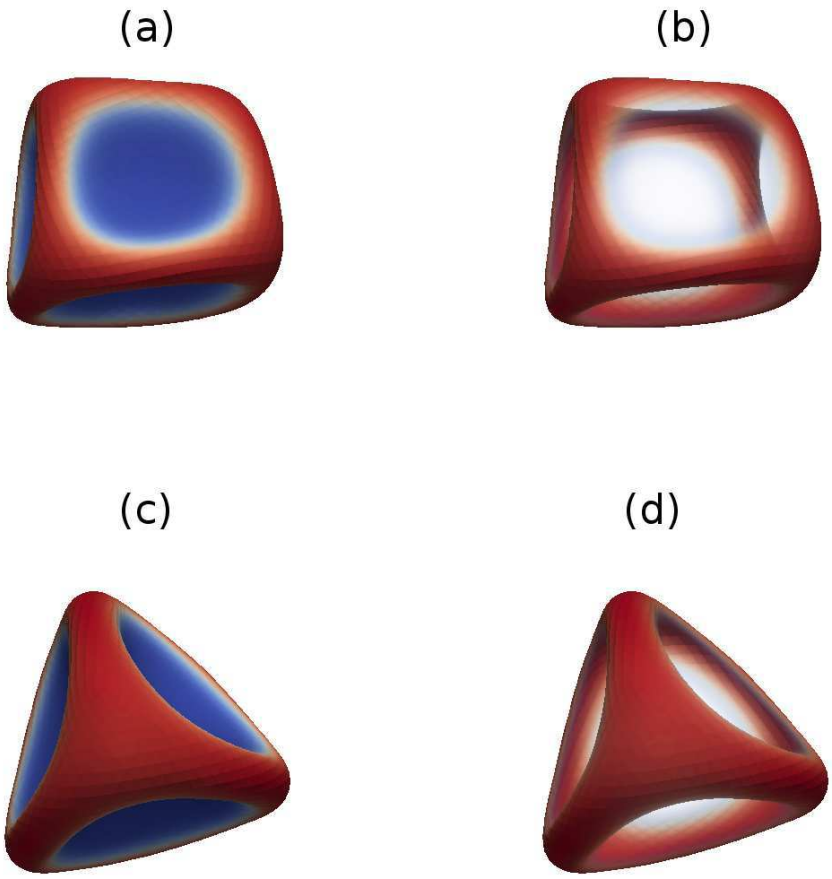

Figure 5.10: Two different stages of the evolution of the surface when the curvature coupling coefficient is $c = 10$. In figure (a) an unstable configuration with cubical symmetry is displayed, as can be better seen in figure (b) where the B-rich phase is rendered as transparent for better visualisation. The evolution then proceeds annealing one of the domains with negative curvature, and the system reaches then a tetrahedral configuration at steady state, as shown in figure (c) and in figure (d) with transparent B-rich phase.

by arresting the merging of domains in the relaxation from random to the cubic-symmetrical configuration at $c = 40$, freezing the evolution at a state in which one of the edges of the cube is replaced by a face (Fig. 5.11b).

5.3.2 Stiffer membrane

If we now increase the intensity of the elastic forces acting on the surface, setting $H_E = 100$ and $\kappa_S = 100$, we expect the surface to become less deformable, affecting the evolution and steady state configurations of the surface. In figure 5.12 the plots of the time evolution of the area and

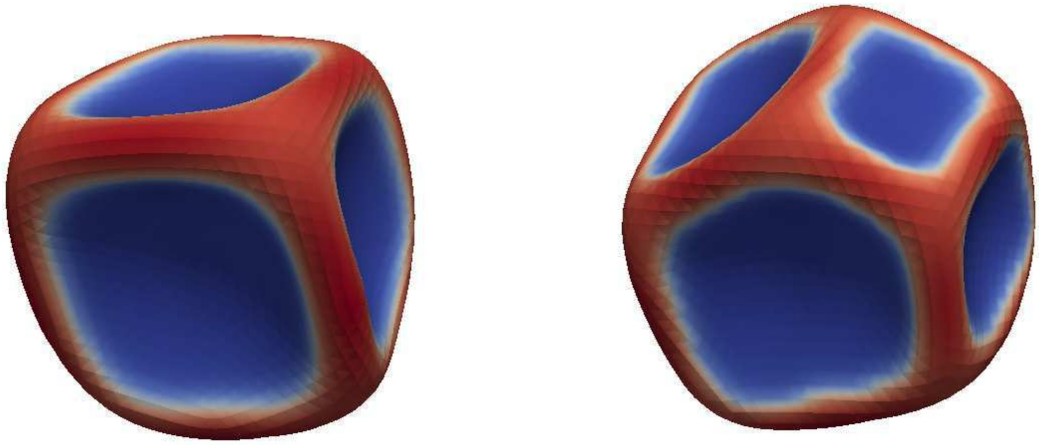

(a) (b)

Figure 5.11: Figure (a) shows the steady state configuration for $c = 40$. The coarsening is arrested with a simmetric cubic disposition of the B-rich phase domains, which was not stable for $c = 10$. Increasing to $c = 80$ (fig. (b)) causes the coarsening to arrest earlier, leaving an incomplete cubic domain with 7 blue facets.

volume of the vesicle in this second scenario are displayed, showing a smaller variation for the area, but a slight increase in volume variability. As a first consequence, we observe that the smaller stretchability of the membrane still allows the formation of the pronounced wrinkles of Fig. 5.8, but less pronounced. Apart from that, the dynamic is essentially analogous to the one described above. Let us then increase c and look for differences in the membrane shapes.

First of all, we remark that the dependence of the number of domains on the coupling coefficient c still holds, as it follows only from the mechanism presented in section 3.3.2, regardless of the mechanical properties of the membrane. However, we can see from Fig. 5.13 that the biconcave shape of Fig. 5.9 is no longer stable: while a metastable phase with two domains of the B phase separated by a ring of the A-rich phase appears during the evolution (Fig. 5.13c), the final state reaches complete phase separation. The higher elastic modulus of the membrane does not allow in fact the stretching of the surface which is necessary for the formation of a broad, negatively curved central region, while preserving the association between the phases

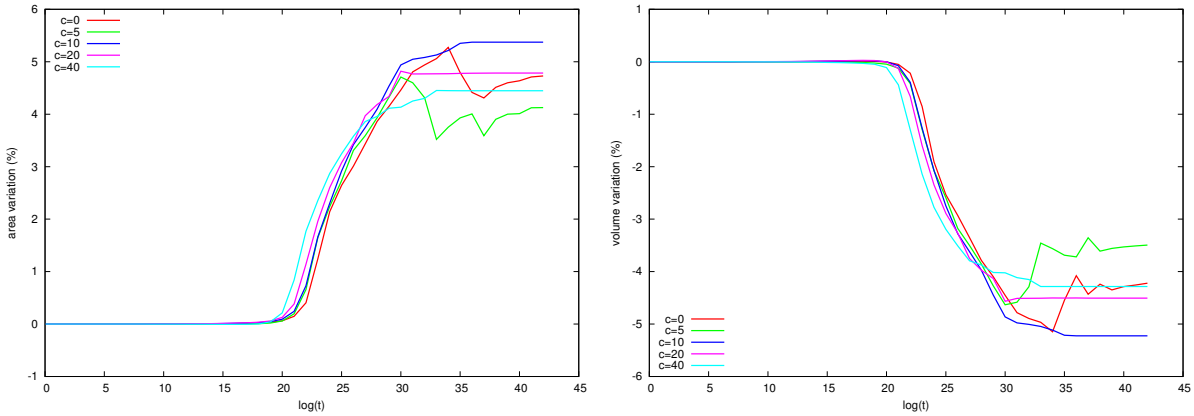

Figure 5.12: Time variation of area (A) and volume (B) of a vesicle with $\kappa_S = 100$, $H_E = 100$. The area variation is now limited of up to the 5.4% of the initial surface, but the volume variation is now accentuated to some extent, reaching its maximum at $c = 10$, with a variation of -5.2% of the initial volume enclosed by the surface.

and their preferred curvatures. Thus, the surface elasticity free energy disrupts the balance between the interfacial free energy and the curvature coupling term, unlocking the biconcave configuration and stabilising the completely separated state. The same holds for $c = 8$ and for

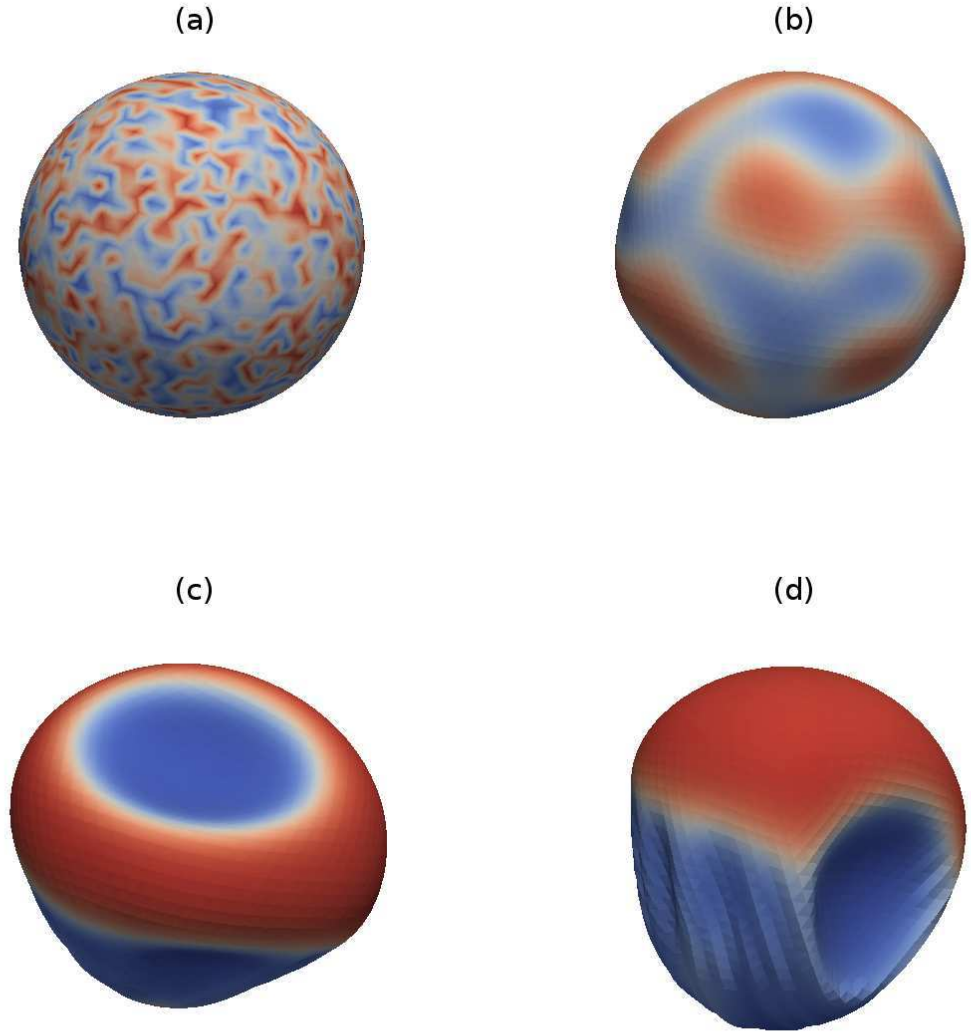

Figure 5.13: Snapshots of the time evolution of a phase-separating vesicle with the phase field φ linearly coupled to the curvature via a coefficient $c = 5$, with area compressibility and edge elasticity set to the higher values $\kappa_S = 100$, $H_E = 100$. Starting from a random configuration (a), the deformations start to appear at the same time they did in the case of lower surface elasticity (b), and then proceed to coarsening until two domains of the B-rich phase are separated by a ring of the A-rich phase (c). The outcome of the dynamics then proceeds differently from the previous case, with the two phases reaching complete phase separation while the vesicle is distorted, as happens with $c = 0$ - this last situation is portrayed in figure (d).

$c = 9$. At $c = 10$, a stable configuration with 4 B-rich domains is reached at steady state: we infer that a threshold value $\tilde{c}$ must exist between $c = 9$ and $c = 10$, which stabilises the biconcave shape.

As already said, increasing the coupling constant to $c = 10$ leads again to a tetrahedral configuration at the steady state. Increasing further c produces an increase in the number n_B of domains of the B-rich phase: in Fig. 5.14 we display the steady-state configurations of vesicles with c ranging from 20 to 80. Note that n_B grows more rapidly in this stiffer case, going from $n_B = 4$ with $c = 10$ to $n_B = 9$ when $c = 20$, and gradually reaching stationarity with $n_B = 12$

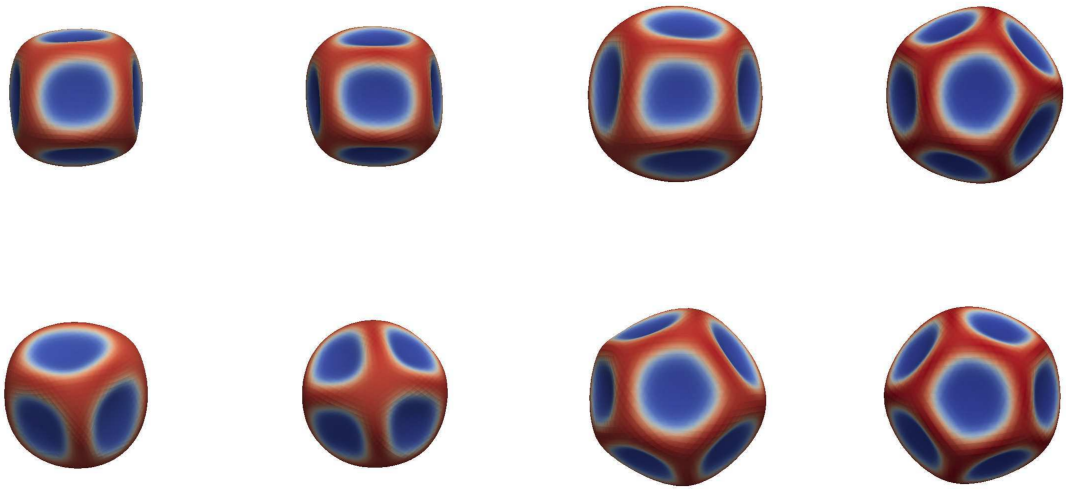

$c = 20$ $c = 25$ $c = 30$ $c = 40$

Figure 5.14: Steady state configurations of vesicles with $c \geq 20$: each column shows opposite faces of the surface, appropriately rotated for a quicker comparison, generated using the curvature coupling coefficient written at the bottom of the column. It can be easily seen that while a geometry similar to the cubic case is preserved for $20 \geq c \geq 30$, with one square face surrounded by four other faces, and the opposite side generated by the subdivision of the remaining face in the cubic configuration being subdivided into 3, 4 and 5 facets for $c = 20$, 25 and 30, respectively.

for $c = 40$. In this last case, a dodecahedral configuration is attained at large times: in order to exclude influences by the underlying dodecahedral topology of the triangular mesh, repeated

runs of the simulation with different initial random configurations have been tested, leading to randomly oriented results, confirming the independence from the connectivity of the discretised surface.

Doubling the value of c from $c = 40$ to $c = 80$ does not lead to substantial differences in the steady state; though there is a metastable state with 13 facets at a certain point in the dynamic, the final configuration is again a highly symmetrical dodecahedral but the curve $n_B(c)$ is different with respect to the case treated in section 5.3.1. The diagram of the number of B phase domains as a function of c for the two choices of κ_S and H_E presented so far is showed in Fig. 5.15.

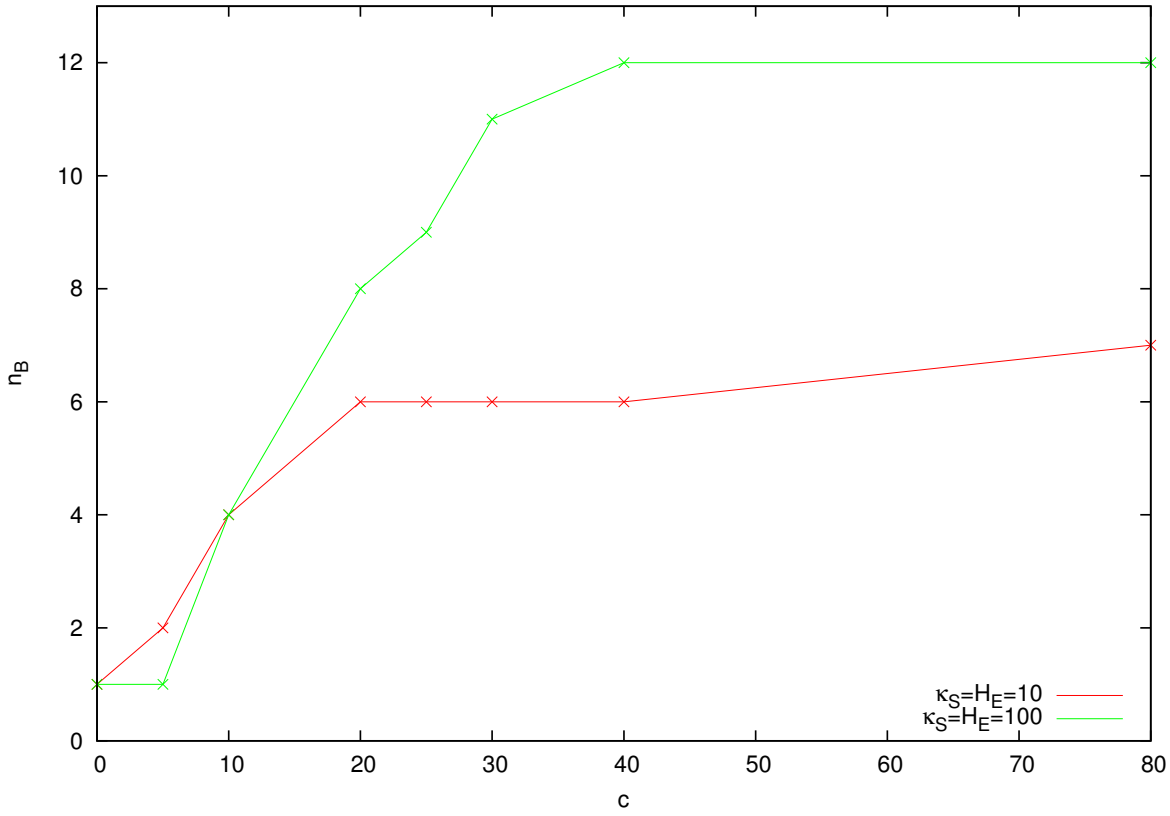

Figure 5.15: Plot of the number n_B of domains of the B-rich phase in steady state configuration versus the value of the curvature coupling coefficient c. Two different curves are produced depending on the choice of the constants κ_S and H_E. In both cases, the slope of the curve is always positive or zero, confirming the positive correlation between the c and n_B. Moreover, both the increase in $n_B(c)$ and plateau value are higher in the case of higher κ_S, H_E.

We hereby note that if we set the intensity of the volume-restoring force to a higher value, $\kappa_V = 100$, while leaving $\kappa_A = 100$, the area and volume variation are reduced considerably, approximating the effect of two Lagrange multipliers. As expected, with $c = 5$ we recover the discoidal shape obtained by Taniguchi & al. [57], confirming the consistency of our model. In this case the B-rich domains are flattened out and do not show the pronounced depressions of the previous cases. We point out that the relationship between n_B and c is confirmed, allowing to extend the results of [57] to a more general model of elastic phase separating curved surface (see Fig. 5.16).

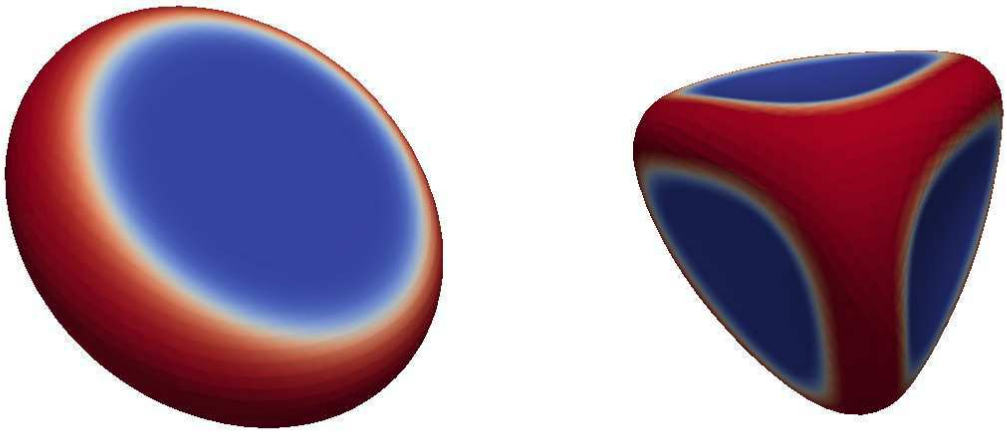

Figure 5.16: Long time configurations of a vesicle with $\kappa_V = \kappa_S = 100$, for $c = 20$ (left) and $c = 40$ (right). Increasing both κ_S and κ_V to high values leads to equilibrium shapes of the vesicles coincident with those showed in [57].

The results we have shown provide a model for the evolution of the shape of bicomponent elastic membranes, each phase of which induces a positive or negative local mean curvature. For specific ranges of the model parameters, it reproduces known configurations of vesicles, such as the biconcave shape of the red blood cell (Fig. 5.9) or the 6-fold symmetrical state characteristic of cubosomes [85] (Fig. 5.11). Though the mechanisms behind the real structures can differ from the one presented here, model structures such as GUV or GMPV with inclusions

of curvature-inducing proteins or minimal actin cortices (MAC) [86, 87, 88, 89] could be used to validate the model presented in this chapter from an experimental point of view. Different choices of the membrane constituent may be used to tune the membrane elasticity, while concentration and type of membrane proteins and the composition of the actin cortex could provide a way to tune the curvature coupling and the intensity of the normal force.

Chapter 6

Dynamics of vector fields on curved membranes

An interesting feature that can be exploited to describe biological systems is the emergence of orientational order on fluctuating surfaces. Structures presenting orientational order constrained to surfaces have been known and studied for decades [90, 91, 92]. In the case of biological systems, lipid bilayers with inclusions can have a nematic order [19]; in the cytoskeleton, during mitosis, the cortical actomyosin filaments show an orientational order typical of nematic fluids as well [20]. In vitro experiments on cytoskeletal filaments and molecular motors on flat surfaces have revealed topological defects that spontaneously self-organise, arranging in a variety of geometrical patterns [21]. Such dynamics spontaneously arise in similar media within living cells, and influence their shape and evolution. A meaningful example is the behaviour of the actin network with crosslinking proteins of various length and stiffness [93].

Probably a paradigmatic model that best captures the onset of orientational order is a liquid crystal system. The nematic phase is one of the known mesophases taken by liquid crystals, in which orientational order is present among the constituent particles of the system. A thin layer of a nematic fluid deposed upon a hard surface can display planar anchoring, i.e. alignment of the orientational order along the tangent direction to the surface [94]. Liquid

cristal films can be described, as a first approximation, by the XY model [95, 96]: when applied to spherical geometries, this approach shows geometric frustration, with the emergence of topological defects with total valence +2 [23, 97, 98]. Furthermore, the curvature of the surface can affect the direction of the global directional order [99] as well as the distribution of defects [100, 101], the interaction among them [102]. Until now, computational studies of liquid crystals on curved membranes were performed mainly with Monte Carlo dynamics [22, 23], while finite elements algorithms were successfully used for scalar systems [17]. However, while Monte Carlo models allow to accurately describe the topological patterns of nematics at equilibrium, the time evolution of the vector field describing the nematic would be more suitably described through the use of PDEs. We therefore built a model for the study of the evolution of a nematic field on a curved closed surface, using advanced methods for the numerical evaluation of the mathematical operators that arise in the equation of motion for the nematic fluid. We want to examine the influence of geometry on the relaxation of nematics on a curved surface, in order to provide a suitable model to simulate the dynamics of structures with orientational order on the surface of biological vesicles.

The plan of the chapter is the following: in the first section of this chapter we review the properties of nematic liquid crystals and set up a mathematical model for the study of a director field on a curved surface; we will then proceed to describe the numerical methods used to perform numerical calculations, concluding with the presentation and comment of the results of our simulations.

6.1 Nematic order on curved surfaces

In order to study the dynamics of nematic liquid crystals on a curved surface $\mathcal{M}$, a director field is needed to describe the local orientational order parameter at each point p of the surface. We want to use the director field to describe the orientational order of surface structures like cortical actin or septin filaments: both these structures have been characterised experimentally as being tangent to the plasma membrane [103, 104, 105, 106, 107, 108]. This director field is a unit

vector, that we require to be tangent to the surface; we can denote it[1] as a field $\mathbf{q}(p) = q^\mu(p)$, $\mu = 1, 2$. The free energy of the field must be a function of $\mathbf{q}$ and its derivatives, along with geometric quantities depending on the shape of the surface. Since the free energy functional needs to be invariant for coordinate transformations, it can contain only terms involving the scalar length of the director $|\mathbf{q}| = \sqrt{g_{\mu\nu} q^\mu q^\nu}$, and scalar terms derived from a contraction of the covariant derivative of the director field with another rank-2 tensor [109]. Since the norm of the field is fixed to $|\mathbf{q}| = 1$ at every point of the surface, the terms of the first kind are just constant terms in the bulk free energy density: let us call this term f_0, a constant term which represents the free energy of a uniformly aligned nematic. The other type of term present in the free energy is a distortion free energy that is constructed with the covariant derivatives of the director field. We choose it to be the trace of the square of the covariant derivative of q^μ, following the prescription of the one-constant approximation [110]. Hence, the free energy is described by the integral

$$\mathcal{F}[\mathbf{q}] = \int_{\mathcal{M}} d^2x \left[f_0 + \frac{G}{2} g^{\mu\nu} g_{\alpha\beta} D_\mu q^\alpha(\mathbf{x}) D_\nu q^\beta(\mathbf{x}) \right]. \tag{6.1}$$

Generally speaking, when describing the orientational order of a liquid crystal, a tensor quantity is needed. If $q_\mu = g_{\mu\nu} q^\nu$ is the local (covariant) director field, a traceless rank-2 tensor serves as order parameter:

$$S_{\mu\nu} = S \left(q_\mu q_\nu - \frac{1}{3} \delta_{\mu\nu} \right),$$

where $S \in [0, 1]$ is a scalar order parameter defining the degree of alignment between the fluid molecules. We here assume that the liquid crystal is locally in the nematic state, so that $S = 1$ at every point of the surface, and the order parameter can be more easily described with director fields, without needing to manipulate tensor quantities.

A major difference between a nematic liquid crystal and the phase field φ considered in the previous chapters is that while the scalar order parameter φ was globally conserved, the

[1] The director field is usually denoted with $\mathbf{n}$: since we are already using a vector $\mathbf{n}_i$ as the local unit normal to the surface, we choose to indicate by $\mathbf{q}$ the director in order to avoid ambiguity.

orientational order parameter $\mathbf{q}$ is not conserved anymore: when the system evolves from an initially disordered state to a globally aligned one, the initial average over all the surface points $|\langle\mathbf{q}\rangle_{\mathcal{M}}| = 0$ evolves to a nonzero average $|\langle\mathbf{q}\rangle_{\mathcal{M}}| = q_0$. For this reason, we chose a nonconservative model, following the dissertation by Leslie [111]: the evolution of the orientational order parameter is given by the equation

$$\dot{\mathbf{q}} = \mathbf{h}(\mathbf{q}),$$

where $\mathbf{h}$ is a m ıbouring points

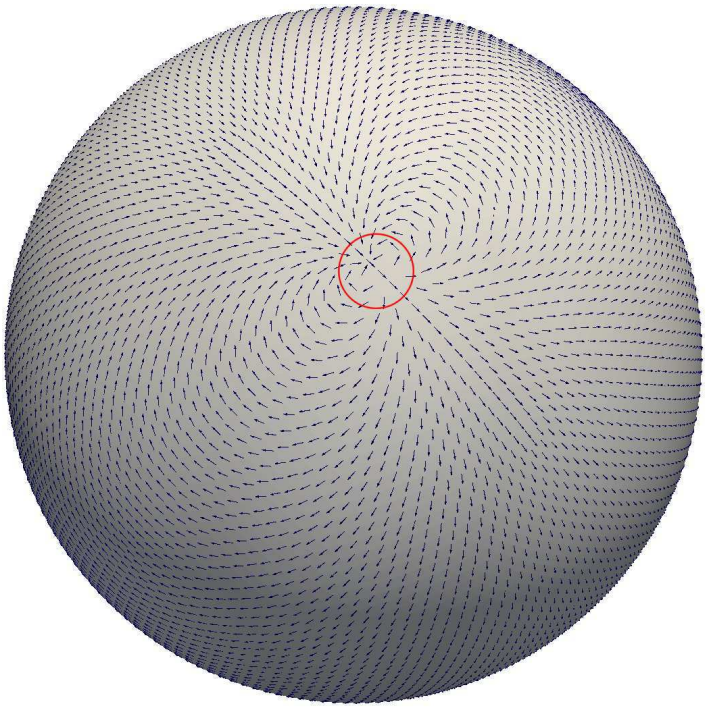

Figure 6.1: Tangent dipole field on a sphere: the field has just one singular point of index 2 (circled in red).

of the surface with average director field $\mathbf{q}$ [112]. The molecular field can be computed as the functional derivative of the free energy functional $\mathcal{F}[\mathbf{q}]$:

$$h^{\mu}(\mathbf{x}) = g^{\mu\nu}(\mathbf{x})\frac{\delta\mathcal{F}[\mathbf{q}]}{\delta q^{\nu}(\mathbf{x})}. \tag{6.2}$$

Given the free energy (6.1), we obtain

$$\frac{\delta \mathcal{F}[\mathbf{q}]}{\delta q^{\nu}(\mathbf{x})} = -G g_{\mu\nu}(\mathbf{x}) g^{\alpha\beta}(\mathbf{x}) D_{\beta} D_{\alpha} q^{\mu}(\mathbf{x}) = g_{\mu\nu} \nabla^2_{LB} q^{\mu}(\mathbf{x}),$$

that plugged into equation (6.2) gives the equation of motion for the director field

$$q^{\mu} = -G \nabla^2_{LB} q^{\mu}. \tag{6.3}$$

If the initial state is a disordered configuration in which the directions of $\mathbf{q}_i$ are randomly distributed on the surface, equation (6.3) relaxes the system to an ordered state where the director fields tends to align globally. The topology of the surface is now relevant in determining the pattern of defects in the ordered state: according to the Poincaré-Hopf theorem [113], the sum of the indices of the critical points of the field $\mathbf{q}$, where the direction is not univocally defined, must be equal to the Euler characteristic χ of the surface. This implies that on a sphere ($\chi = 2$) there must be at least one critical point of $\mathbf{q}$ with index 2 (see Fig. 6.1), or equivalently, one source and one sink. The latter is in fact the configuration we expect when the system, evolving via eq. (6.3), reaches a steady state: aligned vectors at all points with the exception of two singular points.

If we suppose that the structures displaying orientational order on the membrane have a preferred curvature, for example membrane proteins like amphiphysin and endophilin [42, 114], then the orientation of the structures is also relevant if a coupling between the curvature of the membrane and the surface order parameter is assumed. Specifically, if we model the order parameter as being preferentially oriented along the principal direction associated with the maximum principal curvature, in the steady state the orientation should be modulated by the curvature of the surface.

6.2 Numerical methods

We now want to discretise equation (6.3) to simulate it on a triangulated surface $\mathcal{M}$. In this respect, a representation of a vector field on the triangular mesh is needed, together with a correct definition of the local tangent space $T_p\mathcal{M}$ at point p and a discrete version of the Laplace-Beltrami operator for vector fields consistent with parallel transport.

6.2.1 Surface fields representations

The discretised surface where the vector field is defined is constituted by N vertices, E edges and F faces. In all the previous chapters, we implicitly assumed that the natural way to define a discrete scalar field φ on a triangle mesh is to construct an array $\mathbf{\Phi}_v$ of dimension N, with the i-th entry representing the value that φ takes on vertex i: we call this the *vertex based representation* of the field. Thus, the value that φ takes on each point on the edges and faces of the discretised surface is obtained by linear interpolation of the values in $\mathbf{\Phi}$. Given a point $\mathbf{u}$ on triangle $T(i,j,k)$ with barycentric coordinates $B_i(\mathbf{u})$, $B_j(\mathbf{u})$, $B_k(\mathbf{u})$, we can evaluate the field on $\mathbf{u}$ as $\varphi(\mathbf{u}) = \varphi_i B_i(\mathbf{u}) + \varphi_j B_j(\mathbf{u}) + \varphi_k B_k(\mathbf{u})$. In general, the choice of the vertex points of the mesh for the representation of the fields is not necessarily the most convenient one. One could choose to construct an array $\mathbf{\Phi}_e$ with E entries storing the values of φ on the midpoints of the edges, or an array $\mathbf{\Phi}_f$ of dimension F containing the values of the field at the barycenters of the triangular faces: these are named the edge-based and face-based representations of the field, respectively.

An example of this is seen when interpolating the edge- and face-based representations to evaluate it on the vertices: as we showed in the previous paragraph, in the vertex-based representation only three vertices are used to compute the value of the field on the barycenter of a face, and only two vertices for the midpoint value of an edge, whereas 5 to 6 values are used in both edge- and face-based representations, thus giving a more accurate estimate than the inverse. A summary of the pros and cons of the different representations is given by De Goes, Desbrun and Tong [115]: in the vertex-based representation, in the face-based repre-

sentation, the differential operators can be constructed by referring to the literature on finite element methods and the Helmholtz-Hodge decomposition of vector fields is simple, though some first and second order derivatives are ill-defined; the edge-based representation offers a coordinate-free representation and can rely on the discrete external calculus literature for the construction of differential operators, but the interpolation does not grant continuity of the fields at the vertices; the vertex-based representation allows continuous interpolation and the integral version of first and second order differential operators, yet the Hodge decomposition of a vector field is not clearly defined.

The edge- and face-based representations have some significant advantages in that they allow to draw the forms of the operators from literature on FEM [116, 117] and DEC [118, 119, 120]. Their major flaw, though, is the impossibility to consistently define a force acting on edges and faces in the same way that was done for the vertices in chapter 5, so we chose to keep the vertex-based representation. Even though its properties make more challenging some tasks such as the computation of normal vectors to the surface and the definition of local bases, this representation allows to avoid the inevitable errors that would be caused by interpolation of field values at each time step of the simulated dynamics.

6.2.2 Tangent spaces

In chapter 2 we introduced the notion of tangent planes to a surface in order to extend the definition of vector fields to a curved manifold $\mathcal{M}$. We now want to include this notion in our numerical model, by adapting it to a discrete setting. In order to represent tangent vectors as two-component real fields, we need to choose an orthonormal basis for each vertex in the mesh; we cannot thereupon use the same non-orthogonal reference frames which were used in section 2.3.

The method we use to construct the basis of the tangent space at vertex i is the following. We start by computing the normal $\mathbf{n}_i$ as explained in section 5.2.5. Then one of the edges departing from vertex i is chosen and projected onto the plane orthogonal to $\mathbf{n}_i$: normalising

this vector gives the first element $\mathbf{X}_i$ of the orthonormal basis. This first generator is then rotated counterclockwise by 90° around $\mathbf{n}_i$, producing the second basis vector $\mathbf{Y}_i = \mathbf{n}_i \wedge \mathbf{X}_i$, as shown in figure 6.2A. A vector field $\mathbf{V}$ at vertex i can then be expressed in terms of these basis vectors: $\mathbf{V}_i = V_i^1 \mathbf{X}_i + V_i^2 \mathbf{Y}_i$.

Once the bases are defined, we can follow the procedure by Zhang & al. [121] to rescale the angles at each vertex to sum 2π, in order to effectively "flatten" the vertices and push their curvature into the incident triangles. We thus assume that the curvature on a triangle is constant. Let then $T(i,j,k)$ be a triangle having i as one of its vertices and α_{ijk} the internal angle of $T(i,j,k)$ at i, as defined in section 5.2.5. We can compute the total vertex angle:

$$\theta_i = \sum_{T(i,j,k) \in \langle i \rangle} \alpha_{ijk},$$

so that the Gaussian curvature can be expressed as $K_i = 2\pi - \theta_i$. We can now define the angle scale factor

$$r_i = 1 + \frac{K_i}{\theta_i} = \frac{2\pi}{\theta_i},$$

which represents the deviation of the cell surrounding vertex i from euclidean geometry. On a flat surface, $K_i = 0$ and therefore $r_i = 1$, on surface with an engulfing or protrusion $K_i > 0$ and $r_i > 1$, and on a saddle region with negative curvature $K_i < 0$ and $0 < r_i < 1$. If we rescale each angle α_{ijk} by a factor r_i, we obtain a set of transformed triangles whose angles at i now correctly sum to 2π.

6.2.3 Parallel transport

Once the tangent spaces at each vertex and the corresponding geometry have been defined, the next step is to define the parallel transport from a vertex to another. If i and j are two neighbouring vertices of the mesh, let $\mathbf{e}_{ij}$ be the edge connecting them and $\gamma_i(\mathbf{X}_i, \mathbf{e}_i j)$ the rescaled angle between base vector $\mathbf{X}_i$ in the tangent plane $T_i\mathcal{M}$. The angle between the

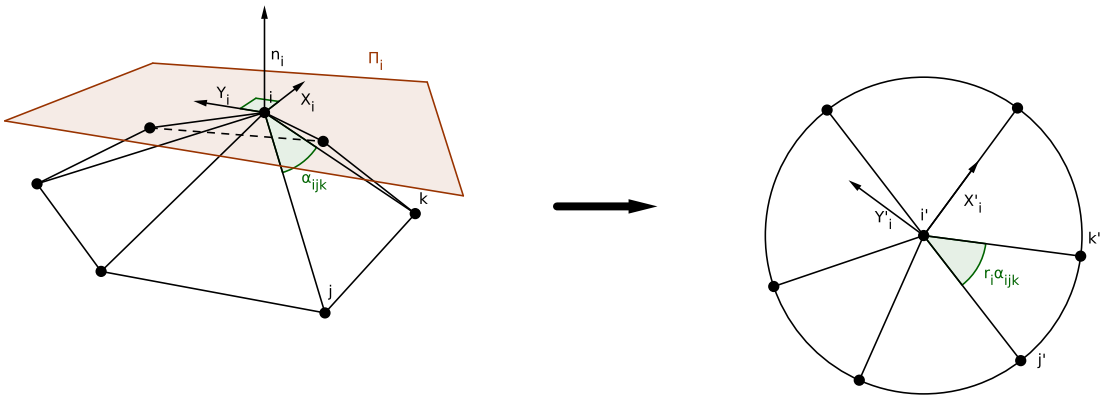

(A) (B)

Figure 6.2: Local tangent space at vertex i and flattening of the vertex. The cell of figure (A) is projected onto the tangent space Π_i and the angles are consistently rescaled, obtaining the geometry of figure (B).

reference frames of $T_i\mathcal{M}$ and $T_j\mathcal{M}$ is then computed as

$$\rho_{ij} = \gamma_j(\mathbf{X}_j, \mathbf{e}_{ij}) - \gamma_i(\mathbf{X}_i, \mathbf{e}_{ij}).$$

We can now define, for each oriented edge of the mesh, the transport matrix $r_{ij} = R(\rho_{ij})$, where $R(\omega)$ is the counterclockwise rotation of an angle ω on $T_j\mathcal{M}$. The application of this rotation to a vector in $T_j\mathcal{M}$ allows to transport it to $T_i\mathcal{M}$ in a consistent way, without getting contradictory situations as the one depicted in figure 2.1, where the direction of a vector depends on the local coordinates (see Fig. 6.3).

6.2.4 Laplace-Beltrami for vector fields

In order to compute the integrals needed to evaluate the action of the Laplace-Beltrami operator on a vector field, the holonomy $\Omega_{ijk} \in]-\pi, \pi]$ is needed. This angle represents the curvature of the tangent space over triangle $T(i, j, k)$ (which is constant for every point of the triangle), and it can be computed as the argument of the rotation matrix given by the product of the

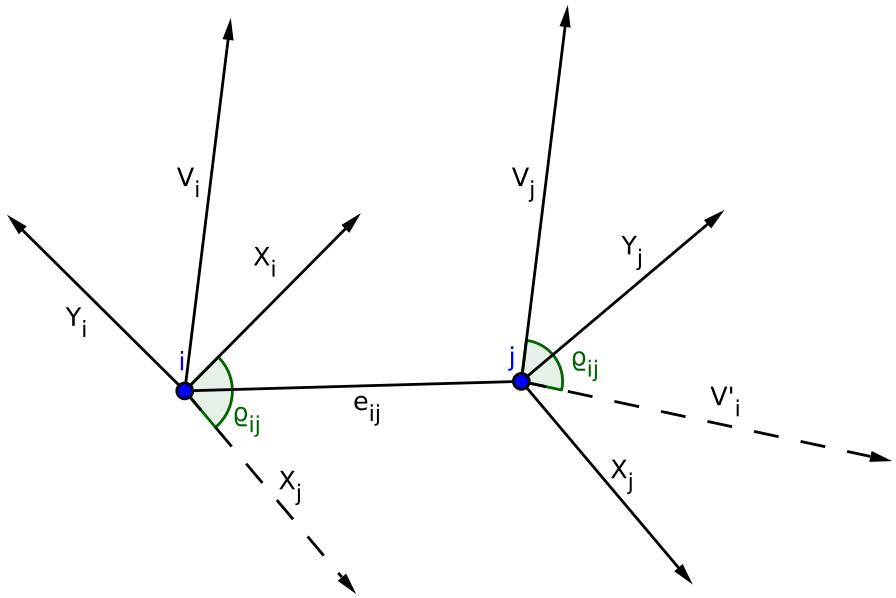

Figure 6.3: Transport of a vector from vertex i to vertex j. Given vector $\mathbf{V}_i$ of coordinates (V_{ix}, V_{iy}) in the local basis $\{\mathbf{X}_i, \mathbf{Y}_i\}$, translating it to vertex j produces the vector $\mathbf{V}'_i = V_{ix}\mathbf{X}_j + V_{iy}\mathbf{Y}_j$ displayed in the figure. This is clearly not parallel to $\mathbf{V}_i$: in order to recover the correct orientation, we need to rotate it by the angle ρ_{ij} between the two bases.

transport matrices around the perimeter of a triangle:

$$R(\Omega_{ijk}) = r_{ij} r_{jk} r_{ki}.$$

We use the expression for the vector laplacian given by Knöppel & al. [72], first on each triangle $T(i, j, k)$ and then obtained for each vertex upon summation over the neighbouring triangles. The derivation of the operator is based on the extension of basis vectors $\mathbf{X}_i, \mathbf{Y}_i$ to the incident triangles and evaluation of the derivatives on the basis obtained this way are explained in detail in appendix B. Note that since we are dealing with vector fields, each element of the Laplace-Beltrami operator needs to be a 2×2 real matrix acting on 2-vectors. The integrals per triangle of diagonal and off-diagonal elements of the laplacian matrix are given by:

$$\langle \Delta_{ii} \rangle_{ijk} \quad = \quad \frac{\mathbb{I}}{4A_T} \left[|\mathbf{e}_{ij}|^2 + \Omega_{ijk}^2 \frac{|\mathbf{e}_i j|^2 + \mathbf{e}_{ij} \cdot \mathbf{e}_{ik} + |\mathbf{e}_{ik}|^2}{90} \right]$$

$$\langle \Delta_{jk} \rangle_{ijk} = \frac{r_{kj}}{A_T} \left[\left(|\mathbf{e}_{ij}|^2 + |\mathbf{e}_{ik}|^2 \right) f_1(\Omega_{ijk}) + \mathbf{e}_{ij} \cdot \mathbf{e}_{ik} f_2(\Omega_{ijk}) \right], \tag{6.4}$$

where $\mathbb{I}$ is the 2×2 identical matrix, and the functions f_1 and f_2 are matrix operators defined as follows:

$$\begin{aligned}
R_1(s) &= \left(\frac{3}{s^2} + \frac{1}{24} \right) + \left(\frac{s^2}{2} - 3 \right) \frac{\cos(s)}{s^4} - 2\frac{\sin(s)}{s^4}, \\
I_1(s) &= s \left(\frac{1}{s^4} - \frac{1}{60} \right) + 2\frac{\cos(s)}{s^3} + \left(\frac{s^2}{2} - 3 \right) \frac{\sin(s)}{s^4}, \\
R_2(s) &= \left(s^2 - 4 \right) \cos(s) - 3s \sin(s), \\
I_2(s) &= 3s \cos(s) + \left(s^2 - 4 \right) \sin(s), \\
f_1(s) &= \begin{pmatrix} R_1(s) & -I_1(s) \\ I_1(s) & R_1(s) \end{pmatrix}, \qquad f_2(s) = \begin{pmatrix} R_2(s) & -I_2(s) \\ I_2(s) & R_2(s) \end{pmatrix}.
\end{aligned} \tag{6.5}$$

Note that, in the flat limit, the holonomy Ω_{ijk} tends to zero, and the off-diagonal term has a removable singularity: by computing the limits for $s \to 0$ of $R_1(S)$, $I_1(s)$, $R_2(s)$ and $I_2(s)$, we easily obtain

$$R_1(0) = 0, \qquad I_1(0) = 0, \qquad R_2(0) = -\frac{1}{4}, \qquad I_2(0) = 0,$$

so that the off-diagonal element of the laplacian operator converges to the limit

$$\langle \Delta_{jk} \rangle_{ijk} = -r_{kj} \frac{\mathbf{e}_{ij} \cdot \mathbf{e}_{ik}}{4A_T} = -\frac{1}{2} r_{kj} \cot(\alpha_{ijk}),$$

which is just the vector version of the cotan laplacian defined in section 5.2.3.

6.3 Results

We performed a simulation of a director field $\mathbf{q}$ evolving on a spherical surface. The initial configuration is chosen by defining for each vertex of the mesh a unit vector $\mathbf{q}_i$, whose angle with the basis vector $\mathbf{X}_i$ is picked randomly from a uniform distribution with values in the

interval $[0, 2\pi[$. The system is quenched at $t = 0$ and follows a relaxation of the directions of $\mathbf{q}$, according to equation 6.3. Initially the orientational order forms locally, with domains of same orientation forming in different regions of the surface. Then the directors $\mathbf{q}$ start to align over a region the size of the membrane, leading to an overall homogeneous orientation, with local variations and defects. The defects then start to anneal until only two defects of $\mathbf{q}$ are left, namely one source and one sink - each one of index 1, respecting the equilibrium conditions imposed by the Poincaré-Hopf theorem.

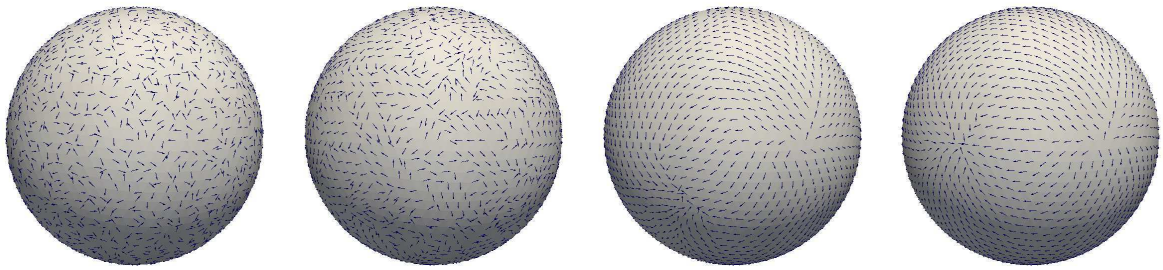

Figure 6.4: Time evolution of a nematic field on a spherical membrane. After an initial isotropic configuration, the orientational order start to form first locally and then globally. All the residual defects then anneal, with the exception of one source and one sink.

Chapter 7

Conclusions

In this thesis we have performed a theoretical study, based on numerical simulations of several models of phase separation, patterning dynamics and orientational order on closed surfaces that can be either rigid or fluctuating in shape. In designing our models we have been inspired by physical and biological examples such as the shape evolution of some biological membranes and the dynamics of some order parameter fields describing the concentration of some molecules diffusing in the membranes. In order to carry out these investigations, we have implemented discrete versions of differential operators on curved surfaces, both by using finite difference and finite element schemes. Among the numerical achievements we had to reach it is worth mentioning the implementation of finite difference covariant derivatives of scalar and vector fields on curved surfaces, and the finite element version of the laplacian of a vector field.

In chapters 1 and 2 we introduced the topics of our study and reviewed concepts of differential geometry needed to properly describe the system and the numerical techniques required to solve the corresponding partial differential equations on manifolds. This set of tools was then used to study a variety of situations, reflecting cases of physical and biological interest.

More precisely, in chapter 3 we addressed the question of whether the phase separation dynamics of binary mixture like systems can be affected by the curvature of the surface on which they evolve. The paradigmatic model that we have considered is the Cahn-Hilliard equation for

phase separation of binary systems, where the order parameter describing the local difference in concentration of the two components is a conserved quantity that evolves according to a model B dynamics. We showed that, when the model is merely evolving on the surface the results are independent of the local geometry, although the steady-state configurations display different degrees of degeneration depending on the rotational symmetry group of the surface. The situation changes radically if a direct coupling between the local mean curvature and the order parameter is considered. In particular, if the coupling is sufficiently strong, interesting features such as arrested phase separation and multi-domains patterns driven by the surface curvature are observed. We understood this behaviour in terms of a competition between the local curvature, that favours the formation of domains of a specific phase in definite regions of the surface and the interfacial free energy that tends to reduce the length of the interface between phases and consequently drives the coarsening of the domains. Quite remarkably this mechanism when present on surfaces with non-homogeneous mean curvature such as ellipsoids or spheres with gaussian protrusions allows to tune the number of domains present at the steady state by appropriately choosing the intensity of the coupling.

In chapter 4 we introduced a further complication to the model by adding, to the phase separation dynamics, a reaction-diffusion system. This can model, for example the behaviour of membrane proteins coupled to the lipid bilayer [122, 123, 124]. After reviewing the theory of pattern formation on flat and curved spaces, we coupled the diffusivity of the reactants in the patterning reaction with the local composition of the lipids in the membrane. The resulting effective coupling between the reaction-diffusion dynamics and the one of the phase separation gives rise, when arrested coarsening of chapter 3 occurs, to a clear selection of the position and size of the patterns by the local curvature of the surface. Besides, the geometry of the surface determines the shape of the domains in which patterning is allowed, which, in turn, influences the patterning modes, so that the geometry of patterns reflects the one of the underlying surface in a nontrivial way. The chapter ends with the study of another model of pattern localisation and arrested phase separation that is inspired by binary mixtures in presence of surfactant and

the physics of lamellar phases.

So far we have considered rigid surfaces. This situation might be representative of real systems when the dynamics of the fields is much faster the one governing the surface shape. When this is not the case the evolution of the surface shape has to be considered as well. This is done in chapter 5 where the shape dynamics of the surface depends on physical properties such as its response under stretching, bending and osmotic pressure as well as on the local concentration of the phase separating field. More precisely, by complementing a finite element description of unit normal field, mean curvature and Laplace-Beltrami operator, we have been able to set up a numerical model of a physical membrane that is subject to a force directed along its normal and proportional to the values of the phase field: this term mimics the action of curvature-inducing membrane molecules. By tuning the mechanical parameters of the closed surface and the strength of the coupling between the phase field and the curvature we showed that different shapes can be formed with the number of connected phase domains in the steady state being proportional to the strength of the curvature coupling.

Finally, in chapter 6, we extend the model of a scalar field to the case of a liquid crystal nematic with planar anchoring to a curved surface. The main challenge here was the construction of a Laplace-Beltrami operator acting on a director field, consistently with the theory of parallel transport of vectors on a surface. We adapted a numerical method introduced very recently in computer graphics and tested it to the paradigmatic model of the relaxation dynamics of a nematic field on a spherical surface, reproducing the well-established dynamics of annealing of topological defects consistently with the geometry of the surface.

Starting from this thesis, extensions can be carried in the near future regarding the different aspects of the numerical studies of field on evolving vesicles. With regard to the arrested coarsening on curved surfaces (see 4.4), the lamellar phase induced by the presence of a surfactant can be explored more in depth, investigating the possible patterning modes induced on surfaces with different shapes; this in turn makes possible the experimental validation of the model, by observing giant unilamellar vesicles of fixed shape and with varying concentration of a surfac-

tant (e.g. cholesterol). The model for dynamic evolution of bicomponent vesicles presented in chapter 5 can be made more precise by replacing the normal force F^{φ} with a force derived from a free energy acting on the surface; on the other hand, comparison with the model of shrinking vesicle by Quemeneur & al. [61] could provide insight on the reason why the two models lead to similar equilibrium configurations in spite of their difference. The coupling of the director field of chapter 6 with the curvature of the surface and its back-action on the shape of the vesicle itself: these will require a discrete approximation of the shape operator that is compatible with the algorithms used for the curvature. Moreover, the successful test of differential operators for vector fields on curved surfaces paves the way for the exploration of active polar fields on closed vesicles and their influence on the geometry of the vesicle surface. For all the models presented in this work, an analysis of the hydrodynamical interactions and thermal noise on the membrane would be necessary in order to understand whether our equilibrium models reflect real systems or need to be refined. A useful research that could be useful for this last purpose would be the adaptation of the theoretical models to real systems, using experimental data to predict the time evolution of several stages of the life of biological vesicles in which membrane dynamics play an important role, such as cell division and other structural transitions.

Appendix A

Differential geometry of manifolds

Definition 1 *A Hausdorff topological space $\mathcal{M}$ is called a* topological manifold *if for each point $p \in \mathcal{M}$ there is a* chart *(U_p, ψ_p), with $U_p \in \mathcal{M}$ an open neighbourhood of p and $\psi_p : U_p \to \mathbb{R}^2$ a homeomorphism. A set of charts covering the whole surface $\mathcal{M}$ is called an* atlas*.*

Since in general we have surfaces which are not globally homeomorphic to the euclidean plane, we need to consider different maps of $\mathcal{M}$. To be sure that the local reference frames on the surface do not have any hole, we must be able to define transition functions between maps in the non-void intersection of the defining neighbourhood. This is where the differential structure arises:

Definition 2 *Two maps $(U_p, \psi_p), (U_q, \psi_q)$ on a topological surface $\mathcal{M}$ are $\mathcal{C}^k$-compatible if the transition function $f_{pq} = \psi_p \circ \psi_q^{-1}$ is a $\mathcal{C}^k$-differentiable function along with its inverse. A $\mathcal{C}^k$-differential surface is a topological surface provided with an atlas of maps which are two by two $\mathcal{C}^k$-compatible.*

In our work we restrict ourselves to the case of smooth surfaces, i.e. $\mathcal{C}^\infty$-differential surfaces. This allows to define smooth scalar functions and smooth curves on manifold $\mathcal{M}$:

Definition 3 *A scalar function on a manifold $\mathcal{M}$ is a function $f : \mathcal{M} \to \mathbb{R}$. A curve is a function $\gamma : \mathbb{R} \to \mathcal{M}$.*

A scalar function is smooth if the composition $\psi_p^{-1} \circ f : \mathbb{R}^2 \to \mathbb{R}$ is $\mathcal{C}^\infty$; similarly, a smooth curve is a curve such that $\gamma \circ \psi_p : \mathbb{R} \to \mathbb{R}^2$ is $\mathcal{C}^\infty$. The notion of curve is crucial to define vectors on surface $\mathcal{M}$:

Definition 4 *The* tangent space *to a manifold $\mathcal{M}$ at a point p is defined as the set of equivalence classes*

$$T_p\mathcal{M} := \frac{\left\{\gamma : \mathbb{R} \to \mathcal{M} | \gamma(0) = p, \exists\, \gamma^{(n)}\, \forall\, n > 0\right\}}{\left\{\gamma \sim \gamma' \text{ if } \left.\frac{d\psi_p \circ \gamma}{dt}\right|_{t=0} = \left.\frac{d\psi_p \circ \gamma'}{dt}\right|_{t=0}\right\}},$$

and the elements of this set are the vectors *of $T_p\mathcal{M}$. The disjoint union of all the $T_p\mathcal{M}$ of $\mathcal{M}$ is called the* tangent bundle *$T\mathcal{M}$ of the manifold.*

Given a tangent vector $V \in T_p\mathcal{M}$, the operation of directional derivative along V is univocally identified, regardless of the coordinate choice.

Definition 5 *Given a tangent vector V along a curve γ to $\mathcal{M}$ and real-valued scalar function f on $\mathcal{M}$, the* directional derivative *of f along V is defined as the map*

$$D_V : f \mapsto \left.\frac{d\,(f \circ \gamma)}{dt}\right|_{t=0}.$$

By writing the directional derivative in 2-dimensional real components x^i through the chart ψ_p, we identify the directional derivatives ∂_i as the basis for the tangent space at point p:

$$D_V f(p) = \left.\frac{dx^i}{dt}\,\frac{df}{dx^i}\right|_{t=0} = V^i \partial_i f.$$

This way we can define a vector field as a section of the tangent bundle which associates a single vector on the tangent space at each point p of $\mathcal{M}$:

Definition 6 *A* vector field *on $\mathcal{M}$ is a differentiable function that associates to each point $p \in \mathcal{M}$ a single vector on the tangent plane $T_p\mathcal{M}$.*

Clearly, since there is a definition of vectors, linear operators can be defined as well:

Definition 7 *A* covector *on tangent plane $T_p\mathcal{M}$ is a linear operator $T : T_p\mathcal{M} \to \mathbb{R}$. The space of covectors is called the cotangent plane $T_p^*\mathcal{M}$.*

A basis for the space of covectors is constituted by the differentials dx^i, in a way that $dx^i\partial_j = \delta^i_j$. Let's now consider the space generated by the direct product of r copies of $T_p\mathcal{M}$ and s copies of $T_p^*\mathcal{M}$, and generalise here the notion of covector:

Definition 8 *A* tensor *is a linear operator $T : T_p\mathcal{M} \otimes \cdots \otimes T_p\mathcal{M} \otimes T_p^*\mathcal{M} \otimes \cdots \otimes T_p^*\mathcal{M} \to \mathbb{R}$. The space of tensors on $T_p\mathcal{M}$ is indicated with $T^r_s(T_p\mathcal{M})$.*

A tensor can be identified with its components with respect to the basis of the domain, obtained via direct product of the bases of the r copies of the tangent space and the s copies of the cotangent space. This lead to a representation with r high indices, called contravariant components, and s low indices, or covariant indices. The sum over two equal indices of a tensor in $T^r_s(T_p\mathcal{M})$ at different heights is called the contraction of the indices, which produces a new tensor of $T^{r-1}_{s-1}\mathcal{S}$.

Proposition 1 *Under a change in coordinates $x \mapsto x'$, a tensor $T^{i_1\cdots i_r}_{j_1\cdots j_s}$ transforms as*

$$T'^{k_1\cdots k_r}_{l_1\cdots l_s} = \frac{dx^{k_1}}{dx'^{i_1}}\cdots\frac{dx^{k_r}}{dx'^{i_r}}\frac{dx'^{j_1}}{dx^{l_1}}\cdots\frac{dx'^{j_s}}{dx^{l_s}}T^{i_1\cdots i_r}_{j_1\cdots j_s}.$$

Proof 1 *The tensor is a real-valued linear operator $T(\mathbf{x}) = T^{i_1\cdots i_r}_{j_1\cdots j_s}\partial_{i_1}\cdots\partial_{i_r}dx^{j_1}\cdots dx^{j_s}$. Under a change of coordinates the elements of the basis transform as*

$$\partial'_k = \frac{d}{dx'^k} = \frac{dx^i}{dx'^k}\frac{d}{dx^i}, \qquad dx'^l = \frac{dx'^l}{dx^j}dx^j.$$

By applying the transformation to the base vectors and grouping the transformation matrices together with the tensor component, we obtain the desired expression. □

We now introduce a particular tensor, which can be used to raise or lower indices, and generalises the notion of scalar product to a curved manifold.

Definition 9 *A* metric tensor *is a rank-2 contravariant tensor $g_{\mu\nu}$ that is symmetric for swapping of the indices and nondegenerate, i.e. if one of the indices is contracted with a non-null vector V^μ, the vector field $g_{\mu\nu}V^\mu W^\nu$ does not take the value 0 for any vector $W^\nu \neq 0$. A metric tensor with a positive signature is called a* Riemann metric*, and a manifold provided with a Riemann metric is called a* Riemann manifold *$(\mathcal{M}, g)$.*

Since it is nondegenerate, the metric tensor has an inverse $g^{\mu\nu}$ such that $g_{\mu\nu}g^{\nu\rho} = \delta^\rho_\mu$. The metric and its inverse establish a bijective correspondence between $T\mathcal{M}$ and $T^*\mathcal{M}$, thus for each vector V^μ a covector $V_\mu = g_{\mu\nu}V^\nu$ is defined.

The properties of transformation stated in Prop. 1 imply that the directional derivative *does not act as a tensor* when applied to a nonscalar field.

Proposition 2 *The directional derivative of a vector field does not transform as a tensor.*

Proof 2 *Let $x \mapsto x'$ be a transformation of coordinates, and $V^\mu(x)$ a vector field. Then under the change of coordinates, the derivative of the vector field will transform as*

$$\partial'_\mu V'^\nu(x') = \frac{dx'^\rho}{dx^\mu}\partial_\rho\left(\frac{dx^\nu}{dx'^\sigma}V^\sigma(x)\right) = \frac{dx'^\rho}{dx^\mu}\frac{dx^\nu}{dx'^\sigma}\partial_\rho V^\sigma(x) + \frac{dx'^\rho}{dx^\mu}V^\sigma(x)\partial_\rho\frac{dx^\nu}{dx'^\sigma}. \tag{A.1}$$

The first term of the right side of the expression is a tensor, but the second one is not. □

In order to construct a tensor derivative we therefore need to introduce a counterterm to cancel the non-tensor quantity in (A.1). This is done through differentiation of the metric tensor, and the resulting operator is called the covariant derivative.

Definition 10 *The* covariant derivative *of a tensor $T^{i_1\cdots i_r}_{j_1\cdots j_s}$ on a Riemann manifold $(\mathcal{M}, g)$ is defined as the operator D_μ acting on scalar fields as the usual directional derivative ∂_μ, and on a tensor $T^{i_1\cdots i_r}_{j_1\cdots j_s}$ as the derivative plus a correction term $+\Gamma^{i_k}_{\mu\nu}T^{i_1\cdots i_{k-1}\nu i_{k+1}\cdots i_r}_{j_1\cdots j_s}$ for each contravariant index, and $-\Gamma^{i_\nu}_{\mu k}T^{i_1\cdots i_r}_{j_1\cdots i_{k-1}\nu i_{k+1}\cdots j_s}$ for each covariant index. The* Christoffel symbol

(or affine connection*)* $\Gamma^{\rho}_{\mu\nu}$ *is defined as*

$$\Gamma^{\rho}_{\mu\nu} = \frac{1}{2} g^{\rho\sigma} \left(\partial_{\mu} g_{\sigma\nu} + \partial_{\nu} g_{\mu\sigma} + \partial_{\sigma} g_{\mu\nu} \right).$$

This term cancels exactly the non-tensor quantity in the change of coordinates of a directional derivative, providing a differential operator that transforms as a tensor. Using the explicit formula for the metric tensor (2.4) we can write the Christoffel symbol as a function of the derivatives of the coordinates $\mathbf{x}$ of the surface points: plugging expression (2.4) into the definition of the Christoffel symbol we obtain the explicit formula

$$\Gamma^{\rho}_{\mu\nu}(\mathbf{x}) = g^{\rho\sigma}(\mathbf{x}) \partial_{\sigma}\mathbf{x} \cdot \partial_{\mu}\partial_{\nu}\mathbf{x}. \tag{A.2}$$

The Christoffel symbols play an important role in the intrinsic characterisation of the differential geometry of a surface. Not only they are needed to define a directional derivation operator consistent with the parallel transport over the tangent bundle, but they can be used to derive an intrinsic definition of the curvature. To be able to see this latter result, we need to define the second fundamental form, an extrinsic tensor quantity needed to compute the curvatures of the surface at a point p.

Definition 11 *If* $\mathbf{n}(p)$ *is the local outward unit normal vector to surface* $\mathcal{M}$ *and* $\mathbf{x}(p)$ *the coordinates of the point, the second fundamental form is defined as*

$$b_{\mu\nu}(p) = \partial_{\mu}\partial_{\nu}\mathbf{x}(p) \cdot \mathbf{n}(p). \tag{A.3}$$

A relevant property of the second fundamental form is that it allows to write the directional derivative of the normal vector in terms of the local tangent vectors:

Proposition 3 (Weingarten equation) *For a Riemann manifold* $(\mathcal{M}, g)$ *with fundamental form* $b_{\mu\nu}$*, the following relationship intercurs between the directional derivative of the local unit*

normal $\mathbf{n}$ *and the basis vectors* $\partial_\mu \mathbf{x}$ *of the tangent space* $T_p\mathcal{M}$ *at point* p*:*

$$\partial_\nu \mathbf{n} = -b^\mu{}_\nu \partial_\mu \mathbf{x} \tag{A.4}$$

Proof 3 *Equation (A.4) can be expanded as*

$$\partial_\nu \mathbf{n} = -g^{\mu\rho} b_{\rho\nu} \partial_\mu \mathbf{x},$$

and taking the scalar product of both sides of this equation by $\partial_\sigma \mathbf{x}$ *we obtain*

$$\partial_\nu \mathbf{n} \cdot \partial_\sigma \mathbf{x} = -g^{\mu\rho} b_{\rho\nu} \partial_\mu \mathbf{x} \cdot \partial_\sigma \mathbf{x}.$$

Since the first fundamental form is derived explicitly as the scalar product $g_{\mu\sigma} = \partial_\mu \mathbf{x} \cdot \partial_\sigma \mathbf{x}$*, we get the result*

$$\partial_\nu \mathbf{n} \cdot \partial_\sigma \mathbf{x} = -g^{\mu\rho} b_{\rho\nu} g_{\mu\sigma} = -b_{\sigma\nu}$$

This last expression can be written as

$$b_{\sigma\nu} = -\partial_\nu \left(\mathbf{n} \cdot \partial_\sigma \mathbf{x} \right) + \mathbf{n} \cdot \partial_\nu \partial_\sigma \mathbf{x},$$

and since $\partial_\sigma \mathbf{x}$ *is a tangent vector and* $\mathbf{n}$ *is normal, their scalar product is zero, and we recover the correct expression for the second fundamental form*

$$b_{\sigma\nu} = \partial_\nu \partial_\sigma \mathbf{x} \cdot \mathbf{n},$$

which proves the Weingarten formula. □

The second fundamental form essentially measures the displacement of a geodesic on the surface on the normal direction, formalising the intuitive concept of curvature. The gaussian curvature of the surface is computed as the product of the eigenvalues of the second fundamental form,

i.e. the determinant of the tensor:

Definition 12 *Given a Riemann manifold $(\mathcal{M}, g)$ with second fundamental form b, the* gaussian curvature *at a point $p \in \mathcal{M}$ is given by the determinant*

$$K(p) = \det(b^{\mu}_{\nu}(p)) = \frac{\det(b_{\mu\nu}(p))}{\det(g_{\mu\nu}(p))}.$$

With the quantities we have defined, we can express the second derivative of the coordinates of a point p in terms of the Christoffel symbols and the second fundamental form.

Proposition 4 *Given a point $p \in \mathcal{M}$ of coordinates $\mathbf{x}$, its second derivatives along curvilinear coordinates $\mu = 1, 2$ of $T_p\mathcal{M}$ are given by the* Gauss formula

$$\partial_\mu \partial_\nu \mathbf{x} = \Gamma^{\rho}_{\mu\nu} \partial_\rho \mathbf{x} + b_{\mu\nu}\mathbf{n} \tag{A.5}$$

Proof 4 *The tangent component of the second derivative $\partial_\mu\partial_\nu\mathbf{x}$ is given by its scalar product with the vectors $\partial_\mu\mathbf{x}$ that constitute the basis of the tangent space $T_p\mathcal{M}$. Recalling expression (A.2) for the Chrystoffel symbols, we obtain*

$$\langle \partial_\sigma \mathbf{x}, \partial_\mu\partial_\nu\mathbf{x} \rangle = g^{\rho\sigma}\partial_\sigma\mathbf{x} \cdot \partial_\mu\partial_\nu\mathbf{x} = \Gamma^{\rho}_{\mu\nu}.$$

For the normal component, we take the scalar product of the second derivative of the coordinate points with the normal vector $\mathbf{n}$:

$$\mathbf{n} \cdot \partial_\mu\partial_\nu\mathbf{x} = b_{\mu\nu}.$$

Thus, the expression of the second directional derivative of $\mathbf{x}$ in the local frame $(\partial_1\mathbf{x}, \partial_2\mathbf{x}, \mathbf{n})$ is given by

$$\partial_\mu\partial_\nu\mathbf{x} = \Gamma^{\rho}_{\mu\nu}\partial_\rho\mathbf{x} + b_{\mu\nu}\mathbf{n},$$

which concludes the proof. □

With the results obtained so far, we now want to draw a link between the extrinsic measure

$b_{\mu\nu}$ of the curvature and intrinsic quantity $\Gamma^{\rho}_{\mu\nu}$.

Theorem 1 (Theorema Egregium) *Given a Riemann manifold* $(\mathcal{M}, g)$*, the* Riemann curvature tensor *at point* p *is defined as*

$$R^{\rho}{}_{\sigma\mu\nu} = \partial_\mu \Gamma^{\rho}_{\nu\sigma} - \partial_\nu \Gamma^{\rho}_{\mu\sigma} + \Gamma^{\rho}_{\mu\lambda}\Gamma^{\lambda}_{\nu\sigma} - \Gamma^{\rho}_{\nu\lambda}\Gamma^{\lambda}_{\mu\sigma}.$$

The gaussian curvature of the surface is then given by the formula

$$K = \frac{g_{2\sigma} R^{\sigma}{}_{121}}{\det(g_{\mu\nu})}. \tag{A.6}$$

Proof 5 *We begin by taking the third derivative of the coordinate points. Using Gauss formula (A.5), we have*

$$\begin{aligned}
\partial_\mu\partial_\nu\partial_\rho \mathbf{x} &= \partial_\mu\left(\Gamma^{\sigma}_{\nu\rho}\partial_\sigma \mathbf{x} + b_{\nu\rho}\mathbf{n}\right) = \left(\partial_\mu \Gamma^{\sigma}_{\nu\rho}\right)\partial_\sigma \mathbf{x} + \Gamma^{\sigma}_{\nu\rho}\partial_\mu\partial_\sigma \mathbf{x} + \left(\partial_\mu b_{\nu\rho}\right)\mathbf{n} + b_{\nu\rho}\partial_\mu \mathbf{n} \\
&= \left(\partial_\mu \Gamma^{\sigma}_{\nu\rho}\right)\partial_\sigma \mathbf{x} + \Gamma^{\sigma}_{\nu\rho}\left(\Gamma^{\lambda}_{\mu\sigma}\partial_\lambda \mathbf{x} + b_{\mu\sigma}\mathbf{n}\right) + \left(\partial_\mu b_{\nu\rho}\right)\mathbf{n} - b_{\nu\rho}b^{\sigma}{}_{\mu}\partial_\sigma \mathbf{x} \\
&= \left(\partial_\mu \Gamma^{\sigma}_{\nu\rho} + \Gamma^{\lambda}_{\nu\rho}\Gamma^{\sigma}_{\mu\lambda} - b_{\nu\rho}b^{\sigma}{}_{\mu}\right)\partial_\sigma \mathbf{x} + \left(\Gamma^{\sigma}_{\nu\rho}b_{\mu\sigma} + \partial_\mu b_{\nu\rho}\right)\mathbf{n}.
\end{aligned}$$

By exchanging indices μ *and* ν *we obtain the expression*

$$\partial_\nu\partial_\mu\partial_\rho \mathbf{x} = \left(\partial_\nu \Gamma^{\sigma}_{\mu\rho} + \Gamma^{\lambda}_{\mu\rho}\Gamma^{\sigma}_{\nu\lambda} - b_{\mu\rho}b^{\sigma}{}_{\nu}\right)\partial_\sigma \mathbf{x} + \left(\Gamma^{\sigma}_{\mu\rho}b_{\nu\sigma} + \partial_\nu b_{\mu\rho}\right)\mathbf{n},$$

and since $\partial_\mu\partial_\nu\partial_\rho \mathbf{x} = \partial_\nu\partial_\mu\partial_\rho \mathbf{x}$*, we obtain the equivalence*

$$\partial_\mu \Gamma^{\sigma}_{\nu\rho} + \Gamma^{\lambda}_{\nu\rho}\Gamma^{\sigma}_{\mu\lambda} - b_{\nu\rho}b^{\sigma}{}_{\mu} = \partial_\nu \Gamma^{\sigma}_{\mu\rho} + \Gamma^{\lambda}_{\mu\rho}\Gamma^{\sigma}_{\nu\lambda} - b_{\mu\rho}b^{\sigma}{}_{\nu},$$

which allows to define the Riemann curvature tensor as

$$R^{\sigma}{}_{\rho\mu\nu} = \partial_\mu \Gamma^{\sigma}_{\nu\rho} - \partial_\nu \Gamma^{\sigma}_{\mu\rho} + \Gamma^{\sigma}_{\mu\lambda}\Gamma^{\lambda}_{\nu\rho} - \Gamma^{\sigma}_{\nu\lambda}\Gamma^{\lambda}_{\mu\rho} = b_{\nu\rho}b^{\sigma}{}_{\mu} - b_{\mu\rho}b^{\sigma}\nu.$$

Now we can write equation (A.6) as

$$K = \frac{g_{2\sigma} R^{\sigma}{}_{121}}{\det(g_{\mu\nu})} = \frac{b_{11}b_{22} - b_{21}b_{12}}{\det(g_{\mu\nu})} = \frac{\det(b_{\mu\nu})}{\det(g_{\mu\nu})},$$

recovering the explicit formula for the gaussian curvature. □

The theorem we present here constitutes an important connection between the geometry of the surface and its topology. For every closed surface, the following holds:

Theorem 2 (Gauss-Bonnet) *Given a compact two-dimensional Riemann manifold* $(\mathcal{M}, g)$*, let* $K(p)$ *be the local curvature at point* $p \in \mathcal{M}$*,* $\chi(\mathcal{M})$ *the Euler characteristic of the surface, and* dA *the area element of the surface. The following equivalence holds:*

$$\int_{\mathcal{M}} dA(p) K(p) = 2\pi\chi(\mathcal{M}).$$

For the proof, see reference [113].

Appendix B

Discrete vector laplacian on curved manifolds

We explain here the construction of the discrete Laplace-Beltrami operator for vector fields on triangulated surfaces, following [72]. The formalism is based on a representation of 2D vectors on the tangent bundle as complex numbers, so that a vector $\mathbf{V}_i = V_{ix}\mathbf{X_i} + V_{iy}\mathbf{Y}_i$ is simply the complex number $V_i = V_{ix} + \iota V_{iy}$. Moreover, the rotation of a vector V by an angle θ is simply the multiplication by a complex exponential:

$$R(\theta)V = e^{\iota\theta}V = (\cos\theta V_x - sin\theta V_y) + \iota(\sin\theta V_x + \cos\theta V_y).$$

Before starting with the derivation of the laplacian, we need to define the *PL (piecewise linear) basis section*: this is done by extending the basis $(\mathbf{X}_i, \mathbf{Y}_i)$ from each vertex into the incident triangles through parallel transport along radii. For simplicity we take into consideration only the $\mathbf{X}_i$ vector for each vertex i, being $\mathbf{Y}_i$ univocally determined once a unit normal vector to $T_i\mathcal{M}$ is given. This gives a unit basis section Φ_i supported on the incident triangles, which coincides with the local basis on vertex i: $\Phi_i(i) = \mathbf{X}_i$. Φ_i is then attenuated with the barycentric coordinates on the triangles, so that the PL basis section on a point p in triangle

$T(i,j,k)$ can be expressed as

$$\Psi_i(p) = B_i(p)\Phi_i(p)$$

This basis can be used to represent a vector field $\mathbf{V}$ as the sum $\sum_i^N V_i\Psi_i$, with V_i being complex coefficients, so that the computation of the action a differential operator on field reduces to finding its action on the PL basis section and multiplying the resulting $N \times N$ matrix by the vector $\mathbf{V} = (V_1, \ldots, V_N)$.

Furthermore, we need to know the value of the scalar products of the elements of the basis section, which are needed to construct the matrix elements of the differential operator. Considering that Φ_j does not vary its direction along the edge $\mathbf{e}_{jk}$, we can state that

$$\Phi_j(k) = r_{jk}\Phi_k(k).$$

Moreover, Φ_k does not vary its direction along a ray from k to any point p within the triangle $T(i,j,k)$, and the same holds for Φ_j while moving from j to p. Since parallel transport along the subtriangle $T(k,p,j)$ gives the holonomy Ω_{kpj}, and since the holonomy is constant over all the points of a triangle, the holonomy of the subtriangle is simply given by the one of $T(i,j,k)$ times the area of the subtriangle as a fraction of the area $A_{T(i,j,k)}$. This allows to write the expression

$$\langle \Phi_j(p), \Phi_k(p) \rangle \, r_{jk} = e^{\iota\Omega_{kpj}} = e^{\iota\Omega_{ijk}B_i(p)}.$$

Considering that $\Psi_j = B_j\Phi_j$, and integrating symbolically in B_j, B_k over the triangle area, we come to the conclusion that

$$\langle\langle \Psi_j, \Psi_k \rangle\rangle_{ijk} = r_{kj}A_T\frac{6e^{\iota\Omega_{ijk}} - 6 - 6\iota\Omega_{ijk} + 3\Omega_{ijk}^2 + \iota\Omega_{ijk}^3}{3\Omega_{ijk}^4}.$$

We now have the elements we need for computing the laplacian, i.e. the values of the integrals $\langle \nabla\Phi_j, \nabla\Phi_k \rangle_{T(i,j,k)}$ for $j,k \in \{1,\ldots,N\}$. This requires the covariant derivatives of Φ_i and Φ_k. In order to find them, we use a linear parametrisation $f(x,y)$ of triangle $T(i,j,k)$,

with $f(0,0) = i$, $f(1,0) = j$ and $f(0,1) = k$, and denote by ∂_x and ∂_y the basis vectors of the embedded triangle. In order to compute $\nabla_{\partial_y}\Phi_j$ at a point p in $T(i,j,k)$, let ξ be a vector field on triangle $T(i,j,k)$ that coincides with Φ_j for $y = 0$ and does not vary while moving along the y axis of the parametrisation: hence we get $\nabla_{\partial_y}\xi = 0$. If we use the parametrisation $p = f(x,y)$ and define $q = f(x,0)$, then the holonomy around triangle T_{pqj} is given by $\Omega_{pqj} = (1-x)y\Omega ijk$. From parallel transport of field ξ one can easily obtain

$$e^{\iota\Omega_{pqj}}\xi(p) = e^{\iota(1-x)y\Omega_{ijk}}\xi(p) = \Phi_j(p).$$

This allows to compute the directional derivative of the basis as

$$\nabla_{\partial_y}\Phi_j = \left(\partial_y e^{\iota(1-x)y\Omega_{ijk}}\right)\xi = \iota(1-x)\Omega_{ijk}\Phi_j$$

.

By construction, Φ_j does not vary its direction while moving on straight lines departing from j and likewise Φ_k along segments from k, the covariant derivatives along ∂_x and ∂_y are related by linear equations:

$$(1-x)\nabla\partial_x\Phi_j - y\nabla_{\partial_y}\Phi_j = 0, \qquad x\nabla_{\partial_x}\Phi_k + (y-1)\nabla_{\partial_y}\Phi_k,$$

which specifies both components of the covariant derivatives of the basis section. In this parametrisation, $\Psi_j = x\Phi_j$ and $\Psi_k = y\Phi_k$, so that

$$\begin{aligned}
\nabla_{\partial_x}\Psi_j &= (1+\iota\Omega_{ijk}xy)\Phi_j, & \nabla_{\partial_y}\Psi_j &= \iota\Omega_{ijk}x(1-x)\Phi_j \\
\nabla_{\partial_x}\Psi_k &= -\iota\Omega_{ijk}y(1-y)\Phi_k, & \nabla_{\partial_y}\Psi_k &= (1-\iota\Omega_{ijk}xy)\Phi_k.
\end{aligned}$$

Let us switch to an orthogonal basis $\mathbf{u}_1, \mathbf{u}$ on $T(i,j,k)$: to compute the coefficient of the

coordinate transformation we use the metric tensor of components

$$g_{11} = |\mathbf{e}_{ij}|^2, \qquad g_{12} = g_{21} = \mathbf{e}_{ij} \cdot \mathbf{e}_{ik}, \qquad g_{22} = |\mathbf{e}_{ik}|^2,$$

so that the orthogonal basis can be written as

$$\mathbf{u}_1 = \frac{1}{\sqrt{g_{11}}}\partial_x, \qquad \mathbf{u}_2 = \frac{1}{2A_T\sqrt{g_{11}}}(g_{11}\partial_y - g_{12}\partial_x).$$

The expressions of the covariant derivatives of the basis section in this basis is then

$$\begin{aligned}
\nabla_{\mathbf{u}_1}\Psi_j &= \tfrac{1}{\sqrt{g_{11}}}(1 + \iota\Omega_{ijk}xy)\Phi_j, \quad \nabla_{\mathbf{u}_2}\Psi_j = \tfrac{1}{2A_T\sqrt{g_{11}}}(-g_{12} + \iota\Omega_{ijk}(g_{11}x(1-x) - g_{12}xy)\Phi_j \\
\nabla_{\mathbf{u}_1}\Psi_k &= -\tfrac{1}{\sqrt{g_{11}}}\iota\Omega_{ijk}y(1-y)\Phi_k, \quad \nabla_{\mathbf{u}_2}\Psi_k = \tfrac{1}{2A_T\sqrt{g_{11}}}(g_{11} + \iota\Omega_{ijk}(g_{12}y(1-y) - g_{11}xy))\Phi_k.
\end{aligned}$$

By taking the scalar products and integrating over triangle $T(i,j,k)$ we then obtain the matrix elements

$$\begin{aligned}
\langle\langle\nabla\Psi_j, \nabla\Psi_j\rangle\rangle_{ijk} &= \frac{1}{4A_T}\left[g_{22} + \Omega_{ijk}^2\frac{3g_{11} - 3g_{12} + g_{22}}{90}\right], \\
\langle\langle\nabla\Psi_j, \nabla\Psi_k\rangle\rangle_{ijk} &= \frac{r_{kj}}{A_T\Omega_{ijk}^4}\Big[(3g_{11} + 4g_{12} + 3g_{22}) + \iota\Omega_{ijk}(g_{11} + g_{12} + g_{22}) - \iota\Omega_{ijk}^3\frac{g_{12}}{6} + \\
&\quad + \Omega_{ijk}^4\frac{g_{11} - 2g_{12} + g_{22}}{24} - \iota\Omega_{ijk}^5\frac{g_{11} - 2g_{12} + g_{22}}{60} - ((3g_{11} + 4g_{12} + 3g_{22}) + \\
&\quad - \iota\Omega_{ijk}(2g_{11} + 3g_{12} + 2g_{22}) - \Omega_{ijk}^2\ \frac{g_{11} + 2g_{12} + g_{22}}{2}\Big)\, e^{\iota\Omega_{ijk}}\Big].
\end{aligned}$$

Converting back from complex numbers to rotation matrices, we obtain the expressions (6.4).

Bibliography

[1] W. Helfrich, *Elastic Properties of Lipid Bilayers: Theory and Possible Experiments*, Z. Naturforsch., Vol. 28 (1973), pp. 693-703;

[2] S. J. Singer & G. L. Nicholson, *The Fluid Mosaic Model of the Structure of Cell Membranes*, Science, Vol. 175, No. 4023 (1972), pp. 720-731;

[3] D. Nelson, T. Piran & S. Weinberg, *Statistical Mechanics of Membranes and Surfaces, 2nd edition*, World Scientific, 1989;

[4] D. R. Nelson & L. Peliti, *Fluctuations in membranes with crystalline and hexatic order*, J. Phys. France, Vol. 48 (1987), pp. 1085-1092;

[5] M. J. Bowik & A. Travesset, *The statistical mechanics of membranes*, Physics Reports, Vol. 344, No. 4-6 (2001), pp. 255-308;

[6] L. Peliti & S. Leibler, *Effects of Thermal Fluctuations on Systems with Small Surface Tension*, Phys. Rev. Lett, Vol. 54 (1985), p. 1690;

[7] D. Andelman, T. Kawakatsu & K. Kawasaki, *Equilibrium Shape of Two-Component Unilamellar Membranes and Vesicles*, Europhys. Lett., Vol. 19, No. 1 (1992), pp. 57-62;

[8] F. Jülicher & R. Lipowsky, *Domain-induced budding of vesicles*, Phys. Rev. Lett, Vol. 70, No.1 19 (1993), p. 2964;

[9] T. Baumgart, S. Das, W. W. Webb & J. T. Jenkins, *Membrane Elasticity in Giant Vesicles with Fluid Phase Coexistence*, Bioph. J., Vol. 89, No. 2 (2005), pp. 1067-1080;

[10] U. Seifert, *Curvature-induced lateral phase segregation in two-component vesicles*, Phys. Rev. Lett., Vol. 70, No. 9 (1993), p. 1335;

[11] T. Taniguchi, *Shape Deformation and Phase Separation Dynamics of Two-Component Vesicles*, Phys. Rev. Lett., Vol. 76, No. 23 (1996), p. 4444;

[12] U. Seifert, *Configurations of fluid membranes and vesicles*, Adv. Phys., Vol. 46, No. 1 (1997), pp. 13-137;

[13] P. B. S. Kumar & M. Rao, *Shape Instabilities in the Dynamics of a Two-Component Fluid Membrane*, Phys. Rev. Lett., Vol. 80, No. 11 (1998), p. 2489;

[14] H. Diamant, T. A. Witten, A. Gopal & K. Y. C. Lee, *Topography and instability of monolayers near domain boundaries*, Phys. Rev. E, Vol. 63, No. 6 (2001), p. 061602;

[15] J. L. Harden, F. C. MacKintosh & P. D. Olmsted, *Budding and domain shape transformations in mixed lipid films and bilayer membranes*, Phys. Rev. E, Vol. 72, No. 1 (2005), p. 011903;

[16] A. Bonito, R. H. Nochetto & M. S. Pauletti, *Parametric FEM for geometric biomembranes*, J. Comp. Phys., Vol. 220, No. 9 (2010), pp. 3171-3188;

[17] P. Tang & al., *Phase Separation Patterns for Diblock Copolymers on Spherical Surfaces: a Finite Volume Method*, Phys. Rev. E, Vol. 72 (2005), p. 016710;

[18] F. C. MacKintosh & T. C. Lubensky, *Orientational order, topology, and vesicle shape*, Phys. Rev. Lett., Vol. 67, No. 9 (1991), p. 1169;

[19] J. B. Fournier & L. Peliti, *Paired Defects of Nematic Surfactant Bilayers*, Phys. Rev. E, Vol. 58 (1998), p. R6919;

[20] Y. Fukui & S Inoué, *Cell Division in Dictyostelium with Special Emphasis on Actomyosin Organization in Cytokinesis*, Cell Mot. Cytoskel., Vol. 18 (1991), pp. 41-54;

[21] F. J. Nédélec & al., *Self-Organization of Microtubules and Motors*, Nature, Vol 389 (1997), p. 41;

[22] X. Xing & al., *Morphology of Nematic and Smectic Vesicles*, PNAS, Vol. 109, No. 14 (2012), pp. 5202-5206;

[23] H. Shin & al., *Topological Defects in Spherical Nematics*, Phys. Rev. Lett., Vol. 101 (2008), p. 037802;

[24] D. Marenduzzo & E. Orlandini, *Phase separation dynamics on curved surfaces*, Soft Matter, Vol. 9, No. 4 (2013), pp. 1178-1187;

[25] J. R. Baumgardner & P. O. Frederickson, *Icosahedral Discretization of the Two-Sphere*, SIAM J. Numer. Anal., Vol. 22, No. 6 (1985), pp. 1107-1115;

[26] Anthony A. Hyman, Christoph A. Weber, & Frank Jülicher, *Liquid-Liquid Phase Separation in Biology*, Annu. Rev. Cell Dev. Biol., Vol. 30 (2014), pp. 39-58;

[27] Diana M. Mitrea & Richard W. Kriwacki, *Phase separation in biology; functional organization of a higher order*, Cell Comm. Sig., Vol. 14, No. 1 (2016)

[28] M. E. Cates, D. Marenduzzo, I. Pagonabarraga & J. Tailleur, *Arrested phase separation in reproducing bacteria creates a generic route to pattern formation*, PNAS, Vol. 107, No. 26 (2010), pp. 11715-11720;

[29] T. Baumgart, A. T. Hammond, P. Sengupta, S. T. Hess, D. A. Holowka, B. A. Baird, & W. W. Webb, *Large-scale fluid/fluid phase separation of proteins and lipids in giant plasma membrane vesicles*, PNAS, Vol. 104, No. 9 (2007), pp. 3165-3170;

[30] F. A. Heberle & G. W. Feigenson, *Phase Separation in Lipid Membranes*, Cold. Spring Harb. Perspec. Biol., Vol. 3 (2011). p. a004697;

[31] I. Levental, F. J. Byfield, P. Chowdhury, F. Gai, T. Baumgart, P. A. Janmey, *Cholesterol-dependent phase separation in cell-derived giant plasma-membrane vesicles*, Biochem. J., Vol. 424, No. 2, pp. 163-167;

[32] T. Baumgart, S. T. Hess & W. W. Webb, *Imaging coexisting fluid domains in biomembrane models coupling curvature and line tension*, Nature, Vol. 425 (2003), pp. 821-824;

[33] K. Bacia, P. Schwille & T. Kurzchalia, *Sterol structure determines the separation of phases and the curvature of the liquid-ordered phase in model membranes*, PNAS, Vol. 102, No. 9 (2005), pp. 3272-3277;

[34] , S. L. Veatch & S. L. Keller, *Organization in Lipid Membranes Containing Cholesterol*, Phys. Rev. Lett., Vol. 86, No. 26 (2002), p. 268101;

[35] R. Parthasarathy, C. Yu & J. Y. Groves, *Curvature-Modulated Phase Separation in Lipid Bilayer Membranes*, Langmuir, Vol. 22, No. 11 (2006), pp. 5095-5099;

[36] J. W. Cahn & J. E. Hilliard, *Free Energy of a Nonuniform System. I. Interfacial Free Energy*, J. Chem. Phys., Vol. 28 (1958), p. 258;

[37] P. C. Hohenberg, B. I. Halperin, *Theory of dynamic critical phenomena*, Rev. Mod. Phys, Vol. 49, No. 3 (1977), pp. 435-475;

[38] E. Hairer, S. P. Nørsett, G., *Solving ordinary differential equations I: Nonstiff problems (2nd ed.)*, Berlin, Springer Verlag, 1993;

[39] J. H. Yao, K. R. Elde, H. Gu & M. Grant, *Theory and simulation of Ostwald ripening*, Phys. Rev. B, Vol. 47, No. 21 (1993), pp.14110-14125;

[40] I. M. Lifshitz & V. V. Slyozov, *The kinetics of precipitation from supersaturated solid solutions*, J. Phys. Chem. Solids, Vol. 19, No. 1-2 (1961), pp. 35-50;

[41] H. Miura & Masahide Kimoto, *A Comparison of Grid Quality of Optimized spherical Hexagonal-Pentagonal Geodesic Grids*, Mon. Wea. Rev., Vol. 133 (2005), pp. 2817-2833;

[42] B. J. Peter, H. M. Kent, I. G. Mills, Y. Vallis, P. J. G. Butler, P. R. Evans & H. T. McMahon, *BAR Domains as Sensors of Membrane Curvature: The Amphiphysin BAR Structure*, Science, Vol. 303, No. 567 (2004), pp. 495-499;

[43] I. M. Pranke, V. Morello, J. Bigay, K. Gibson, J. Verbavatz, B. Antonny, & Ca. L. Jackson, *α-Synuclein and ALPS motifs are membrane curvature sensors whose contrasting chemistry mediates selective vesicle binding*, J. Cell Biol., Vol. 194, No. 1 (2011), pp. 89-103;

[44] S. L. Veatch, O. Soubias, K. Gawrisch, *Critical fluctuations in domain-forming lipid mixtures*, PNAS, Vol. 104, No. 45 (2007), pp. 17650–17655;

[45] S. D. Connell, G. Heath, A. Kisil, *Critical point fluctuations in supported lipid membranes*, Faraday Discuss, Vol. 161 (2013), pp. 91-150;

[46] S. L. Veatch, P. Cicuta, B. Baird, *Critical fluctuations in plasma membrane vesicles*, ACS Chem. Biol., Vol. 3, No. 5 (2008), p. 287, 293;

[47] , T. Fischer, R. L. Vink, *Domain formation in membranes with quenched protein obstacles: lateral heterogeneity and the connection to universality classes*, J. Chem. Phys, Vol. 134, No. 5 (2011), p. 055106;

[48] B. B. Machta, S. Papanikolau, J. P. Sethna, S. L. Veatch, *Minimal model of plasma membrane heterogeneity requires coupling cortical actin to criticality*, Biophys. J., Vol. 100, No. 7 (2011), pp. 1668-77;

[49] J. Ehrig, E. P. Petrov, P. Schwille, *Near-critical fluctuations and cytoskeleton-assisted phase separation lead to subdiffusion in cell membranes*, Biophys. J., Vol. 100, No. 1 (2011), pp. 80-9;

[50] A. Honigmann, S. Sadeghi, R. Vink, *A lipid bound actin meshwork organizes lipid phase separation in model membranes*, Elife, Vol. 3 (2014), p. e01671;

[51] , M. Schick, *Membrane heterogeneity: manifestation of a curvature-induced microemulsion*, Phys. Rev. E, Vol. 85, No. 3 (2012), p. 031902;

[52] S. Meinhardt, R. L. Vink, F. Schmid, *Monolayer curvature stabilizes nanoscale raft domains in mixed lipid bilayers*, PNAS, Vol. 110, No. 13 (2013), pp. 4476-81;

[53] R. Parthasarathy, C. H. Yu, J. T. Groves, *Curvature-modulated phase separation in lipid bilayer membranes*, Langmuir, Vol. 22, No. 11 (2006), pp. 5095-9;

[54] J. D. Murray, *Mathematical biology. II: Spatial models and biomedical applications*, Springer-Verlag Berlin Heidelberg, 3rd ed. (2003), p. 71;

[55] A. Gierer & H. Meinhardt, *A Theory of Biological Pattern Formation*, Kybernetik, Vol. 12 (1972), pp. 30-39;

[56] G. Gonnella, E. Orlandini & J. M. Yeomans, *Lattice Boltzmann simulations of lamellar and droplet phases*, Phys. Rev. E, Vol. 58, No. 1 (1998), pp. 480-485;

[57] T. Taniguchi, M. Yanagisawa & M. Imai, *Numerical investigations of the dynamics of two-component vesicles*, J. Phys.: Condens. Matter, Vol. 23, No. 28 (2011), p. 284103;

[58] P. B. S. Kumar, G. Gompper & R. Lipowsky, *Budding Dynamics of Multicomponent Membranes*, Phys. Rev. Lett., Vol. 86, No. 17 (2001), pp. 3911-3914;

[59] T. Kohyama, D. M. Kroll & G. Gompper, *Budding of crystalline domains in fluid membranes*, Phys. Rev. E, Vol. 68, No. 6 (2003), p. 061905;

[60] J. Li, H. Zhang & F. Qiu, *Budding behaviour of Multi-Component Vesicles*, J. Phys. Chem. B, Vol. 117, No. 3 (2013), pp. 843-849;

[61] F. Quemeneur, C. Quilliet, M. Faivre, A. Viallat & B. Pépin-Donat, *Gel Phase Vesicles Buckle into Specific Shapes*, Phys. Rev. Lett., Vol. 108, No. 10 (2012), p. 108303;

[62] M. Ashrafuzzaman and J. Tuszynski, *Membrane Biophysics*, Biological and Medical Physics, Biomedical Engineering, Springer-Verlag Berlin, Heidelberg, 2012;

[63] OpenStax College, the Cell Membrane, October 22, 2013;

[64] D. Chapman, *Phase transitions and fluidity characteristics of lipids and cell membranes*, Quarterly Reviews of Biophysics, Vol. 8, No. 2 (1975), pp. 185-235;

[65] E. J. Shimshick & H. M. McConnell, *Lateral phase separation in phospholipid membranes*, Biochemistry, Vol. 12, No. 12 (1973), pp 2351–2360;

[66] A. Alessandrini, H. M. Seeger, T. Caramaschi, & P. Facci, *Dynamic Force Spectroscopy on Supported Lipid Bilayers: Effect of Temperature and Sample Preparation*, Biophys J., Vol. 103, No. 1 (2012), pp 38–47;

[67] L. Picas, F. Rico & S. Scheuring, *Direct Measurement of the Mechanical Properties of Lipid Phases in Supported Bilayers*, Biophys J., Vol. 102, No. 1 (2012), pp. L01-L03;

[68] P.B. Canham, *The minimum energy of bending as a possible explanation of the biconcave shape of the human red blood cell*, J. Theor. Biol., Vol. 26, No. 1 (1970), p. 61;

[69] E.A. Evans, *A new material concept for the red cell membrane*, Biophys J, Vol. 13 (1973), pp. 926–940;

[70] P. Bassereau, B. Sorree, & A. Lévy, *Bending lipid membranes: Experiments after W. Helfrich's model*, Adv. Colloid Interface Sci., Vol. 208 (2014), pp. 47–57;

[71] O. Azencot, M. O. Lix, F. Chazal & M. Ben-Chen, *Discrete Derivatives of Vector Fields on Surfaces - An Operator Approach*, ACM Trans. Graph., Vol. 34, No. 3 (2015), Article 29;

[72] F. Knöppel, K. Crane, U. Pinkall & P. Schröder, *Globally Optimal Direction Fields*, ACM Trans. Graph., Vol. 32, No. 4 (2013), Article 59;

[73] F. de Goes, B. Liu, M. Budninskiy, Y. Tong & M. Desbrun, *Discrete 2-Tensor Fields on Triangulations*, Computer Graphics Forum, Vol. 33, No. 5 (2014), pp. 13-24;

[74] B. Liu, Y. Tong & F. de Goes, *Discrete Connection and Covariant Derivative for Vector Field Analysis and Design*, ACM Trans. Graph., Vol. 35, No. 3 (2016), Article 23;

[75] M. Botsch, L. Kobbelt, M. Pauly, P. Alliez & B. Levy, *Polygon Mesh Processing*, A K Peters, Ltd., 2010;

[76] M. Meyer, M. Desbrun, P. Schröder & A. H. Barr, *Discrete Differential-Geometry Operators for Triangulated 2-Manifolds*, from H.-C. Hege & al. (eds.), *Visualization and Mathematics III*, Springer-Verlag Berlin Heidelberg (2003), pp. 35-57;

[77] H. T. McMahon & J. L. Gallop, *Membrane curvature and mechanisms of dynamic cell membrane remodelling*, Nature, Vol. 438, No. 7068 (2005), pp. 590-596;

[78] M. Ø. Jensen & O. G. Mouritsen, *Lipids do influence protein function — the hydrophobic matching hypothesis revisited*, BBA - Biomembranes, Vol. 1666, No. 1-2 (2004), pp. 205-226;

[79] W. B. Huttner & Joshua Zimmerberg, *Implications of lipid microdomains for membrane curvature, budding and fission: Commentary*, Curr. Opin. Cell Biol., Vol. 13, No. 4 (2001), pp. 478-484;

[80] T. R. Graham & M. M. Kozlov, *Interplay of proteins and lipids in generating membrane curvature*, Curr. Opin. Cell Biol., Vol. 22, No. 4 (2010), pp. 430-436;

[81] I. R. Cooke, *Coupling between Lipid Shape and Membrane Curvature*, Biophys. J., Vol. 91, No. 2 (2006), pp. 487-495;

[82] S. Sadeghi, M. Müller & R. L. C. Vink, *Raft Formation in Lipid Bilayers Coupled to Curvature*, Biophys. J., Vol. 107, No. 7 (2014), pp. 1591-1600;

[83] B. Sorre, A. Callan-Jones, J.-B. Manneville, P. Nassoy, J.-F. Joanny, J. Prost, B. Goud & P. Bassereau, *Curvature-driven lipid sorting needs proximity to a demixing point and is aided by proteins*, PNAS, Vol. 106, No. 14 (2009), pp. 5622-5626;

[84] P. Rangamani, K. K. Mandadap & G. Oster, *Protein-Induced Membrane Curvature Alters Local Membrane Tension*, Biophys. J., Vol. 107, No. 3 (2014), pp. 751-762;

[85] G. Garg, Shailendra Saraf & Swarniata Saraf, *Cubosomes: An Overview*, Biol. Pharm. Bull., Vol. 30, No. 2 (2007), p. 350-353;

[86] S. K. Vogel, F. Heinemann, G. Chwastek & Petra Schwille, *The Design of MACs (Minimal Actin Cortices*, Cytoskeleton (Hoboken), Vol. 70, No. 11 (2013), pp. 706-717;

[87] C. Campillo, P. Sens, D. Köster, L. Pontani, D. Lévy, P. Bassereau, P. Nassoy & C. Sykes, *Unexpected Membrane Dynamics Unveiled by Membrane Nanotube Extrusion*, Biophys. J., Vol. 104, No. 6 (2013), pp. 1248-1256;

[88] F. Heinemannm, S. K. Vogel & P. Schwille, *Lateral Membrane Diffusion Modulated by a Minimal Actin Cortex*, Biophys. J., Vol. 104, No. 7 (2013), pp. 1465-1475;

[89] S. K. Vogel & P. Schwille, *Minimal systems to study membrane-cytoskeleton interactions*, Curr. Opin. Biotech., Vol. 23, No. 5 (2012), pp.758-765;

[90] B. Jerome, *Surface Effects and Anchoring in Liquid Crystals*, Rep. Prog. Phys., Vol. 54 (1991), p. 341;

[91] M. S. Spector, S. Sprunt & J. D. Litster, *Novel Dynamical Mode in a Tilted Smectic Liquid-Crystal Film*, Phys. Rev. E, Vol. 47, No. 2 (1993), p. 1101;

[92] C. Y. Young & al., *Light-Scattering Study of Two-Dimensional Molecular-Orientation Fluctuations in a Freely Suspended Ferroelectric Liquid-Crystal Film*, Phys. Rev. Lett., Vol. 40 (1978), p. 773;

[93] P. Dalhaimer, D. E. Discher & T. C. Lubensky, *Crosslinked Actin Networks Show Liquid Crystal Elastomer Behaviour, Including Soft-Mode Elasticity*, Nature Physics, Vol. 3 (2007), p. 354;

[94] J.-B. Fournier & P. Galatola, *Modeling planar degenerate wetting and anchoring in nematic liquid crystals*, Europhys. Lett., Vol. 72, No. 3 (2005), pp. 403-409;

[95] D. R. Nelson & J. M. Kosterlitz, *Universal Jump in the Superfluid Density of Two-Dimensional Superfluids*, Phys. Rev. Lett., Vol. 39, No. 19 (1977), pp. 1201-1205;

[96] R. L. Blumberg Selinger, A. Konya, A. Travesset & J. V. Selinger, *Monte Carlo Studies of the XY Model on Two-Dimensional Curved Surfaces*, J. Phys. Chem. B, Vol. 115., No. 48 (2011), pp. 13989-93;

[97] T. Lopez-Leon, V. Konig, K. B. S. Devaiah, V. Vitelli & A. Fernandez-Nieves, *Frustrated nematic order in spherical geometries*, Nat. Phys., Vol. 7, No. 5 (2011) pp. 391-394;

[98] V. Vitelli & D. R. Nelson, *Nematic textures in spherical shells*, Phys. Rev. E, Vol. 74, No. 2 (2006), p. 021711;

[99] G. Napoli & L. Vergori, *Extrinsic Curvature Effects on Nematic Shells*, Phys. Rev. Lett., Vol. 108, No. 20 (2012);

[100] S. Sachdev & D. R. Nelson, *Crystalline and fluid order on a random topography*, J. Phys. C: Solid State Phys., Vol. 17 (1984) pp. 5473-89;

[101] V. Vitelli & D. R. Nelson, *Defect generation and deconfinement on corrugated topographies*, Phys. Rev. E, Vol. 70, No. 5 (2004) p. 051105;

[102] M. J. Bowick, D. R. Nelson & A. Travesset, *Interacting topological defects on frozen topographies*, Phys. Rev. B, Vol. 62, No. 13 (2000), pp. 8738-51;

[103] A. A. Bridges & A. S. Gladfelter, *Septin Form and Function at the Cell Cortex*, J. Biol. Chem., Vol. 290, No. 28 (2015), pp. 17173-17180;

[104] A. S. Gladfelter, J. R. Pringle & D. J. Lew, *The septin cortex at the yest mother-bud neck*, Curr. Opin. Microbiol., Vol. 4, No. 6 (2001), pp. 681-9;

[105] M. P. Sheetz, J. E. Sable & H. G. Döbereiner, *Continuous membrane-cytoskeleton adhesion requires continuous accomodation to lipid and cytoskeleton dynamics*, Annu. Rev. Biophys. Biomol. Struct., Vol. 35 (2006), pp. 417-434;

[106] N. Morone, T. Fujiwara, K. Murase, R. S. Kasai, H. Ike, J. Usukura & A. Kusumi, *Three-dimensional reconstruction of the membrane skeleton at the plasma membrane interface by electron tomography*, J. Cell. Biol., Vol. 174, No. 6 (2006), pp. 851-862;

[107] T. M. Svitkina & G. G. Borisy, *Arp2/3 complex and actin depolymerizing factor/cofilin in dendritic organization and treadmilling of actin filament array in lamellipodia*, J. Cell. Biol., Vol. 145, No. 5 (1999), pp. 1009-26;

[108] T. Fujiwara, K. Ritchie, H. Murakoshi, K. Jacobson & A. Kusumi, *Phospholipids undergo hop diffusion in compartmentalized cell membrane*, J. Cell. Biol., Vol. 157, No. 6 (2002), pp. 1071-1081;

[109] M. J. Stephen & J. P. Straley, *Physics of Liquid Crystals*, Rev. Mod. Phys., Vol. 46, No. 4 (1974), pp. 617-704;

[110] S. Chandrasekhar, *Liquid Crystals*, Cambridge University Press (1993), p. 118;

[111] P. G. de Gennes, *The Physics of Liquid Crystals*, Clarendon Press, 1979;

[112] P. M. Chaikin, T. C. Lubensky, *Principles of condensed matter physics*, 2007, Cambridge University Press;

[113] M. Spivak, *A comprehensive introduction to differential geometry*, Publish or Perish, 1970

[114] M. Masuda, S. Takeda, M. Sone, T. Ohku, H. Mori, Y. Kamioka & N. Mochizuki, *Endophilin BAR domain drives membrane curvature by two newly identified structure-based mechanisms*, EMBO J., Vol. 25, No. 12 (2006), pp. 2889-2897;

[115] F. de Goes, M. Desbrun, Y. Tong, *Vector Field Processing on Triangle Meshes*, Proceeding of SA '15 SIGGRAPH Asia 2015 Courses, Article No. 17, ACM, New York;

[116] K. Polthier & E. Preuss, *Identifying vector field singularities using a discrete Hodge decomposition*, Vis. and Math. III (2003), pp. 113-134;

[117] Y. Tong, S. Lombeyda, A. N. Hirani & M. Desbrun, *Discrete multiscale vector field decomposition*, ACM Trans. Graph., Vol. 22, No. 3, pp. 445-452;

[118] A. N. Hirani, *Discrete Exterior Calculus*, PhD Thesis, Caltech (2003);

[119] M. Desbrun, E. Kanso & Y. Tong, *Discrete differential forms for computational modeling*, in E. Grinspun, P. Schröder & M. Desbrun, *Discrete Differential Geometry*, Course Notes, ACM SIGGRAPH (2006);

[120] K. Crane, F. DeGoes, M. Desbrun & P. Schröder, *Digital geometry processing with discrete exterior calculus*, Course Notes, ACM SIGGRAPH (2013);

[121] E. Zhang, K. Mischaikow & G. Turk, *Vector Field Design on Surfaces*, ACM Trans. Graph., Vol. 25, No. 4 (2006), pp. 1294-1326;

[122] S. Alonso, Y. Dietrich, C. Händel, J. A. Käs & M. Bär, *Oscillations in the Lateral Pressure of Lipid Monolayers Induced by Nonlinear Chemical Dynamics of the Second Messengers MARCKS and Protein Kinase C*, Biophys. J., Vol. 100, No. 4 (2011), pp. 939, 947;

[123] V. Y. Kiselev, D. Marenduzzo & A. B. Goryachev, *Lateral Dynamics of Proteins with Polybasic Domain on Anionic Membranes: A Dynamic Monte-Carlo study*, Biophys. J., Vol. 100, No. 5 (2011), pp. 1261-1270;

[124] H. Strahl, F, Bürmann & L. W. Hamoen, *The actin homologue MreB organizes the bacterial cell membrane*, Nat. Comm., Vol. 5, Article No. 3442 (2014).

Note: all figures were produced by the candidate unless otherwise specified.